UNIVERSITY OF SOUTHAMPTON

FACULTY OF ENGINEERING AND PHYSICAL SCIENCES

School of Electronics and Computer Science

An investigation into the use of Zinc Oxide Nanowire Sensors in the detection of Micro-RNA Cancer Biomarkers

by

Joshua D. Akrofi

Thesis for the degree of Doctor of Philosophy

July 2022

UNIVERSITY OF SOUTHAMPTON

ABSTRACT

FACULTY OF ENGINEERING AND PHYSICAL SCIENCES
School of Electronics and Computer Science

Doctor of Philosophy

AN INVESTIGATION INTO THE USE OF ZINC OXIDE NANOWIRE SENSORS IN THE DETECTION OF MICRO-RNA CANCER BIOMARKERS

by Joshua D. Akrofi

Cancer is a complex disease characterised by genes which encode oncogenic and tumour-suppressor proteins. microRNAs (miRNA), a group of small noncoding RNAs that regulate gene expression, have been shown to participate in a number of essential biological process including cell proliferation control, hematopoietic B-cell lineage fate, B-cell survival, brain patterning, pancreatic cell insulin secretion and adipocyte development [1]. Abnormal expression, that is, the loss, amplification and mutations of miRNA genes has been identified in a wide variety of cancers including B-Cell Chronic Lymphocytic Leukemia (B-CLL) [2], breast carcinoma [3], primary glioblastoma [4], hepatocellular carcinoma [5], papillary thyroid carcinoma [6], lung cancer [7], colon carcinoma [8], and pancreatic tumours [9].

Presently, medical diagnostic tests, by and large, are performed in laboratories equipped with bench-top analyzers and operated by trained lab technicians. Although these systems have a high throughput, in most cases patients wait a number of days to receive their test results [10]. Being able to perform diagnostic tests at or near the site where patients encounter the health care system; and receiving the results within the time frame of a consultation with a healthcare professional (approximately 15 minutes [11]), would be extremely beneficial. It would provide actionable information that can lead to several changes in patient management. With respect to cancer diagnostics and treatment, this would reduce the need for multiple patient visits; enabling the prompt treatment of the illness in a more targeted fashion.

Point of Care (PoC) devices are diagnostic devices which rapidly provide actionable information for patient care at the time and location of an encounter with the health care system. They are becoming more prevalent. The most commonly found type of PoC device is the Lateral Flow Immunoassays (LFIA) [12] [13]. However, LFIA conventionally provide qualitative results (i.e., yes or no) which are of little use when trying to gauge changes in concentration as would be needed in detecting the loss or amplification miRNA strands. Furthermore, LFIA suffers from difficulties due to varying consistency of the flow rate and from non-uniform dispersion of the sample to label [10]. Field Effect Transistor (FET) biosensors, a promising class of PoC devices, have been shown to able to distinguish between

different concentrations of molecular analyte [14]. This function would be vital in cancer diagnosis revolving around detection of the abnormal expression of miRNA. This is because cancerous cells typically manifest a deviation in miRNA concentration from the normal range.

These FETs are made with established semiconductor techniques and technologies meaning that, they can be readily integrated with other electronic systems. This would enable on chip signal processing and the instantaneous electronic transmission of results from remote areas to a centralised hub. The goal is to leverage the advantages in semiconductor technologies to develop a PoC device for cancer diagnostics. This is to enable cancers to be caught and treated earlier thus reducing the need for invasive or debilitating treatments like surgery or chemotherapy.

In pursuit of this goal, the preliminary step was to fabricate FETs capable of detecting changes in miRNA concentration. The FETs fabricated for this purpose were Zinc Oxide Nanowire Field Effect Transistors (NWFETs) arrays. ZnO is an ideal material with which to fabricate these NWFETs because it is naturally a n-type semiconductor [15], thus eliminating the need for a high temperature doping process steps. ZnO has a large and direct band-gap (3.37 eV [16]) which enables it to sustain large electric fields; withstand higher breakdown voltages; generate lower levels of noise; and operate at high temperatures and levels of power [17]. The ZnO NWFETs were passivated with stack high-κ dielectrics. The stack layer consists of a layer of Hafnium dioxide sandwiched between two Aluminium oxide layers which has been shown to diminish threshold voltage drift effectively [18]. Once fabricated, the ZnO NWFETs were first tested to observe how well they functioned as transducers of ionic charge. The ZnO NWFETs were seen to be excellent transducers of ionic charge with a shift in gate voltage per pH of 117 mV/pH. This shift in gate voltage per pH is comparable to largest known value of 220 mV/pH recorded by Knopfmacher's single Silicon NWFET with a Dual Gate [19]. It is also twice as large as the Nernst limit (59 mV/pH).

Following the pH-sensing experiment, a microDNA(miDNA) detection investigation was conducted. miDNA are the stable biological equivalent of miRNA and thus can serve as proxy of miRNA detection. The result of the investigation was compelling. The ZnO NWFETs were found to have a 43.88% Sensitivity to one order of magnitude changes in miDNA concentration (10 nM, 100 nM and 1 μM). Subsequently, the same investigation was carried out with miRNA as the analyte. In this instance the ZnO NWFETs were found to have a 5.07% Sensitivity to one order of magnitude changes in miRNA concentration of (10 nM, 100 nM and 1 μM). These results irrevocably demonstrate that ZnO NWFETs are capable of detecting changes in miRNA concentration. Thus, making ZnO NWFETs a suitable candidate for the development of a PoC device with which to conduct cancer diagnostics.

Contents

List of Figures

List of Tables

Declaration of Authorship

I, Joshua D. Akrofi , declare that the thesis entitled *An investigation into the use of Zinc Oxide Nanowire Sensors in the detection of Micro-RNA Cancer Biomarkers* and the work presented in the thesis are both my own, and have been generated by me as the result of my own original research. I confirm that:

- this work was done wholly or mainly while in candidature for a research degree at this University;
- where any part of this thesis has previously been submitted for a degree or any other qualification at this University or any other institution, this has been clearly stated;
- where I have consulted the published work of others, this is always clearly attributed;
- where I have quoted from the work of others, the source is always given. With the exception of such quotations, this thesis is entirely my own work;
- I have acknowledged all main sources of help;
- where the thesis is based on work done by myself jointly with others, I have made clear exactly what was done by others and what I have contributed myself;
- none of this work has been published before submission

Signed:

Date: July 2022

Acknowledgements

Thank you God. Who would have thought 3 months into a MSc programme, I would be able to switch onto a PhD programme. To Prof. Harold Chong and Dr. Maurits de Planque, thank for giving me opportunity to take on this PhD. I will be eternally grateful for you tireless support, encouragement, guidance, and unfailing patience throughout my time in Southampton.

Special thanks to Martin Ebert for teaching me how to fabricate ZnO NWFETs. I don't think I'm exaggerating when I say you saved me from rummaging in the dark for 2+ years trying to figure out how to make these devices. No devices, no results! Thus, any success I have experienced over the course of this project must be attributed to your massive contribution. Thank you.

I would like to thank Dr. Norman Godinho for funding this project. To Don Rolt and Prof. Arthur Brunnschweiler thank you for dropping by every so often to check up on the progress of the project.

Dad, Mum, John and Angela you guys are the best. From Merton to GIS, King David to Uni of Liverpool, you've been there every step of the way praying for me and cheering me on. As cliche as it sounds, I literally could not have made it this far without you. This Doctorate is ours to share. Love you loads.

Now because I am lazy and want to be done with this thesis, I am going to list all the people, I can remember, who've made living and work in Southampton such joy and privilege. There's the university massive; my church family (Ascension Bitterne); Sinking Brass Band; Brasoc Samba Batucada; and Capoeira Mar Azul.

Jamie, Anushka, Ben, Omesh, Libe, Mike Perry, Owain, Lukas, Liam, Ali K, Ali, Ying, SweZin, James Frame, Milan, Thomas M, Quite Dan, Loud Dan, Kouta, Thomas, Moise and Yue Fan; Andy and Nicky, Lorna and Mac, Nathan, Luke, Esme, Anne, Ben O, Rachel, Andrew, Ruth, Byron, Jake and David; Rich, Matthew, Mark, Dan, Elena; Dave, Roland, Mikee, Vaguinho and Eliene, Amelia and Tuto, Fernanda, Gabrielle, Gabi, Opkar, Alex, Mikahil, Rafa, Stephen, Hug Ben; Nefeli, Mestre, Suzannah, Sebastian and Lorenzo, Hakan, Sofia, Matthew, Danada and Miguel.

Liam Trace-Kleeberg, I saved a paragraph just for you mate. Loved living with you. So much laughter and joy in everything from KFC Fridays to knock abouts. You made the first lockdown that much more bearable. Thanks for everything, even the floaties.

Florentin and Salma. I has been such a blessing getting to know both of you over the course of our PhDs. I can't express how much I appreciate all that you did for me. For taking care of me after my surgery, to encouraging me to join the Sinking Brass Band. Life in Southampton would have been as awesome without both of you.

To Charlie my teacher and my friend, thank you for taking me under your wing and broadening my horizons. Grande Abraços.

To Prissy and the Leigh family, the story of my PhD isn't complete without you. Bisous.

To Jude and Elsie Hayford, the oasis in my desert. How you manage to find humour in every situation never ceases to amaze me. You never made it to Southampton but you were always there when I needed you. Can't thank you guys enough.

To George Neequaye. Chief Hype Man! Groom to my best man. Bro we made it!!

Ellie Morgan you are a LEG END. WHEN WILL IT END?!!!

And Finally, to Ben & Jerry's and Plantain chips, rays of sunshine on many a bleak and miserable day, the sustenance you provided was second to none. From the bottom of my gut I thank you.

Publications

Journal paper

J.D. Akrofi, M. Ebert, J.D. Reynolds, K. Sun, R. Hu and M.R.R. de Planque and H.M.H. Chong. Multi-stack insulator to minimise threshold voltage drift in ZnO FET sensors operating in ionic solutions. Micro and Nano Engineering(2020). 100066. 2590-0072.https://doi.org/10.1016/j.mne.2020.100072

Conferences

J.D. Akrofi, M. Ebert, J.D. Reynolds, K. Sun, R. Hu, M.R.R. de Planque, H.M.H. Chong. Improving the stablility of ZnO NWFETs operating in 150 mM Phosphate Buffered Solution. In *45th International Conference on Micro & Nano Engineering*, 2019.

B.D. Rowlinson, J. Akrofi, M. Ebert, H.M.H. Chong. Improving electrical performance of PEALD ZnO TFTs for Heterogeneous Integration, using highly-selective TMAH wet-etching of Al2O3 for contact vias.In *45th International Conference on Micro & Nano Engineering*, 2019.

Nomenclature

ABL	Tyrosine-protein kinase ABL
Al	Aluminium
Al_2O_3	Aluminium dioxide
APTES	3-aminopropyltriethoxysilane
ATP	Adenosine Tri-Phosphate
AZO	Aluminium Zinc Oxide
bio-FET	bio-molecule sensing FET
CMOS	Complementary Metal Oxide
DEZ	Diethylzinc
DNA	Aeoxyribonucleic acid
FET	Field Effect Transistor
HCl	Hydrochloric acid
HfO_2	Hafnium dioxide
IBE	Ion Beam Etch
KCl	Potassium Chloride
LOR	Lift off resist
miDNA	Micro Deoxyribonucleic acid
miRNA	Micro Ribonucleic acid
MOSFET	Metal Oxide Semiconductor Field Effect Transistor
NaCl	Sodium Chloride
NaH_2PO_4	monobasic Sodium Phosphate
Na_2HPO_4	dibasic Sodium Phosphate
NaPi	Sodium Phosphate Buffer
NMP	1-Methyl-2-pyrrolidinone
NWFET	Nanowire Field Effect Transistor
PBS	Phosphate Buffered Saline
PEALD	Plasma Enhanced Atomic Layer Deposition
pH-FET	pH sensing FET
PMGI	polymethylglutarimide
PMMA	polymethyl methacrylate
SEM	Scanning Electron Microscope
SERS	Surface-enhanced Raman spectroscopy

Si	Silicon
SiO_2	Silicon dioxide
TE buffer	Trizma-Ethylenediaminetetraacetic (EDTA) buffer
TEMAH	Tetrakis(ethylmethylamino)hafnium(IV)
TFT	Thin Film Transistor
TMA	Trimethylaluminum
TMAH	tetramethylammoniumhydroxid
ZnO	Zinc Oxide

List of Symbols

β	Buffering capacity	mol
C_{ox}	Capacitance of the gate oxide per unit area	F
ϵ_S	dielectric constant of the semiconductor	
g_m	Transconductance	S
I_0	current response to the lowest analyte concentration	A
I_D	drain current	A
I_{norm}	normalised change in drain current	A
I_n	current response to the highest analyte concentration	A
k	Boltzmann constant	$1.38066 \times 10^{-23} J/K$
L	gate lengths	m
l_B	Bjerrum length	$0.7nm$
λ_D	debye length	m
μ_n	mobility of the minority carriers	$cm^2/V.s$
N_A	the acceptor concentration	cm^{-3}
N_D	electron donor concentration	cm^{-3}
pH_{pzc}	pH point of zero charge	
Ψ_B	bulk potential	V
q	the elementary charge	$1.60218 \times 10^{-19} C$
$q\phi_m$	work function of the gate metal	eV
$q\phi_s$	the work function of the semiconductor material	eV
ρ_i	density of the ions in a solution	cm^{-3}
$\sum_i$	sum over all ions in a solution	
SS	subthreshold slope	$Vdec^{-1}$
T	absolute temperature	K
φ	surface potential	V
V_D	drain voltage	V
V_{FB}	flat band voltage	V
V_G	gate voltage	V
V_T	threshold voltage	V
V_{Dep}	depletion voltage	V
W_1	depletion width	m

Z	gate width	m
z_i	the valence of ions in solution	

Disclaimer

It should be noted that all experimental results presented in this thesis were products of single measurement investigations unless stated otherwise. The reader should also be aware of the limitation that single datasets pose, since no statistical analysis based on repeatable experiments can be made. In a previous experiment [18] a Trizma based buffer was used because the analyte sample, 100 nM single strand miDNA-21 (ssDNA) in TE Buffer sample (10 μM Trizma, 50 μM KCl, 1 μM EDTA), was readily available in the lab storage. It was more convenient to use that analyte sample than prepare a PBS based analyte sample buffer. For consistency's sake it was decided that Trizma based buffer would be used in all subsequent miDNA-21 and miRNA-21 detection experiments. Changes in the concentration of the constituent parts of the Trizma based buffers used will be made explicit in the thesis. Finally, it should be noted that data on the response time (time constant) of the ZnO NWFETs has not been presented. This due to the manner in which the experiments presented in this thesis were conducted. This made it difficult to truly the time constant of the ZnO NWFETs.

Chapter 1

Preface

1.1 Introduction

For decades, scientist have sought to mimic the unparalleled efficiency of biological organisms in the recognition of foreign substances. Using recognition elements from biological organisms, referred to as bioreceptors or synthetic receptors, the selective sensing and chemical analysis of analyte can be performed in a variety of ways. The term biosensor generally describes devices that consist of bioreceptors and a transducer. Biosensors are designed to facilitate the interaction between the analyte and bioreceptors so as to produce a measurable chemophysical signal that is converted by the transducer into an electronic signal [20].

Biosensors are classified either by their bioreceptor or their transducer type. The main groups of bioreceptors are biological molecular species such as antibodies, enzymes, proteins, and nucleic acids; and living biological systems namely cells, tissue, or whole organisms. Biosensors can also be classified by the method the device transduces the chemophysical signal created during the interaction between analyte and bioreceptors. Transducers can be broadly grouped into 3 detection methods: optical, electrochemical and mass.

The optical methods of detection can be further subdivided based on the different types of spectroscopy. These include absorption, fluorescence, phosphorescence, Raman, SERS, refraction and dispersion spectrometry. These method are used to record the following spectrochemical properties: amplitude, polarization, energy, decay time and/or phase. Amplitude is the most commonly measured parameter of the electromagnetic spectrum, because it is generally correlated with the analyte concentration.

Mass-sensitive techniques such as surface acoustic wave and microbalance are another form of transduction that has been used for biosensors. This form transduction relies on the use of piezoelectric crystals which vibrate at a specific frequency. The oscillation frequency changes as mass increases when analyte binds with the bioreceptors. The change in frequency can be measured electrically and can be used to determine the additional mass.

Electrochemical detection is the third main method of transduction. Unlike with fluorescence, the most sensitive of the optical techniques, analyte molecules do not require the labor intensive step of tagging with a fluorescent label for electrochemical detection. Field Effect Transistors(FETs) are most common electrochemical transducers used in biochemical sensing applications. They garnered a lot of interest in the last few decades for a number of reasons including parallel sensing, fast response times and seamless integration with established technologies such as Complimentary Metal-Oxide Semiconductors (CMOS) [21]. As noted above, a variety of methods including Surface Plasmon Resonance [22], Enzyme Linked Immuosorbent Assay [23], Micro-cantilever beam arrays [24], Quartz crystal micro-balances and Optical micro-ring resonators [25] have been reported to demonstrate the detection of a number of bio-molecules. These detection techniques, their individual merits not withstanding, have not been able to demonstrate the rapid, highly sensitive, multiplexed detection of biomolecules [26] that Field effect transistors (FETs) have been shown to consistently produce. FETs are able to detect femtomolar concentrations of bio-molecules in solution without the need for labelling the bio-molecules or using large, expensive optical tools to perform their function [27]. Furthermore, they provide additional information such as conformational changes [28] and extracellular potentials [29] which other label-free biosensors currently do not provide.

FETs biosensors have been used in a variety of ways ranging from medical diagnostics [30] and environmental monitoring[31] through to use in the food[32] and pharmaceutical industries [33]. The following subsections highlight a few of the was FET biosensors have been used.

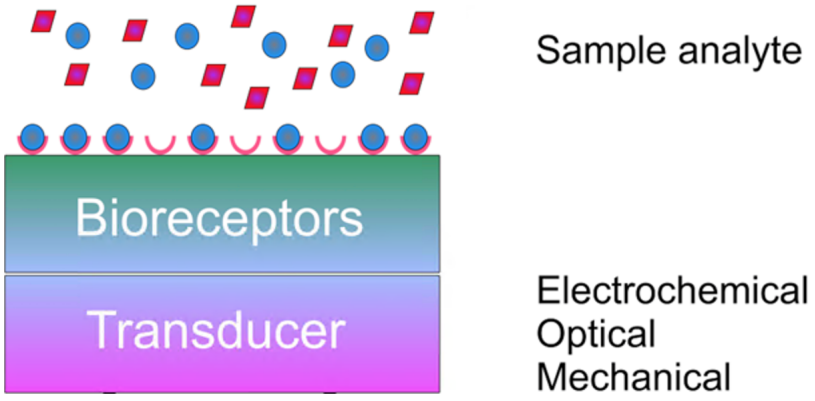

Figure 1.1: A schematic of the structure of a biosensor [34].

1.1.1 FETs in Action: Disease Diagnosis

FETs have been used detect bio-molecules such as DNA [35] [36] [37], proteins [38] [39] [40] and viruses [41] in a host of experiments. In detecting nucleic acids, it has been shown that appropriately surface modified FETs can be used to distinguish mutations in a sequence [42], thus paving for the way for FETs to be used in experiments to detect genetic modifications associated with disease.

To this end, nascent investigations by Zheng et al[43] and Patolsky et al [30] have demonstrated the potential of FETs as diagnostic tool. Patolsky in one experiment exhibited the direct, real-time

detection of influenza A virus cells and, in another, the detection of Influenza A or Adenovirus cells in tandem. Zheng, in focusing on cancer diagnosis using protein biomarkers, showed multiplexed detection of prostate specific antigen (PSA), PSA-α1-antichymotrypsin, carcinoembryonic antigen and mucin-1. In addition to that Zheng was able to distinguish, in real time, between the binding and activity of Telomerase (extracted from tumor cells) and the binding and inactivity of Telomerase (extracted from healthy somatic cells). The importance of such experiments can hardly be overstated as the enzyme Telomerase, in this instance, is inactive in most normal somatic cells but active in $\geq 80\%$ of known human cancers at the time [44].

1.1.2 FETs in Action: Drug Testing

Wang et al successfully used FETs sensors in a bio-pharmaceutical application. Wang monitored the binding activity of Adenosine Tri-Phosphate (ATP) to ABL, a protein tyrosine kinase immobilised on the surface of a FET, by controlling the addition of a drug candidate Gleevec [33]. Since the 1970s ABL role in the development in nearly all cases of chronic myelogenous leukemia has been established thus, Gleevec was developed to inhibit the function of ABL which includes binding to ATP [45].

In Wang's study, the conductance of the FET increased as ATP bound itself to ABL. However, this increase in the conductance of the FET was dampened when the competitive binding of uncharged Gleevec molecules to the ABL prevented the binding of ATP. This experiment, in exhibiting the ability of FETs to distinguish the activity of enzyme in the absence and presence of small-molecule inhibitor demonstrated the readiness of FETs to serve as a technology platform for drug discovery.

More recent applications of FETs being utilised in drug testing include a low-cost drug toxicity test platform that is sensitive enough to distinguish the cytotoxicity of different chemicals [46]; an investigation in the effects of a chemotherapeutic drug, topotecan hydrochloride, on tumor cells cultured on the FET devices [47]; and a demonstration of the ability FETs to perform the continuous monitoring of the extracellular effects of drugs on the transmembrane potentials of mammalian cardiomyocytes [48].

1.1.3 FETs in Action: PoC device development

Whether it is in doctor's office, in a patients home, at a patient's bedside or out in the field, clinicians and patients alike have had a long standing desire for miniaturised, portable devices that can rapidly deliver a prognosis at point at which care is being administered. Tran et al. described the development of a PoC device which is able to detect tumor cells extracted from circulating in the blood or lymph nodes of colorectal cancer patients [49].

FETs used in those experiments attained better results, in terms of sensitivity and speed of detection, than the current standard method based on pathological examination of tissue sections and the emerging clinical gold standard based on molecular assays. The growing possibility of achieving a highly accurate and sensitive analysis of of tumor cells within the surgery time frame has the potential to

negate the need for secondary surgery, consequently, decreasing patient morbidity and time spent in hospital [50].

1.2 Aims and Motivation

These studies listed above demonstrate the potential of a FET based biosensing platform as a tool for diagnosing diseases, testing the efficacy of drugs and developing PoC devices. Our aim is to leverage the excellent biosensing properties of FETs to develop a proof-of-concept PoC device for cancer diagnostics. In doing so we hope to enable cancers to be caught and treated earlier thus, reducing the need for invasive or debilitating treatments like surgery or chemotherapy.

To that end, the focus of this thesis is to document the progress made in developing a FET based biosensing platform than can detect microRNA (miRNA) and changes in its concentration. miRNA are an important group of non-protein coding RNA molecules which regulate gene expression at the transcriptional and post-transcriptional level in wide range of animals, plants, and viruses [51]. The downregulation of miRNA is observed in a wide variety of cancers. As such, miRNA profiles can be used to deduce the developmental lineage and differentiation states of tumours [52], making miRNA an important group of cancer diagnostic biomarkers. Hence, the motivation for wanting to develop a FET biosensing platform than can detect changes in miRNA concentration.

The excellent material properties of Zinc Oxide (ZnO) serve as the starting point for the development of such a device. ZnO is an ideal material with which to fabricate a FET biosensor because it is naturally a n-type semiconductor [15]. This eliminates the need for a high temperature doping process step. ZnO also has a large and direct band-gap (3.37 eV [16]) which enables it to sustain large electric fields; withstand higher breakdown voltages; generate lower levels of noise; and operate at high temperatures and levels of power [17]. The goal in leveraging these excellent material properties, is to develop a FET biosensor with outstanding transductive abilities. Such a device would be able to achieve a gate voltage shift greater than the Nernst Limit (59 mV/pH). In addition to this, it is important that the device being developed be able to withstand the monotonic, temporal and relatively slow change in threshold voltage caused by the hydration. This would aid in reducing the rate of decay of the output current. The section below highlights the process by which the aims set out above were tackled in this thesis.

1.3 Thesis Outline

This thesis begins in earnest by exploring the structure and function of the Metal Oxide Field Effect Transistor (MOSFET). This transducer forms the basis of the biosensor used in the experiments documented in this thesis. By and large FET biosensors are silicon based [53–59] however, other materials such as Molybdenum disulfide [60], Indium Tin Oxide [61], Indium Oxide [62], Graphene

[63] have been used to fabricate FET biosensors. Rarer still are Zinc Oxide (ZnO) FET biosensors [64]. The second chapter ends by exploring the material properties of ZnO.

The process for fabricating ZnO FET biosensor is described in the subsequent chapter. Chapter 4 charts the evolution of the MOSFET to FET pH-sensor, the precursor to the FET biosensor. Through a literature review it details how electrochemical transduction works and the lays out the transduction properties of the fabricated ZnO NWFETs. The next chapter presents a literature review that charts the evolution of FET pH-sensor to FET biosensor. It also covers the function of FET biosensors and the major issue that biosensors encounter in their operation. One of those issue is voltage drift.

As stated above the main of aim this thesis is to develop an miRNA FET biosensor. Such a biosensor must be capable of operating in solutions, at physiological relevant concentrations, for long periods of time. The reason for this is three-fold. Firstly, the time scale of bio-molecule binding events at the surface of the FET increases as the concentration of the analyte decreases. Consequently, FETs must able to withstand detrimental effects, such as signal drift, of the harsh ionic environment in which it operates for an increased length of time in order to detect the desired bio-molecules. Secondly, the prospects of being able to reuse a FET-biosensor are greatly increased if it can work in at physiological relevant concentrations for $\geq$ an hour which, naturally, increases the commercial viability of theses device. Being able to reuse the device would diminishes the contribution of these devices to the growing e-waste crisis [65]. In Chapter 6, the outcomes of an investigation into the stabilising effects the $Al_2O_3/HfO_2/Al_2O_3$ layer on ZnO Nanowire Field Effect Transistors (NWFETs) operating in high ionic strength Phosphate Buffered Solution (10 mM phosphate, 150 mM KCl, pH 7.4) are presented. Detailed in chapter 7 is a record of the miRNA detection experiment conducted and results obtained. Also presented in Chapter 7 are the results of repeats of the miRNA detection experiment conducted and Chapter 8 concludes the thesis by summarising its major findings and ends by discussing future work given the results that have been achieved.

Chapter 2

MOSFET Function

2.1 Introduction

MOSFETs, as depicted in Figure 2.1, are typically comprised of a metal gate, a gate oxide, source, drain and bulk contacts. Voltages applied to the metal gate creates an electric field at the surface of the oxide inducing a change in conductance in the channel which forms between the source and drain. The relationship between the gate controlled drain current (I_D) flowing through channel and the gate (V_G) and drain (V_D) voltages is described by Equation 2.1. This equation holds under conditions where the drain current is less than the difference between the gate and threshold voltages ($V_D < V_G - V_T$) [66].

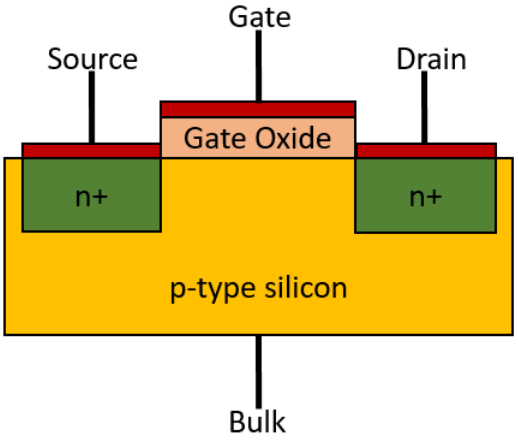

Figure 2.1: A cross-sectional schematic of the constituent parts of a typical MOSFET.

$$I_D = \frac{Z}{L}\mu_n C_{ox}(V_G - V_T - \frac{V_D}{2})V_D \tag{2.1}$$

Where μ_n= mobility of the minority carriers ($cm^2/V.s$); C_{ox}= Capacitance of the gate oxide per unit area (F); and Z and L are the gate width and lengths (m) respectively.

When $V_D \geq (V_G - V_T)$ the channel pinches off, resulting in the drain current saturating. That is, the drain current becomes constant, theoretically, irrespective of any increase in the drain voltage. When this occurs, the drain current is more accurately described by Equation 2.2 [66].

$$I_{Dsat} = \frac{Z}{2L} C_{ox} \mu_n (V_G - V_T)^2 \tag{2.2}$$

2.1.1 Thin Film Transistor

Thin-film Transistors (TFTs) are a subset MOSFET. While there is no difference in the function of TFTs and the structure depicted in Figure 2.1 there is a difference in how they are fabricated. TFTs are fabricated by depositing layers of material on a substrate to form a semiconductor Figure 2.2. In contrast, to fabricate the MOSFET structure described above, a silicon substrate is subjected to high temperature doping process steps to form the different regions of the semiconductor. An example of this difference in fabrication methods is that the source and drain on a TFT can be formed by ohmic contacts with a lifted off metal layer. In the MOSFET structure described above, the source and drain are doped n+ regions in a p substrate.

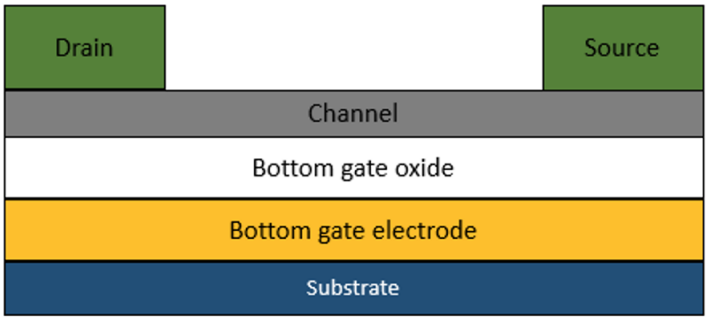

Figure 2.2: A cross-sectional schematic of a TFT.

2.2 Threshold Voltage

The threshold voltage of a MOSFET is the minimum voltage applied at the gate which enables the channel to conduct a significant amount of current. It is qualitatively described as the gate bias, beyond the flatband voltages, at which point an inversion charge sheet is induced. Equation 2.3 shows how the threshold voltage is calculated [66].

$$V_T = V_{FB} + 2\Psi_B + \frac{\sqrt{2\epsilon_S q N_A (2\Psi_B)}}{C_{ox}} \tag{2.3}$$

Where $2\Psi_B$ is the bulk potential. The square-root term is the total depletion-layer charge and is comprised of the dielectric constant of the semiconductor ϵ_S, the elementary charge q ($1.60218 \times 10^{-19} C$), the acceptor concentration N_A (cm^{-3}) and the bulk potential. V_{FB} is the flat band voltage

and is calculated as the difference between the work function of the gate metal qϕ_m (eV) and the work function of the semiconductor material qϕ_s (eV) Equation 2.4.

$$V_{FB} = q\phi_m - q\phi_s \tag{2.4}$$

2.3 Regions of Operation

As mentioned above, the current flowing through the channel is controlled by the gate and drain voltages. Depending on the value of each of these voltages, the MOSFET is biased to operate in one of the three regions depicted in the Figure 2.3. In the subthreshold region, when the gate voltage is several tenths of a volt less than the threshold voltage, the drain current follows an exponential dependence on the gate voltage [67]. This area of the subthreshold region where the surface potential Ψ_s is $\Psi_B \leq \Psi_s \leq 2\Psi_B$ is called the weak inversion region. The subthreshold slope characterises the ability of the transistor operating in weak inversion region to transduce a change in gate voltage into a change in drain current. It is defined as the gate voltage needed to change the drain current by a factor of ten for a constant drain voltage. The value of the subthreshold slope SS can be found by calculating the inverse slope of the linear part of a $\log_{10} I$ versus $\mathrm{V_G}$ graph or by using Equation 2.5 [68]:

$$SS = \frac{\partial V_G}{\partial(log_{10} I)}\bigg|_{V_D} \tag{2.5}$$

The subthreshold slope indicates the ability of MOSFET operating in the subthreshold region to transduce a change in charge at the gate into output current. The smaller this value is, the greater the output current a MOSFET would produce for a given amount of charge at the gate oxide.

For a constant drain voltage the transconductance , $\mathrm{g_m}$ (S), given in Equation 2.6 measures the change in drain current over a range of gate voltages.

$$g_m = \frac{\delta I_D}{\delta V_G}\bigg|_{V_D} = \mu_n C_{ox} \frac{Z}{L} V_D \tag{2.6}$$

where μ_n= mobility of the minority carriers; $\mathrm{C_{ox}}$= Capacitance of the gate oxide; and Z and L are the gate width and lengths respectively. From the Equation 2.6 mobility can be calculated, which measures the rate at which charge carries move through the channel. Transconductance is constant in the linear region and as such it is useful for describing how the drain current varies with the gate voltage in this region.

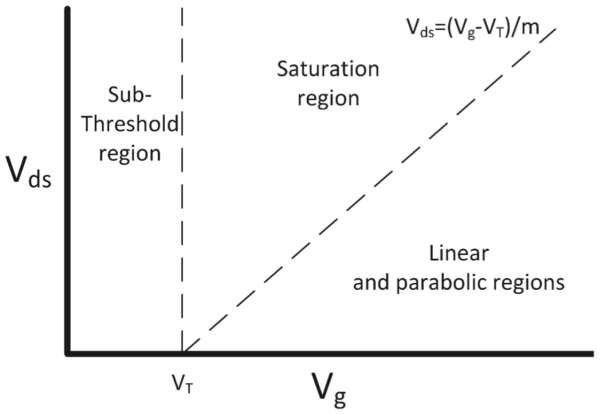

Figure 2.3: Regions of operation of a MOSFET where V_G, V_T, V_{ds} are the gate voltage, threshold voltage, drain voltage respectively and $m = 1 + \frac{\sqrt{\epsilon_S q N_A (4\Psi_B)}}{C_{ox}}$ [67].

2.4 MOSFET Material

MOSFETs, as depicted in Figure 2.1, are typically fabricated with Silicon. Silicon underpins the semiconductor industry, with a 90% share of the market. Its material properties are regarded as an excellent compromise between performance and stability [69] and its ubiquitous presence in the semiconductor industry is due to the fact that fabrication processes involving silicon are well understood and are relatively cheaper than processes involving other semiconductor materials [68]. In the following sections the material properties of Zinc Oxide (ZnO) are detailed along with the case for using ZnO instead of Silicon in the fabrication of the nanowire arrays.

2.5 Zinc Oxide Material Properties

ZnO is a naturally occurring material, pervasive in nature, which crystallizes in either cubic, zinc-blende or hexagonal wurtzite structure. In its zinc-blende and hexagonal forms, each anion is covalently bonded to four cations at the corners of a tetrahedron, and vice versa. These structures are known to have a substantial ionic character because of which, ZnO is considered to be an II-VI compound semiconductor whose ionic characteristics resides at the border of covalent and ionic semiconductor. In ambient conditions, it is most thermodynamically stable in its wurtzite phase Figure 2.4.

ZnO has a direct and large band-gap making an attractive material for electronic applications. This is because its large band-gap (3.37 eV) gives this material the ability to sustain large electric fields and withstand higher breakdown voltages, while enabling lower noise generation, and high temperature and power operation [17]. As ZnO has a larger band-gap than Silicon (1.12 eV) [69] it is less prone to thermal noise. Undoped ZnO in its wurtzite form is naturally a n-type semiconductor. The long held assumption was that the source of this n-type property were the oxygen vacancy or interstitial Zn site native defects [15]. While a consensus has yet to reached, it has been suggested that Zn-sublattice

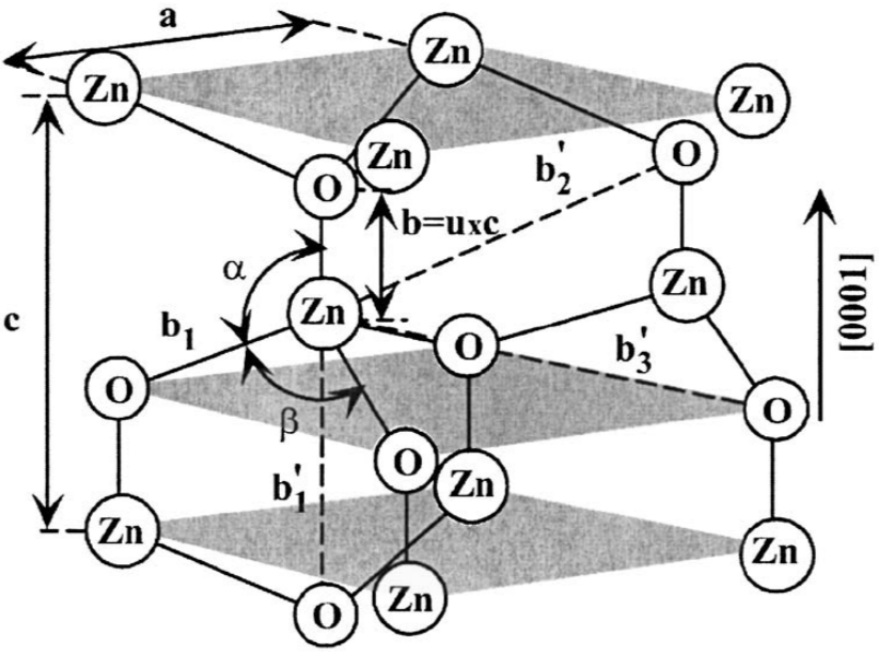

Figure 2.4: A Schematic of ZnO in its wurzite structure. In this form it has lattice constants (a) in the basal plane and (c) in the basal direction. The parameter, u, is expressed as the bond length (b) divided by c (0.375 in ideal crystal). α and β (109.47 in ideal crystal) are the bond angles. [17]

(interstitial Zn) defects rather than oxygen vacancy defects are the dominant native shallow donor in ZnO [70]. More recently, experimental data has been generated which suggests that the n-type property of ZnO emanates from an alternative donor. Walle [71] reached the conclusion that hydrogen acts as the source of conductivity as it is incorporated in the ZnO structure in high concentrations and it behaves as a shallow donor. As ZnO is naturally a n-type semiconductor there is no need for doping, a costly high temperature $(900 - 1200^{o}C)$ process [72]. Consequently, ZnO FETs can be fabricated at considerably lower temperatures of $\leq 250\ ^{o}C$ as is presented in Chapter 3.

2.6 Conclusion

In this chapter we looked at the structure and function of MOSFETs. This was followed by a brief discussion of the merits of fabricating MOSFETs with ZnO instead of Silicon, the material that is typically used. The following chapter details the process by which Zinc Oxide (ZnO) Nanowire Field Effect Transistors (NWFETs) arrays were fabricated at low temperature.

Chapter 3

Fabrication

3.1 Introduction

In a recent paper [73], Ebert et al used a novel dry etch, lift off technique to simultaneously generate Zinc Oxide (ZnO) nanowire field effect transistors (NWFETs) arrays of varying numbers. This chapter details how this low-cost, low temperature, top-down fabrication process was implemented to fabricate ZnO NWFETs to be used in bio-sensing applications. The rationale behind adopting a nanowire configuration is also explained in this chapter.

3.2 Process Flow

The fabrication process began with growing 100 nm of Silicon Dioxide (SiO_2) by the dry oxidation of CZ(100) silicon wafers at 1000 ^oC. A 90 nm layer of Aluminium Zinc Oxide (AZO - 5% Al, 95% ZnO) was then deposited, by Plasma Enhanced Atomic Layer Deposition (PEALD). AZO was deposited at 175 ^oC in 520 cycles of 125 ms DEZ pulses, 5 s DEZ purge, 150 ms H_2O pulse, 5 s H_2O purge; and 26 cycles of 20 ms TMA pulses, 3 s TMA purge, 100 ms H_2O pulse and a 8 s H_2O purge. This AZO layer was wet etched to form individual bottom gate electrodes for each NWFET array. Wet etching was done in a bath of Hydrochloric (HCl) acid and water mixed in a ratio of 1:1000 ($HCl : H_2O$). The original concentration of the HCl before dilution was 37% HCl:H2O.

AZO was an ideal candidate for the gate electrode as it has a relatively low resitivity ($1.25\ m\Omega \cdot cm \pm 0.2\ m\Omega \cdot cm$), does not contain any toxic elements such as Indium and is cheaper than Indium Tin Oxide and Gold [74]. 50 nm of Al_2O_3 was deposited by PEALD and etched by Argon Ion Beam Etch (IBE) to form the bottom gate oxide. The Al_2O_3 layer was etched at a rate of 4 nm/min using a four step etch process with a beam current of 300 mA, beam voltage of 500 V, 400 V beam accelerator, 550 mA neutralizer, 500 W RF, and at 5 ^oC platen temperature.

Al_2O_3 was chosen because it has a high dielectric constant(K = 9) and a large band gap (8.8 eV) [75] which are an important factors in reducing gate leakage currents [76]. Al_2O_3 was deposited at

150 °C with 500 cycles of 30 s O2 clean, 20 ms TMA, 3 s TMA-purge, 3 s O_2 plasma 300 W RF, 1 s O_2-purge, 15 mTorr and 60 sccm O2.

The novel dry etch, lift-off technique developed by Ebert requires 2 layers of resist to be fashioned into a non-reversible template. Lift-Off-Resist (LOR1A), manufactured by Microchem Corp. was spun at 5000 rpm to form a 100 nm thick layer. As LOR1A consists of polymethylglutarimide (PMGI), which is not sensitive to UV exposure. This bottom layer, which would serve as sacrificial thin film, exhibits good adhesion and high-temperature stability. It is also compatible with g-,h-,i-line wavelength photoresists and can be developed with standard tetramethylammoniumhydroxid (TMAH) based developer solution [175].

Following on, the AZ2070 1:1.33 AZ EBR resist, manufactured by Microchemicals GmbH, was then spun at 5000 rpm producing a 400 nm thick layer. AZ2070 1:1.33 was chosen because of the target nanowire dimensions and because it provides very high stability against thermal softening. This layer of negative resist was exposed to UV light with 40 $mJcm^{-2}$ intensity, baked and then developed in diluted AZ 726([1:2] H2O: AZ 726) for 55 s. A chrome/quartz mask was used in hard contact with the sample. The remaining AZ2070 1:1.33 was hardened by flood U.V. exposure and baked for 75 s at 150 °C. This was to ensure that the layer of negative resist would be preserved in the subsequent development and etching steps. The subsequent development step removed exposed LOR1A to create a gap in which the nanowire would be deposited. In order to obtain a 30 nm thick nanowire, the thickness of the gap in the LOR1A layer needs to be at least 100 nm high to ensure an unobstructed deposition of the ZnO. The exposed LOR1A was developed in diluted AZ 726([1:2] H2O: AZ 726) for 55 s.

PEALD was used to deposit the ZnO in 218 cycles with a 100 ms diethylzinc (DEZ, $Zn(C_2H_5)_2$) pulse, a 4 s DEZ purge, a 2.65 s oxygen plasma step with 100 W RF power and a 4 s oxygen purge. PEALD was chosen as the method of deposition because it produces a conformal deposition of ZnO allowing the deposited material to fill the patterned gaps in the photoresist bi-layer. Following the deposition the layer of ZnO atop the photoresist was etched anisotropically in an argon ion beam etcher (IBE) . IBE was used instead of a plasma etching technique because IBE prevents unwanted uncontrollable side effects such as charging. IBE was also preferred to etching with CHF3 and Cl2 prevent the reaction of the ZnO with the photoresist which would leave difficult to remove residues such as zinc fluoride (ZnF_2) and zinc chloride ($ZnCl_2$) [34]. Using a two step etch process with a beam current of 300 mA, beam voltage of 500 V, 400 V beam accelerator, 550 mA neutralizer, 500 W RF, 5 °C platen temperature, the exposed ZnO layer was etched at a rate of 17 nm/min.

Following the etch step, the remaining bilayer resist was lifted off the samples was performed in beakers of 1-Methyl-2-pyrrolidinone (NMP), at 80 °C, leaving behind the nanowires with the following dimensions on average: thickness =30 nm, length =170 μm, width =250 nm. The schematic in Figure 3.1 describes the process by which the nanowires were fabricated. With the nanowires in place, 15 nm of AZO (2 % Al, 98 % ZnO) followed by 500 nm of Aluminium (Al) was sputtered, at room temperature, and fashioned into the source, drain and bottom gate contacts as well as source

and drain electrodes. Al was chosen because it is conductive, relatively cheap material that can be easily acquired.

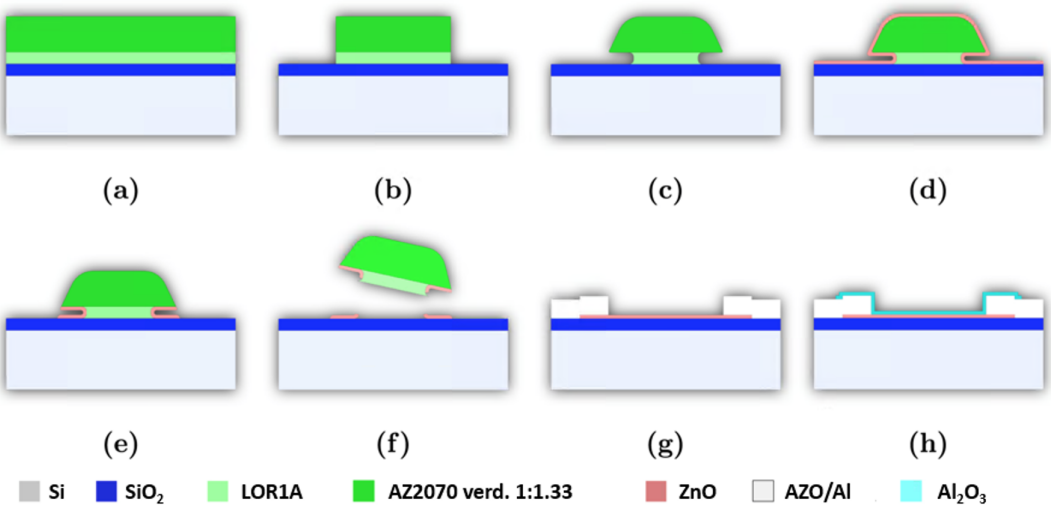

Figure 3.1: Schematic process flow cross section of (a) spun LOR3A and diluted AZ2070 on oxidized silicon wafer, (b) resist pattern after first development, (c) resist pattern after hard-baking and second development, (d) ZnO-coated resist pattern by PEALD, (e) anisotropic dry etched pattern, (f) resist lift-off process, (g) metal pad formation along the nanowire, (h) deposited and structured Al2O3 layer along the nanowire.[73]

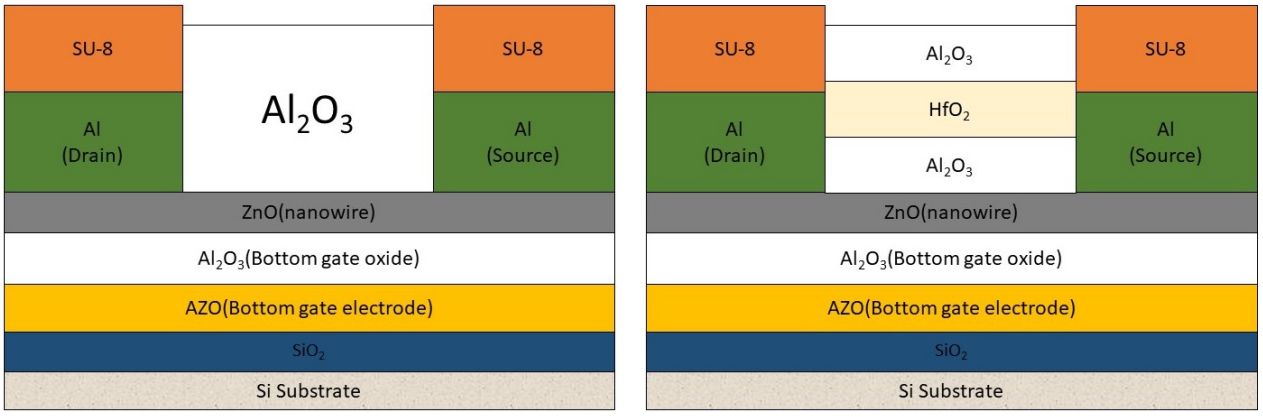

Figure 3.2: (a) Cross section schematic of the ZnO NWFETs with the Al_2O_3 passivation layer. (b) Cross section schematic of the ZnO NWFETs with the $Al_2O_3/HfO_2/Al_2O_3$ stack passivation layer.

At that juncture, 24 nm of Al_2O_3 was deposited by PEALD on the NWFETs on one substrate Figure 3.2(a). On the devices on the other wafer, a dielectric stack comprised of a 4nm layer of HfO_2 sandwiched between two 8nm layers of Al_2O_3 (AHA) was deposited Figure 3.2(b). Discussed in Chapter 6 are the results of experiments conducted to ascertain whether there was a difference in stability offered by the AHA passivation layer compared Al_2O_3 passivation layer when the NWFETs were operating in electrolytes of 150 mM ionic concentration. Although HfO_2 has a much larger dielectric constant than Al_2O_3 [75] it does suffer from non-ideal effects namely, hysteresis phenomenon

[77]. Al_2O_3 has been shown to have a stronger resistance to these non-ideal effects [78] than HfO_2 and is also known to be more compatible with 3-Aminopropyltriethoxysilane (APTES), a commonly used cross linker molecule, thus a greater number of biomolecules can be immobilised at the surface of an Al_2O_3 insulator than a HfO_2 insulator [79].

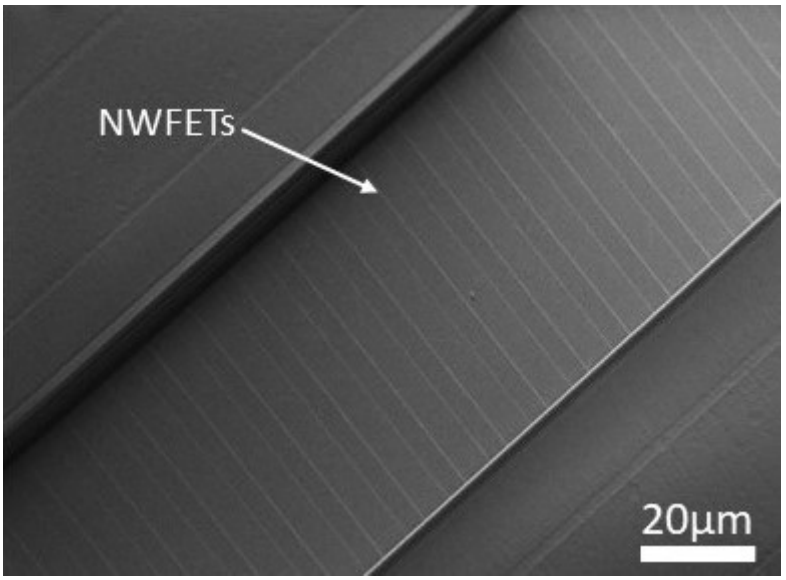

(a)

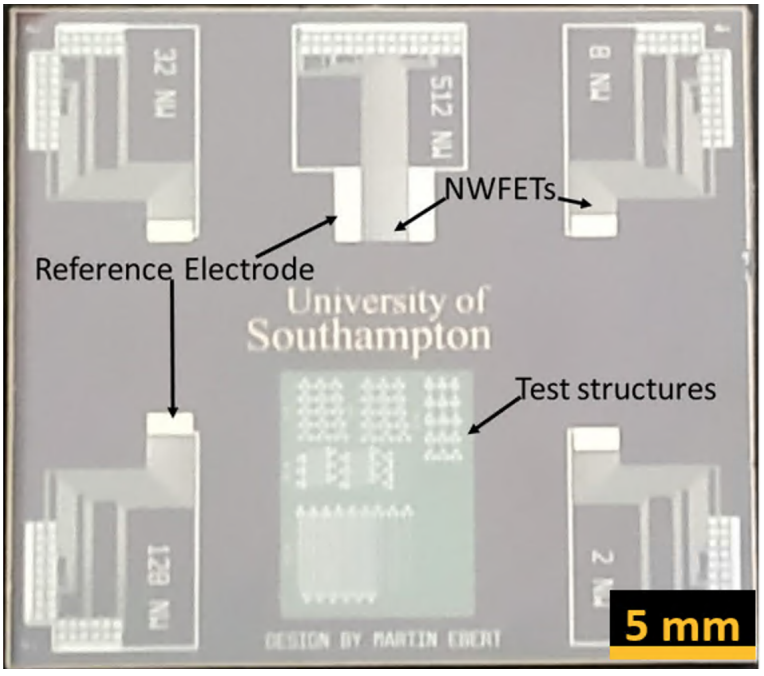

(b)

Figure 3.3: (a) Top view scanning electron micrograph of NWFETs. (b) A diced chip carrying the fabricated ZnO NWFETs. The dimensions of the chip are 23 mm by 25.7 mm.

It is for these reasons that Al_2O_3 was used as the single material insulator layer and the sandwich configuration was adopted for the stack insulator layer, in order to minimise the amount of HfO_2 used. HfO_2 was deposited at 200 °C with in 8 cycles of 1.75 s TEMAH dose with 250 sccm Ar bubbler, 8 s

TEMAH purge at 15 mTorr, 2 s O_2 plasma at 600 W, 2 s purge N_2 100 sccm and Ar 250 sccm at 80 mTorr.

After passivation, SU-8 was spun onto each wafer, patterned and then developed to demarcate the sensing around the NWFETs to keep analyte in an area where they can be detected. The wafers were then scribed into chips Figure 3.3(b). On each chip are 5 groups of NWFET arrays. Each array within a group has the same number of nanowires but different gate electrode lengths. The groups were as follows 2, 8, 32 , 128 and 512 nanowires with gate lengths of 20, 30, 40, 60 and 90 μm within each group. The 512 and 128 nanowire arrays were intended to used in bio-detection experiments as device performance had been seen to correlated with the number of nanowires [73]. Of these 200 devices fabricated per wafer, the yield was approximately 5%. This figure assume that no devices were lost during scribing.

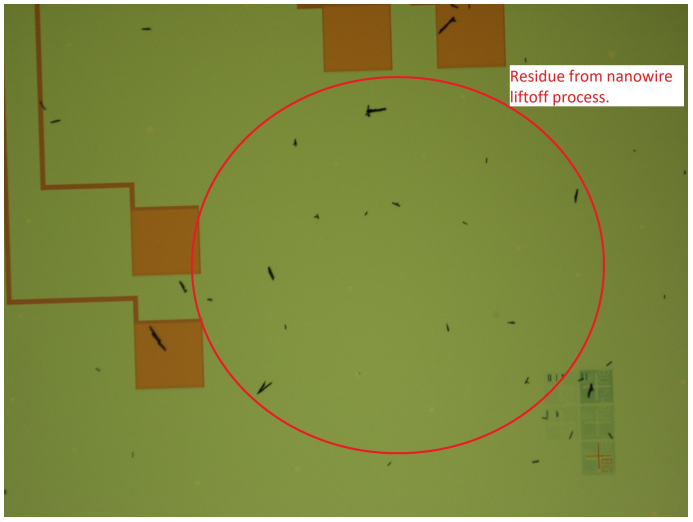

(a)

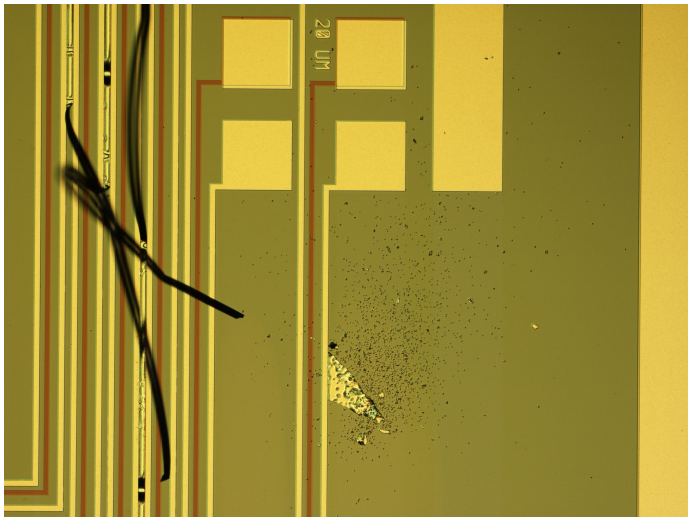

(b)

Figure 3.4: (a) This diagram shows residue resulting from the re-deposition of lift-off resist. (b) This diagram shows the black residue resulting from incomplete lift-off of resist and sputtered AZO and Al.

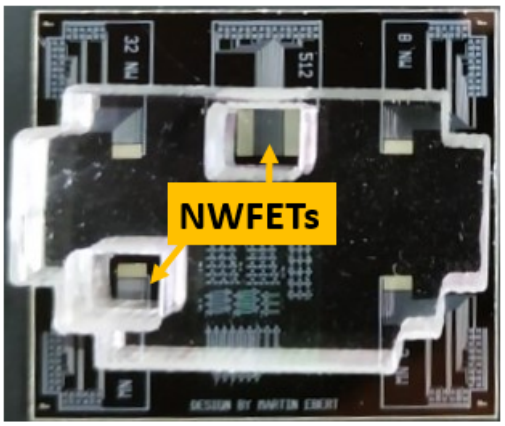

Figure 3.5: A chip of ZnO NWFET arrays underneath sheets of PMMA.

The fabrication process detailed above was not devoid of mishaps. The main issues encountered were the re-deposition of resist during the ZnO liftoff process Figure 3.4(a); and failing to completely lift-off sputtered AZO and Al deposited on top of resist Figure 3.4(b). The residue may have contributed adversely to the performance of the fabricated devices. However, it was impossible to run electrical characterisation measurements (I_DV_G and I_DV_D sweeps) to quantify the effect residue has on the performance of the NWFETs as the fabrication process had not been completed when these issues arose. At the end of the fabrication process laser cut poly methyl methacrylate (PMMA) was to chips to be used in subsequent experiments Figure 3.5. The PMMA sheets were laser cut to form windows, through which to pipette the buffer, pH and analyte samples onto the surface of the NWFETs. Double sided adhesive transfer tape manufactured by 3M was used to bond the PMMA channels the chip.

3.3 Nanowire Configuration

The notion that increasing the surface area to volume ratio of an bioFET increases its sensitivity to analyte[76] is supported by results from experiments where devices were biased in the linear region [80], [81], [82]. This was the main reason for adopting a nanowire configuration for the FETs. Secondary reasons for adopting a nanowire configuration included demonstrating a novel, low cost, low temperature (190 °C), top-down fabrication process. This process enabled the fabrication of NWFET arrays using a bi-layer photoresist pattern with a retrograde profile instead of electron beam lithography. While these were good reasons to adopt a nanowire structure unfortunately, the design of the NWFETs was sub-optimal for their proposed application. While a NWFET array covers the same geometrical area as a planar device would, there are gaps between the wires of a NWFET array which are not present in a planar device. These gaps are approximately 5 μM wide which is at least 3 orders of magnitude of larger than the size of the analyte being detected in this thesis. Thus, it is highly probable that there would be analyte binding to surface of the NWFETs in these gaps which would not have been detected. It has been shown that increasing a device's surface to volume ratio contributes to the enhanced binding kinetics of the analyte, thus reducing the device's response time [83]. However, if the analyte were to adsorb to the surface in the gap between the nanowires it would

not detected given that the Debye length would be nanometres long and the gap is microns wide. Thus, the reasons for adopting a nanowire configuration such as a decreased response time would be a non-factor in this scenario. This design flaw (micron-wide gaps between nanowires) was only noticed in hindsight and given the limited amount of time and resources available, the decision made to carry out the investigations presented in this thesis in spite of this flaw.

3.4 Conclusion

In this chapter the process by which ZnO NWFET arrays were fabricated was detailed. The next chapter focuses on the mechanism by which FETs detect charge particles be they protons, proteins or DNA strands. From a historical perspective the Ion Sensitive Field Effect Transistor (ISFET) is the precursor to the bioFET. So, we begin the subsequent chapter by exploring the structure of ISFETs before unravelling its the sensing mechanism. ISFETs are typically used in pH-sensing experiments. The shift in the gate voltage per pH change is used in determining the efficacy with which an ISFET transduce the the charge at its gate. The chapter is concluded with a discussion of the results obtained from a pH-sensing experiment involving the fabricated ZnO NWFETs.

Chapter 4

pH sensing: An application of FET Sensing

4.1 Introduction

Chemical sensors are deployed in a wide range of application domains such as food safety [32], medical diagnostics [20], environmental monitoring [31] and explosives detection [84]. A class of chemical sensors are based on the FET, the earliest of which were developed in 1970s by Bergveld [85] [86]. In these FET-sensors, which were termed Ion Sensitive Field Effect Transistors (ISFET), the gate electrode of the MOSFET was replaced with a reference electrode and an electrolyte [87] Figure 4.1.

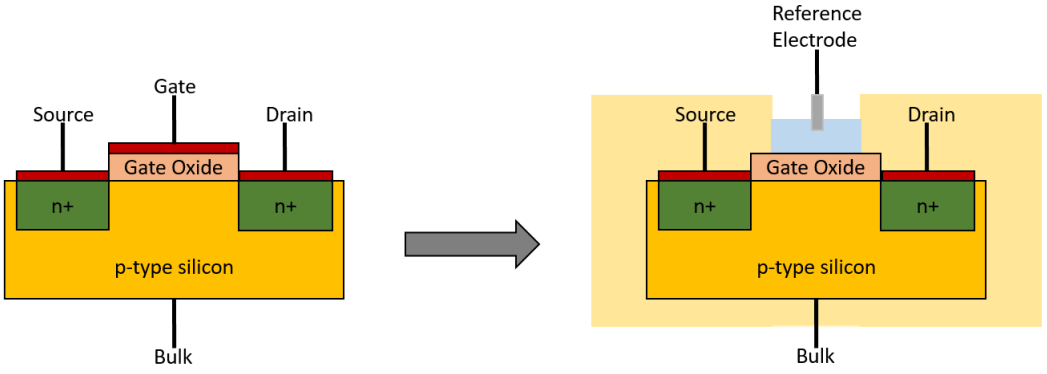

Figure 4.1: This diagram depicts the changes made to MOSFETs to obtain an ISFET. The gate electrode in a MOSFET was replaced by an electrolyte and a reference electrode.

4.2 ISFET Function

In similar manner to the gate of the MOSFET, the reference electrode of an ISFET is used to bias the channel. Positive voltages at the reference electrode results in the formation of a conductive channel beneath the oxide-electrolyte interface for n-channel devices. Apart from biasing the channel,

the reference electrode is used to provide a stable potential in the electrolyte[68]. An ideal reference electrode is assumed to be Faradaic in its operation. That is, the exchange of electrons between the electrolyte and the electrode occurs such that there is controlled potential drop at this interface. This means that a fixed electrostatic potential applied is dropped at the electrolyte-oxide interface [88]. Furthermore, it assumed the that the potential at the electrode–electrolyte interface is insensitive to changes in the electrolyte solution. The electrolyte is a composition of ions in an aqueous solution Figure 4.2. Its function is to maintain the pH of the system in order that the ISFET produces a reliable response.

While the expression for the drain current (Equation 2.1) of a non saturated MOSFET remains the same for ISFET in non-saturated mode, some additional terms are added to the threshold voltage equation of an ISFET Equation 4.1:

$$V_T = E_{ref} - \varphi + \chi^{sol} - q\phi_s + 2\Psi_B + \frac{\sqrt{2\epsilon_S q N_A (2\Psi_B)}}{C_{ox}} \tag{4.1}$$

E_{ref} (V) is the constant potential of the reference electrode which replaces the work function the gate metal $q\phi_m$ (eV); χ^{sol} (V) is a constant representing the dipole potential of the solvent at the oxide-electrolyte surface; and $2\Psi_B$ (V) is the bulk potential. ϵ_S is the dielectric constant of the semiconductor, q $(1.60218 \times 10^{-19} C)$ is the elementary charge, C_{ox} is the capacitance of the gate oxide per unit area (F), and N_A is the acceptor concentration. φ (V) represents the surface potential at the oxide-electrolyte surface which is the only term in Equation 4.1 which is a function of the pH of the electrolyte [89]. That is to say when ISFETs are wetted with electrolytes of different pH levels, its threshold voltage changes in response to changes to surface potential at the oxide-electrolyte interface.

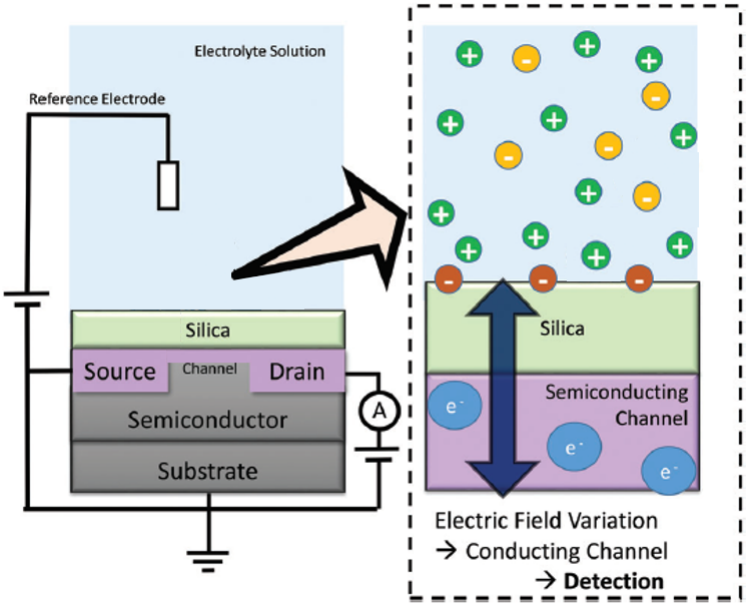

Figure 4.2: A schematic of ISFET operation. Variations in H^+ ion concentration can alter the electric field at the oxide-electrolyte interface, resulting in a measurable change in conductance of the channel.[90]

4.3 Sensing Mechanism

To elucidate the oxide-electrolyte interface phenomena Yates et al developed the Site-Binding Model [91]. In this model, the gate oxides were described as being amphoteric. Thus, the hydroxyl groups at the surface of the oxide could be either neutral, positively charged (protonized), or negatively charged (deprotonized), depending on the pH of the electrolyte. That is, the protonation states of the hydroxyl groups changes with as the pH of the surrounding electrolyte changes. According to the site-binding model, the relationship between the pH and the surface potential, φ, at the oxide-electrolyte interface is given by Equation 4.2 [92].

$$\varphi = 2.3(kT/q)\frac{\beta}{\beta+1}(pH_{pzc} - pH) \tag{4.2}$$

where pH_{pzc}, the point of zero charge, is the pH value for which $\varphi = 0$; k ($1.38066 \times 10^{-23} J/K$) is the Boltzmann constant; T (K) is the absolute temperature; q ($1.60218 \times 10^{-19} C$) is the elementary charge; β (mol) is a parameter which reflects the chemical sensitivity of the gate insulator and is dependent on the density of surface hydroxyl groups and the surface reactivity. β is referred to as buffering capacity of an oxide and it indicates the ability of an oxide to deliver or take upon protons [93].

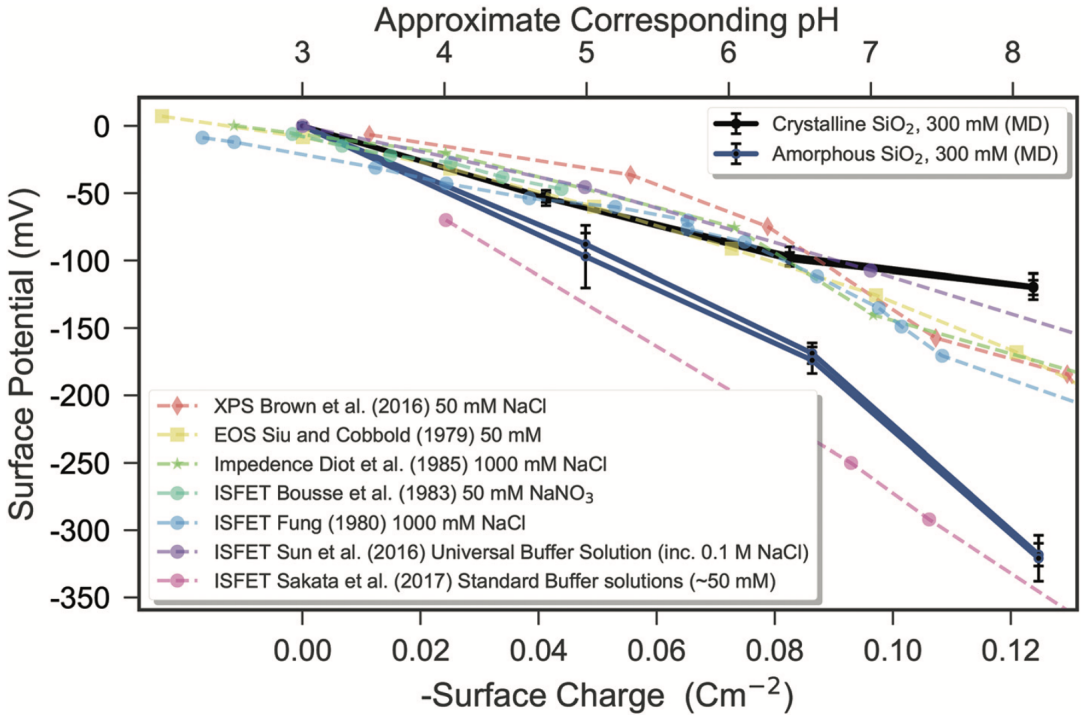

Figure 4.3: A comparison of the surface potential simulated via molecular dynamics (solid lines) with experimental data (dashed lines) as a function of surface charge. The simulated surface potentials are presented relative to the system with no surface charge by subtraction of the surface potential for the zero surface-charge system [94]

The pH-dependent surface potential modulates the channel conductance, and by extension, the drain current I_D, of the ISFET. By measuring changes in the drain current, changes in the pH value of the electrolyte can be observed. Alternatively voltage shift can be recorded when the drain current is set at a fixed value [92]. Lowe et al [68] highlighted Equation 4.3 which had been presented in the following articles [95] [96]. This equation, estimates the change in threshold voltage in response to a change in pH for an ISFET operating in the subthreshold region. It expresses the relationship between the change in threshold voltage (ΔV_T), the subthreshold slope SS ($Vdec^{-1}$), and the normalised change in drain current $I_{norm}(A)$.

$$\Delta V_T = SS(log_{10}(I_{norm} + 1)) \tag{4.3}$$

Given ISFETs of differing subthreshold slopes, Equation 4.3 highlights that at a fixed reference electrode voltage, ISFETs with a smaller subthreshold slope will have larger changes in drain current than ISFETs with a larger subthreshold slope. This is the case assuming the subthreshold slope remains constant when ISFET is wetted with the electrolyte and the threshold voltage change per unit pH remains constant. The response of an ISFET with a constant subthreshold slope is a parallel shift in the I_DV_G characteristics of that ISFET as observed by Zeimpekis [97]. Remarkably, the threshold voltage change per unit pH has been observed to be distinct property of the oxide material, with ISFETs with a Silicon dioxide and Hafnium Dioxide oxide layers consistently producing responses of 30-40 mV/pH [96] [98] [99] and 56-59 mv/pH [95] [100] [101] respectively.

This material consistent surface potential shift is explained using the site binding model, in which the density of surface hydroxyl groups determines the surface potential shift per unit pH. Hence larger surface potential shift per unit pH denote higher densities of surface hydroxyl groups [102]. This explanation is supported by empirical evidence where a decrease in surface potential shift per pH is observed when surface hydroxyl groups are blocked by organic molecules [102] [103]. While site-binding models are widely used, they do have a number of limitations. These models employ empirical parametrisation of a couple of properties such as the acid–base dissociation constant of the oxide and density of surface sites. These properties can vary greatly for each individual material and the latter property is preparation dependent [94]. Site binding models also do not factor in surface morphology which has been seen in Molecular Dynamic simulations to have a marked effect in the surface potential shift per unit pH.

In a Molecular Dynamics simulation of the oxide-electrolyte interface, Lowe et al [94] observed that increases in surface charge density (a proxy for the effective pH of the electrolyte) resulted in an increasingly negative surface potential Figure 4.3. This increasingly negative surface potential is reflected in changes in the threshold voltage as the carrier concentration in the channel is modulated accordingly Figure 4.2. They adopted an empirical relationship (a first order approximation treated as a linear relationship) between surface charge density and the corresponding effective pH as presented by Emami et al [104] [105]. Crucially, in accounting for surface morphology it was seen that the crystalline and amorphous simulations approximately achieved a 25–45 mV per effective pH shift and a 59 mV per effective pH shift, respectively, in pH range 3–8. The difference in voltage per effective

pH shift between the crystalline and amorphous simulations was explained by the amorphous system showing higher sodium ion accumulation. This was attributed to the the amorphous surface having a larger surface area with more cavities thus, providing more favourable surface adsorption sites [94]. It was suggested that the results of the simulation might provide a theoretical explanation for why sputtered silica was seen to provide an enhanced pH response compared to thermally grown silica [106]. It should be noted that further experimental work is required to clarify the precise relationship between surface morphology and the surface potential shift per unit pH.

4.4 Experiment

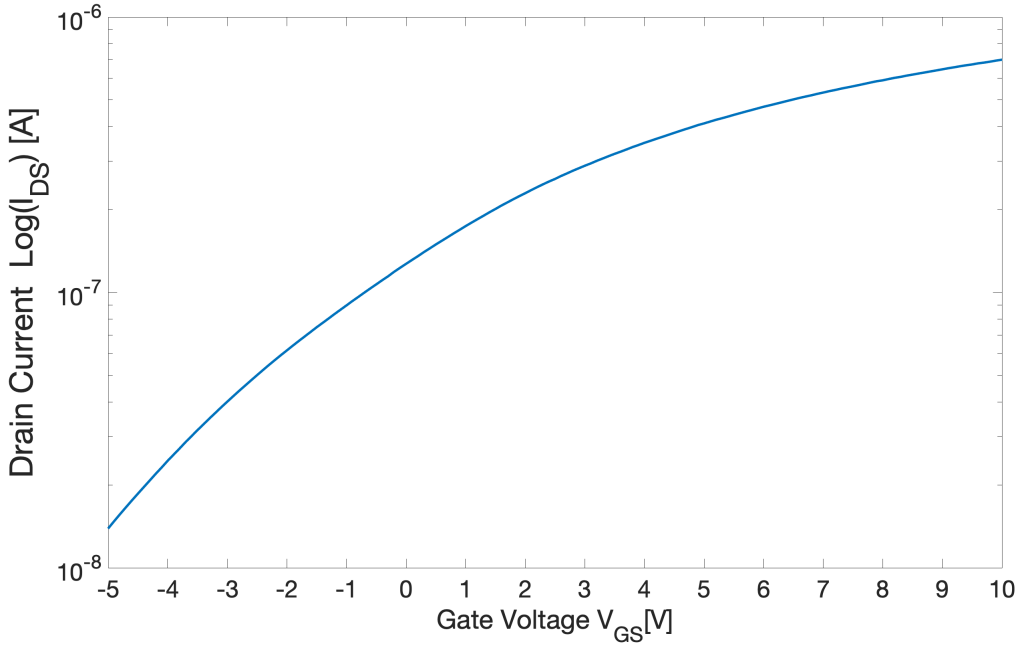

Figure 4.4: I_DV_G curve of the ZnO NWFET array before the pH sensing experiment. The I_DV_G sweep was conducted in dry conditions. Drain voltage =5 V

After fabricating the ZnO NWFETs there was a need to establish that these NWFETs were effective transducers of ionic charge in aqueous conditions. To that end a pH sensing experiment was conducted where the surface of a NWFET array was wetted, consecutively, with solutions of pH 9, 7, 5, 3 (increasing H^+ ions concentration) for five minutes (300 s) per solution. The NWFETs array used was comprised of 128 nanowires was biased with a 4 V bottom gate voltage and a 5 V drain voltage, producing a 349 nA current and positioning the NWFETs the edge of the subthreshold region Figure 4.4. FET pH sensors have been shown to be most sensitive to changes in H^+ ion concentration when operating in the subthreshold region [99]. Moreover, it enabled the NWFETs to be used as a low power device. All electrical measurements were conducted in a dark environment, at room temperature, using the Keysight Semiconductor Parameter Analyzer (B1500A).

4.5 Results and Discussion

As is observed in Figure 4.5, the current output of these n-type ZnO NWFETs increased as the pH decreased. This occurred because, as the pH decreased, there was an increase in the concentration of H^+ ions in the bulk solution and at the surface of NWFET. The increase in H^+ ions concentration led to increased protonation of hydroxyl groups at the surface of the oxide thus increasing the positive surface density charge [94] [107]. The increase in the protonation of hydroxyl groups, as the pH decreased, had the effect of increasing the positive bias on the n-type ZnO NWFETs. Consequently, an increase in output current was observed as pH decreased.

After five minutes (300 s) of measurement, the current levels for each pH appeared to be stable given that, over that time, current levels had decreased by, at most, 0.02 μA. With reference to I_DV_G curve Figure 4.4 which was used to set the bias point of the NWFETs (gate= 4 V; drain = 5 V), the current values sampled at 300 s were used to obtain the shifts in gate voltages. This is to say, the current values sampled at 300 s for each pH were mapped to a corresponding gate voltage using the I_DV_G curve. The difference between these gate voltages and the bias gate voltage (Gate Voltage shift [mV] in Table 4.1) were used to plot the voltage shift against pH graph in Figure 4.6.

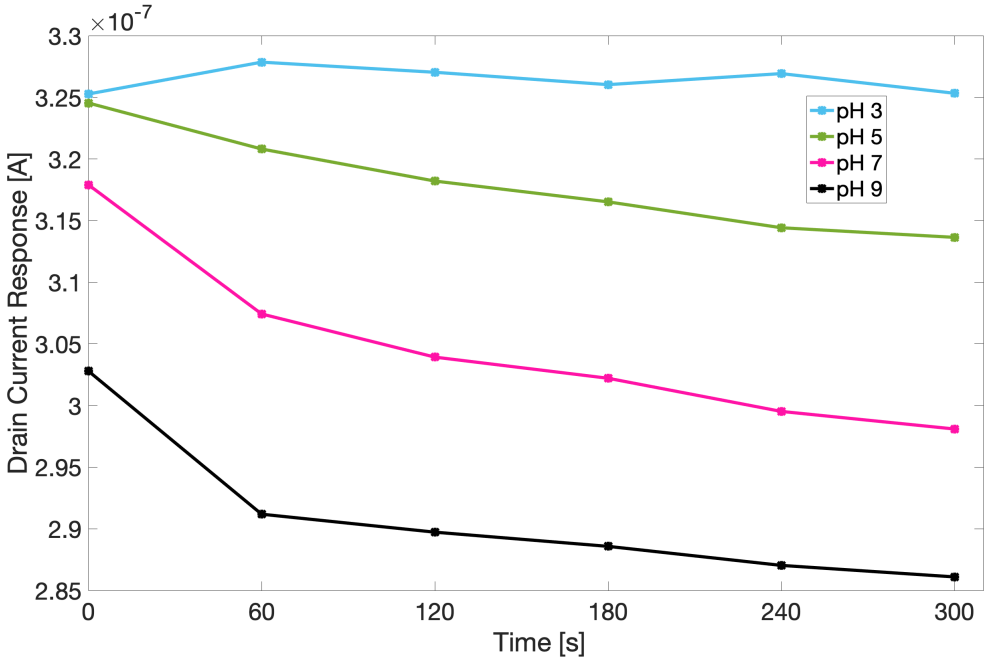

Figure 4.5: The current response of the NWFETs to changes in pH. The lines joining the points are eye guides.

Table 4.1: A summary of results of the pH sensing experiment quoted to 3 significant figures.

pH	Current at 300 s [nA]	Corresponding Gate Voltage [mV]	Gate Voltage shift [mV]
3	325	3600	400
5	314	3400	600
7	298	3100	900
9	286	2900	1100

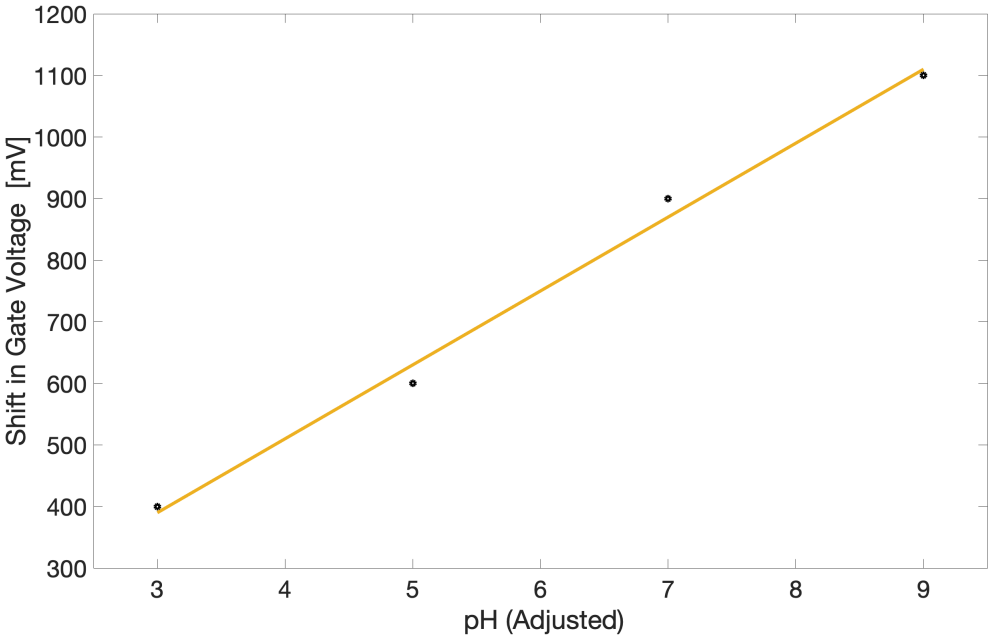

Figure 4.6: A graph of the gate voltage shift as pH is varied. The gradient of the curve is 117 mV/pH.

The gradient of the regression line is 117 mV/pH. This shift in gate voltage per pH is comparable with the 220 mV/pH recorded by Knopfmacher's single Silicon NWFET with a Dual Gate [19], and it is twice as large as the Nernst limit (59 mV/pH). The Nernst equation Equation 4.4 expresses the relationships between the change in surface potential $\Delta\varphi$ at the oxide-electrolyte interface resulting from a change in pH. k ($1.38066 \times 10^{-23} J/K$) is the Boltzmann constant; T (K) is the absolute temperature; q ($1.60218 \times 10^{-19} C$). The theoretical maximum pH sensitivity, $\Delta\varphi/\Delta pH = 59\ mV/pH$ (Nernst limit) , is derived from this equation [108].

$$\Delta\ \varphi = 2.303(\frac{kT}{q})\Delta\ pH \tag{4.4}$$

Like Knopfmacher et al, we attribute the large shift in gate voltage per pH to the relatively high buffering capacity of the Al_2O_3 layer which is the outermost layer of the stack insulator. The buffering capacity of an oxide refers to the ability of an oxide to deliver or take upon protons [93]. Buffering capacity determines the magnitude of the change in surface charge as pH is varied, with larger changes in surface charge resulting in larger shifts in gate voltages per pH. It also important to note the contribution of the HfO_2 layer in the stack insulator which has been shown to improve the subthreshold slope and enhance gate voltage shifts per change in analyte concentration [79]. To summarise, a super-nernstian gate voltage shift per pH (117 mV/pH) was achieved and it is attributed not only the to the relatively high buffering capacity of the Al_2O_3 layer atop the stack insulator; but also to the HfO_2 layer which enhances surface charge transduction.

4.6 Conclusions

In this chapter we explored the structure of ISFETs and examined its sensing mechanism. Experimental results were then presented which established that the ZnO NWFETs are excellent transducers of ionic charge. The subsequent chapter begins by charting the evolution of the structure of the ISFET to bioFET. As the sensing mechanism of ISFETs and bioFETs are the same, that is not covered in the next chapter. What follows, however, is a literature review of how the conditions in which biosensing experiments take place affects the output of a bioFET. In that regard the focus of the literature review is on the strength of the buffer and the distance from the gate of the biomolecule being sensed.

Chapter 5

Biosensing: An application of FET sensing

5.1 Introduction

ISFETs are made using established semiconductor manufacturing processes capable of the low-cost mass production of highly reliable, fast responding, low output impedance, miniaturised devices. On-chip integration with other electronic components such signal processing units is also a possibility given the shared manufacturing processes. These are a couple of the reasons why many have sought to integrate biologically active materials with the ISFET in an attempt to exploit the unique recognition and signal-amplification abilities of biological systems [20]. Such devices are classified as electrochemical biosensors by the International Union of Pure and Applied Chemistry (IUPAC). They are defined as an integrated receptor-transducer devices capable of providing specific quantitative or semi-quantitative analytical data using a biological recognition element that is in direct spatial contact with the transducing device [109].

Figure 5.1 depicts a model of an ISFET that has been modified with biological recognition elements (receptors). FET-sensors with this structure are commonly referred to as a bioFET. In this model the biological recognition layer (receptors) facilitates the specific binding of target biomolecules (analyte) to the surface of the FET [110].

A host of biologically sensitive materials of varying complexity can be used as recognition elements. These include biological molecular species such as enzymes, antibodies, antigens, proteins, and nucleic acids; or living biological systems (e.g., cells, plants, tissue slices, intact organs or whole organisms), which exploit biochemical mechanisms for recognition [92]. The type of recognition layer used depends on the analyte being detected, examples of which are shown in the schematics in Figure 5.2.

Upon binding with the receptor, the analyte causes a variation in the electric field at the electrolyte-oxide interface. This alters the concentration of charge carriers in the channel region of the device,

leading to a change in source–drain conductivity. Changes to the conductance of a bioFET caused by analyte can be recorded in a number of ways as depicted in Figure 5.3.

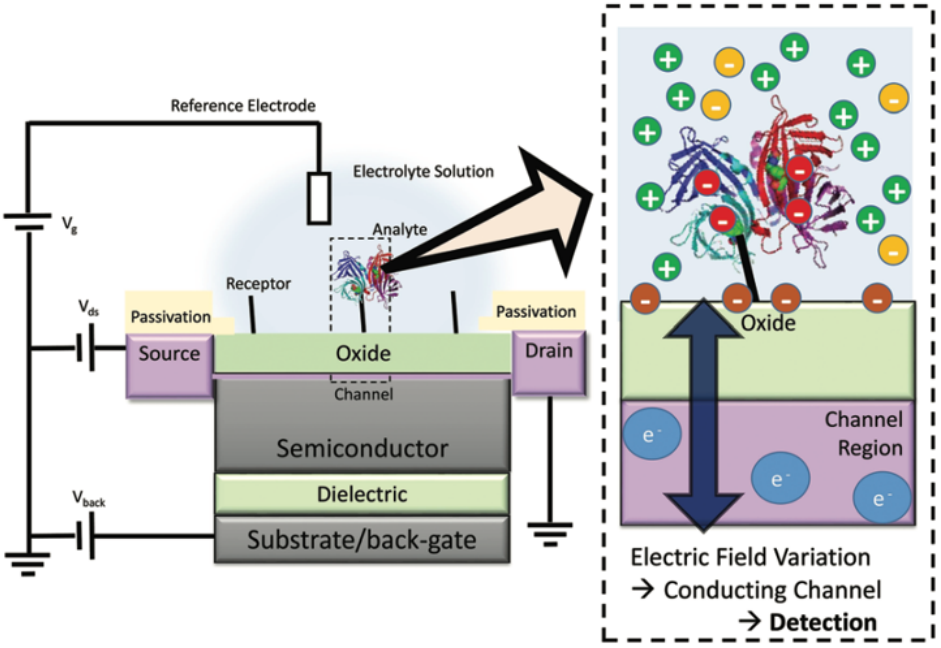

Figure 5.1: Schematic diagram of a FET biosensor. The binding of analyte to the receptor causes in a change in the electric field at the interface. This results in a change in the carrier concentration within the conducting channel. Consequently a measurable change in current is induced between the source and the drain.[68]

5.2 Effects of Buffer on Outputs

The analyte is delivered to the surface of the bioFET in an aqueous liquid commonly referred to as a buffer solution. Buffer solutions are comprised of a variety of ions for the primary purpose of maintaining the pH of the solution. The buffering capacity of a buffer is an important measure which quantifies its ability to maintain a constant pH, where pH is defined as the negative logarithm of the hydrogen ion concentration [68] :

$$pH = -\log[H^+] \tag{5.1}$$

and buffering capacity, β (mol), is given as:

$$\beta = \frac{dC_b}{d(pH)} = -\frac{dC_a}{d(pH)} \tag{5.2}$$

Where C_a and C_b are the concentrations (mol) of added acid and base. Phosphate Buffered Saline (PBS) is the most commonly used buffer in biosensing experiments and, in its standard form, is comprised of 10 mM NaPi, 138 mM NaCl, 2.7 mM KCl [116]. NaPi is combination of monobasic

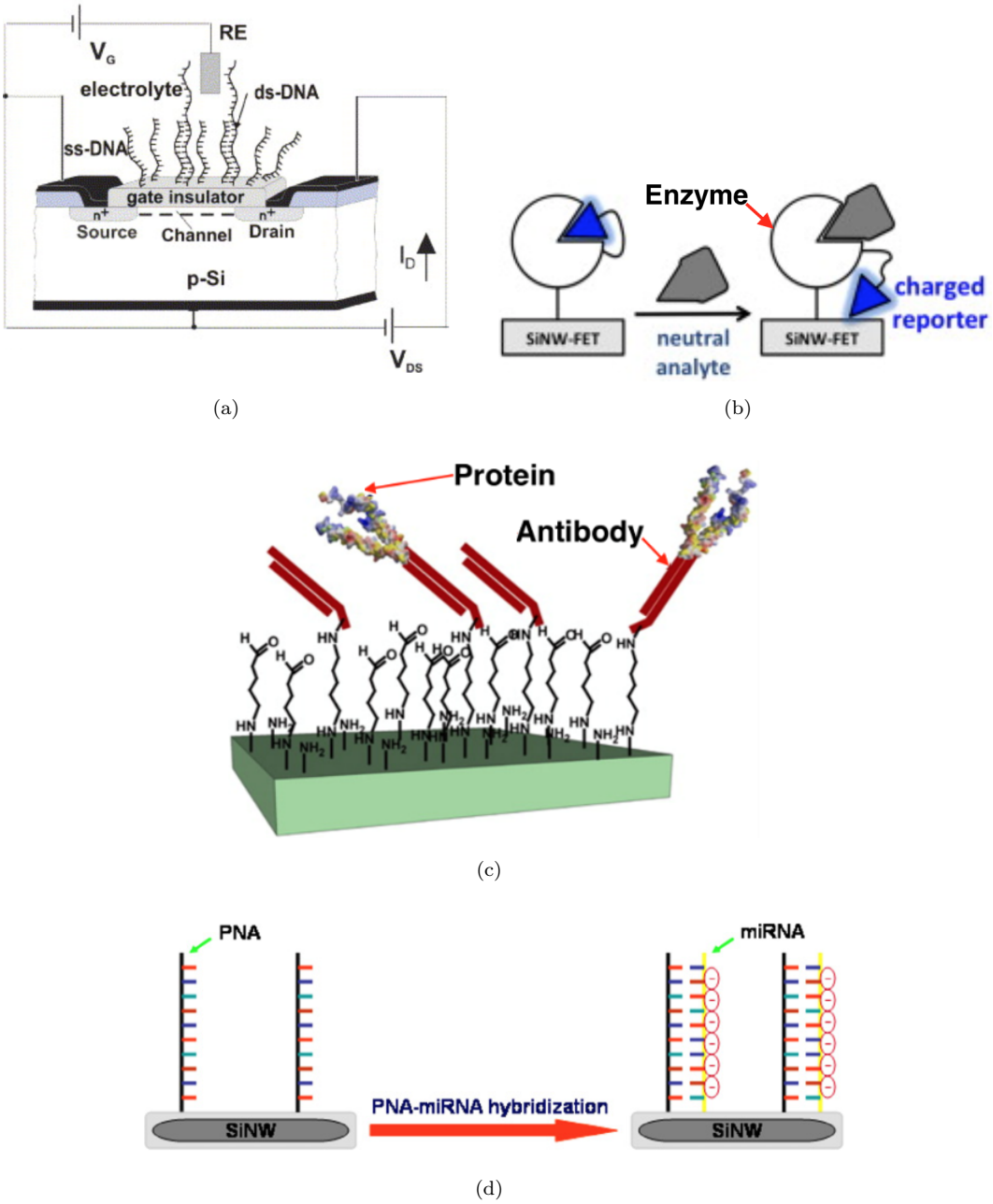

(a) (b)

(c)

(d)

Figure 5.2: (a)Probe DNA - DNA [111] (b) Antibody - Protein [112] (c) Enzyme - Substrate [113] (d) Probe PNA - miRNA [114]

(NaH_2PO_4) and dibasic (Na_2HPO_4) phosphates in varying ratios depending on the desired pH. The 10 mM NaPi buffer used in biosensing experiments has pH 7.4 (8.1 mM of Na_2HPO_4 and 1.9 mM NaH_2PO_4) is, by convention, defined as 1×NaPi [116]. The dilution notation (×) is used to signify the ionic strength of a phosphate buffer solution relative to this standard.

Dilution is often used by experimentalists to minimise the effects ions can have on the sensor's response as was seen in the 59 mV shift in threshold voltage per 10-fold increase in KCl concentration reported by Tarasov et al. This large shift in threshold voltage was attributed to the pH independent selective

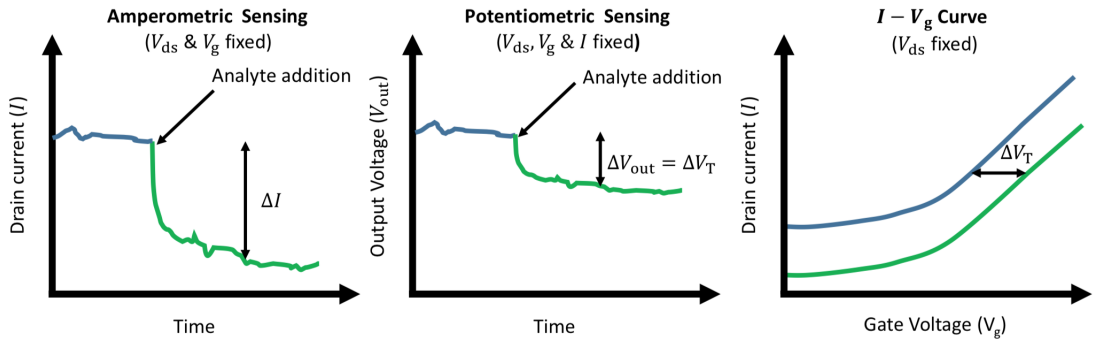

Figure 5.3: These graphs show the different methods of measuring a bioFETs response to presence of analyte. The blue line represents its response before analyte addition, and the green line after analyte addition. The change in surface potential upon analyte binding induces a change in drain current which can be measured by amperometric sensing or potentiometric sensing. The drain current can also be measured as a function of gate voltage (IV_g curve) both before and after analyte addition, resulting in two parallel curves from which the shift in gate voltage can be extracted. [115]

adsorption of anions[117]. Maekawa et al observed similar behavior in an ISFET, experimentally and in a molecular dynamics simulation, when the NaCl concentration in the buffer was increased [118].

5.3 Overcoming short debeye lengths caused by high ionic strength solutions

Dilution is also used as a means to increase the Debye length of the buffer. As mentioned above, the analyte delivered to the surface of BioFET is delivered in an ionic solution [80]. In these solutions, biomolecules such as proteins and DNA are surrounded by counterions in solution. For negatively charged DNA strands, the counterions would be positively charged ions in the electrolyte. These counterions are said to screen out the electric field of the biomolecules they surround such that, the electrostatic potential of the charge on the biomolecule decays exponentially towards zero with distance. The Debye length, a term used to refer to this characteristic length is given by Equation 5.3 where, for aqueous solutions at room temperature, l_B is the Bjerrum length ($0.7\ nm$) , $\sum_i$ is the sum over all ions in the solution , and ρ_i (cm^{-3}) and z_i are the density and valence, respectively, of the ions in solution [119].

$$\lambda_D = \frac{1}{\sqrt{4\pi l_B \sum_i \rho_i z_i^2}} \tag{5.3}$$

As seen in Table 5.1, the Debye length decreases as the ionic strength of a solution increases. As the ionic concentration of a solution increases the electrostatic potential of the charge the analyte decays exponentially towards zero in increasingly smaller distances. Figure 5.4 illustrates the difficulties in detecting analyte which arise from increasing ionic concentrations. With a decreasing Debye length, less and less of the electrostatic potential of the analyte contributes to the surface potential at the

electrolyte oxide interface. This ultimately results in smaller shifts in the FET's current due the presence of the analyte. In other words, the difference between the currents produced in response to the analyte in the buffer decreases as the Debye length decreases, respectively. This makes it increasingly difficult to detect the presence of the analyte as shown in Figure 5.5.

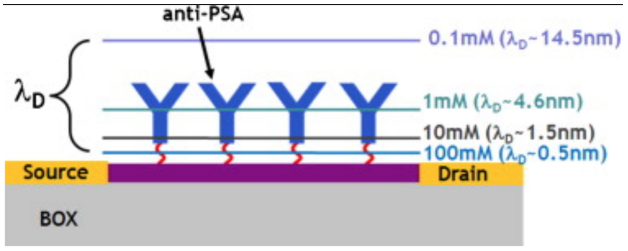

Figure 5.4: Schematic showing how the Debye screening length from the channel surface varies with the concentration of the buffer solution. [120]

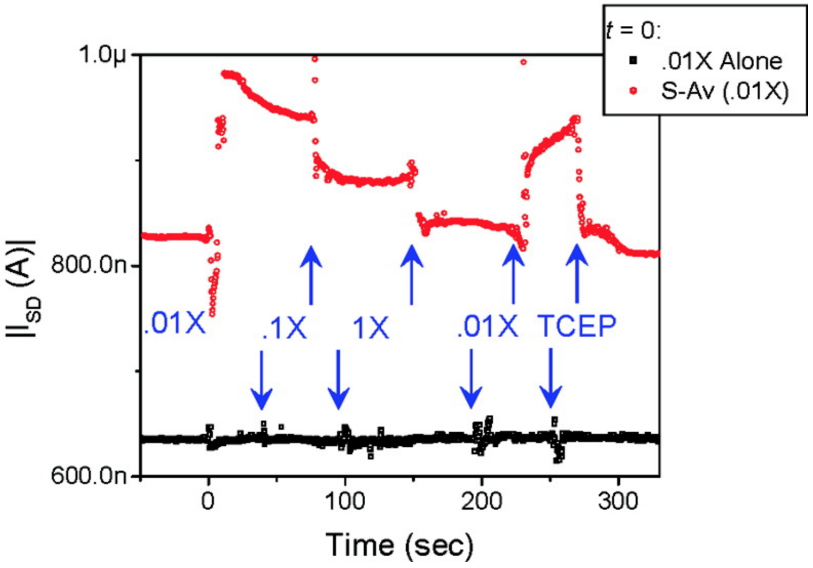

Figure 5.5: This graph shows how bioFET's response varies with changes to buffer ionic concentrations with (red) and without (black) streptavidin addition at time = 0. The blue text gives the PBS buffer concentration [Tris(2-carboxyethyl)phosphine hydrochloride, TCEP, was added in 0.01× PBS] and the blue arrows represent the onset of solution exchange [119]

Table 5.1: A table of the calculated Debye Screening Lengths for varying concentrations of PBS[112]

PBS pH 7.4	λ(nm)	Ionic strength (mM)
×1	0.7	150
×0.1	2.3	15
×0.05	3.3	75
×0.01	7.3	1.5
×0.001	23.2	0.15
×0.0001	75	0.015

5.4 Aiding detection: Flushing away high ionic solutions

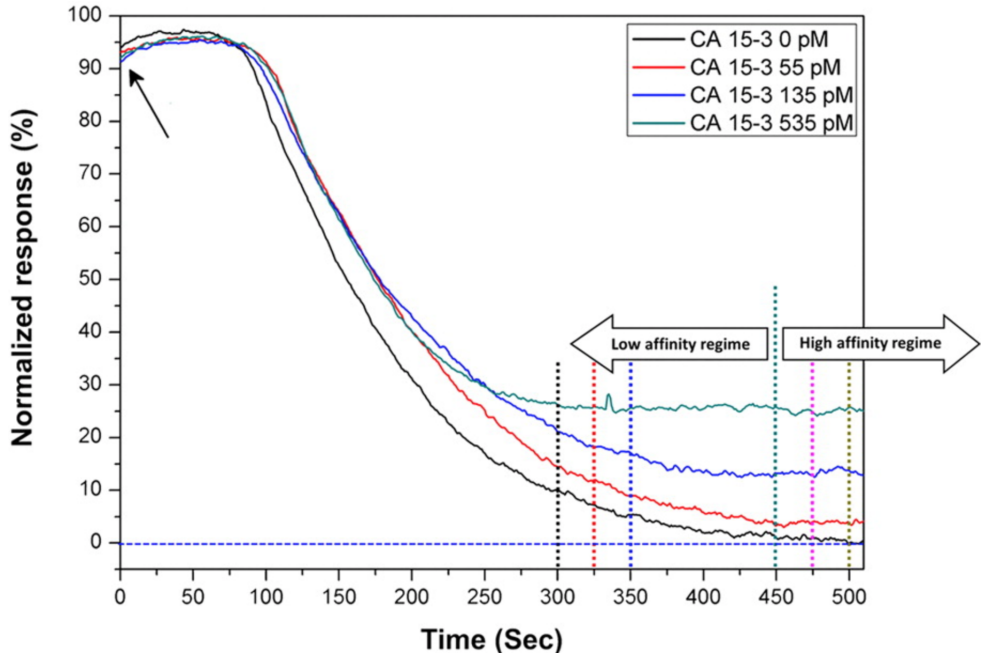

Figure 5.6: The black, red, blue and turquoise curves show the normalized electrical response of the anti-CA 153-modified Si nanowires in unprocessed bovineserum sample at CA 153 concentrations of 0 (control antigen-free sample), 55, 135, and 535 pM. The black arrow shows the time of solution exchange from the unprocessed serum samples to the low-ionic strength sensing buffer. [121]

The issue of short Debye lengths in high ionic fluids is not a trivial matter as the ionic strength of most physiological samples is $\geq$ 100 mM. In a bid to avoid using elaborate, lengthy steps such as centrifugation, filtering, preconcentration, and desalting to reduce the ionic strength of the sample; Krivistsky et al [121] suggested flushing the surface of a bioFET, in a controlled manner, with a low ionic strength buffer to induce the expedited removal of low-affinity, loosely bound molecules at the surface of a bioFET.

This flushing step, they theorised, would have the effect of reducing the charge screening effects of the irrelevant molecules resulting in the increased ability to detect the presence of the molecules of interest which have a high affinity with the receptors on the sensor's surface.

In the experiment carried out, the mouse monoclonal anti-human cancer antigen 15-3 IgG (Anti-CA 15-3) was used as it is known to have a strong binding affinity (low dissociation constant) with its antigen CA 15-3 antigen. Taking advantage of this low dissociation constant, Krivistsky et al demonstrated that simultaneously replacing the high ionic fluid surrounding the bound analyte, and washing non-specifically bound molecules with a low ionic solution, made it possible to detect the analyte without using the biosample manipulation steps listed above to increase the Debye length.

Furthermore, using this method they showed that it was possible to discern the concentration of the analyte in the sample Figure 5.6 in what was a novel demonstration of the real-time, direct label-free

sensing of biomarkers from untreated blood samples, using bioFETs. It should be noted however, that using a diluted buffer solution can introduce a variety of issues. The reduced the buffering capacity of the solution can make the system highly sensitive to small pH changes, introducing a potential source of noise to the measurement. Upon the addition of 1 μM Streptavidin to 0.01×PBS Lloret et al. observed 0.5 pH change in the pH of the buffer. However, there was a negligible change in the pH of the 1×PBS buffer which was attributed to its larger buffering capacity [116]. A 0.5 pH change, it has been noted, corresponds a non-specific 15 mV threshold voltage shift for FET with a SiO_2 surface wetted with a 0.01×PBS solution. This is hugely significant as a 15 mV threshold voltage shift is of the same order of magnitude as most measured Streptavidin signals. [68]

5.5 Conclusions

In this chapter we charted the evolution of the structure of the ISFET to bioFET. This was followed by a literature review of how the output of a bioFET can vary depending on the strength of the buffer and the distance from the gate of the biomolecule being sensed. The subsequent chapter explores how the stack passivation layer enables the ZnO NWFETs to produce a stable current for an hour in conditions that cause the function of the NWFETs to deteriorate quickly. This property- the ability to minimise the threshold voltage drift of the NWFET array when it is operating aqueous solutions of high salt concentrations, is critical to the device's function as a FET biosensor. In the next chapter the results of experiments conducted are used to demonstrate how the stack passivation layer aides in minimising threshold voltage drift. The benefits of this property are also discussed.

Chapter 6

Electrical Drift Characterisation of ZnO FET Sensors

6.1 Introduction

The duration of binding events between analyte and the receptors on the surface of a FET biosensor (bioFET) can last anywhere from a few seconds to thousands of seconds. The length of time depends on a number factors including the ionic strength of the surrounding solution; the concentration of analyte in solution; the binding affinity of the analyte to the receptors at the surface; and the mechanism by which the analyte is delivered to the surface of the bioFET [122]. For Point-of-Care (PoC) systems to be use at crash sites; at a patient's bedside; during physician-patient consultations, it is imperative that bioFETs can operate stably in solution for ≤ 1000 seconds in order to register the output signal change associated with analyte binding to the receptors.

When bioFETs come into contact with an aqueous solution during the course of a biosensing experiment, they experience a monotonic, temporal and relatively slow change in threshold voltage commonly referred to as drift. This change in threshold voltage is not caused by the analyte or by variations in the electrolyte composition but, in large part, by the hydration of the gate insulator layer between the electrolyte and the bioFET's channel [123]. During hydration, bonds are formed between OH groups in water and the metal/metalloid atoms in the gate insulator [124] such as SiO_2, Si_3N_4, Al_2O_3 and Ta_2O_5, with the reaction being facilitated by the presence of traps and buried surface sites in the insulator. Jamasb et al [125] modelled the growth of a thin, hydrated layer at the surface of the insulator limited by the dispersive transport of water molecules; and showed, theoretically and by experimentation, that the temporal growth of this hydrated layer reduces the effective capacitance of the gate insulator. This reduction occurs because the hydrated section of the insulator layer has a smaller dielectric constant than the underlying, unmodified, insulator layer which also decreases in thickness as, over time, the hydrated layer grows. Consequently, the effective capacitance of the insulator, calculated as the capacitance of the hydrated layer in series with the thinner underlying, unmodified, insulator layer decreases as the hydrated layer grows.

Typically, for n-channel bioFETs a decreasing insulator capacitance would lead to a positive voltage drift. That is to say, over time, the threshold voltage would increase leading to a decrease in the output drain current. Not only does a decreasing output drain current, resulting from threshold voltage drift, dampen any change in current associated with an analyte-receptor binding event; it makes it difficult to distinguish between the signal generated by the binding event and the background noise generated by the electrolyte and the bioFET itself. Due to the variance in the duration of binding events (i.e. a few seconds to thousands of seconds) between analyte and receptors, it is of critical importance that the magnitude of threshold voltage drift is kept to a minimum so as to minimise the negative effects of a diminishing drain current on the function of bioFETs.

Mitigating the effects of threshold voltage drift by the Rapid Thermal Annealing (RTA) of the insulator layer, which reduces the density of hydration facilitating defects such as buried surface sites and traps, has been shown to be quite effective [126] [127]. However, RTA is not a viable option when employing a low temperature fabrication process of $\leq 200^{o}C$ [128]. Presented in this chapter is a low temperature approach to mitigating threshold voltage drift which is centered around depositing a multi-material stack of high-κ dielectric insulators via Plasma Enhanced Atomic Layer Deposition (PEALD). As opposed to the current bioFET design and fabrication standard, which is to deposit a single material high-κ dielectric insulator layer, a stack of appropriately chosen high-κ dielectric insulators will have a larger effective capacitance making it a more potent transducer [76]. More importantly, the effects of hydration are less pronounced on the stack than the single material insulator layer. This is because the change in the effective capacitance, resulting from of the presence of the hydrated layer, is smaller for the stack than for the single material insulator layer where, the effective capacitance is calculated as the capacitance of the hydrated layer in series with the underlying, unmodified, insulator layers. As a result, the bioFET with a stack insulator will experience a smaller threshold voltage drift and drain current shift than the bioFET with a single material insulator layer.

The fabrication process begun with growing 100 nm of Silicon Dioxide (SiO_2) by dry oxidation on CZ(100) silicon wafers at 1000 ^{o}C. A 90 nm layer of Aluminium Zinc Oxide (AZO - 5 % Al, 95 % ZNO) was then deposited, by Plasma Enhanced Atomic Layer Deposition (PEALD). This AZO layer was wet etched to form individual bottom gate electrodes for each NWFET array. Wet etching was done in a beaker of Hydrochloric(HCl) acid mixed with Deionized water in a ratio of 1:1000 (HCl : H_2O). Subsequently, 50 nm of Al_2O_3 was deposited by PEALD and etched by Argon Ion Beam Etch (IBE) to form the bottom gate oxide. Using PEALD, a stack insulator layer consisting of 4 nm of HfO_2 between two 8 nm Al_2O_3 layers was deposited on one device. 24 nm of Al_2O_3 was deposited on the other device to be used as a control device. For all Al_2O_3 depositions the substrate was heated to 150^{o}C and 200^{o}C for HfO_2 deposition.

6.2 Experiment

The FET biosensors used in the experiments described below were comprised solely of 512 ZnO Nanowire Field Effect Transistors (NWFETs) arrays Figure 6.1. ZnO is an ideal material because

it is naturally a n-type semiconductor [15] thus eliminating the need for a high temperature doping process step. ZnO also has a large and direct band-gap (3.37 eV [16]) which enables it to sustain large electric fields; withstand higher breakdown voltages; generate lower levels of noise; and operate at high temperatures and levels of power [17].

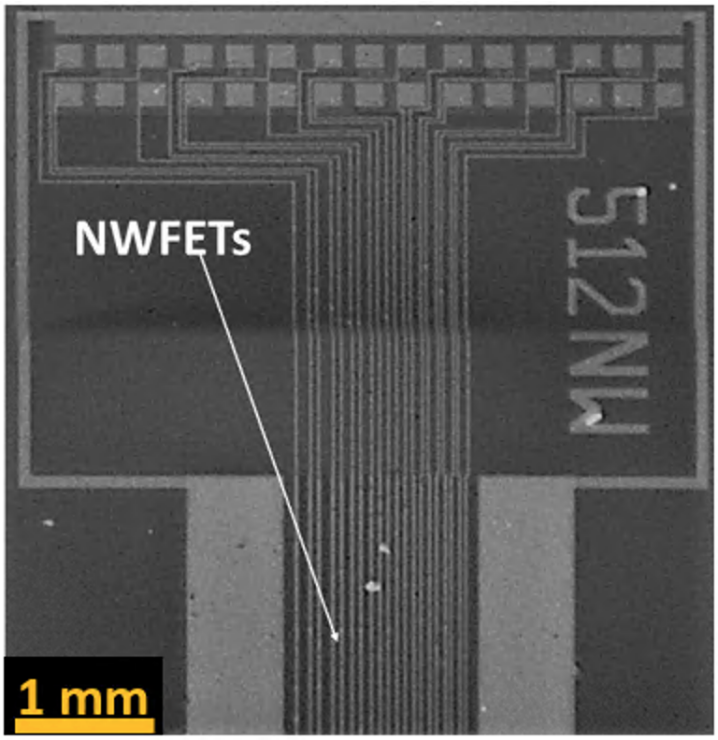

Figure 6.1: (a) An optical image of a chip consisting of 512 ZnO NWFET arrays with gate lengths of 20 μm, 30 μm, 40 μm, 60 μm and 90 μm. One of these chips was used for each of the reported experiments with the NWFET array with the 20 μm gate being probed in each instance.

To investigate whether ZnO NWFETs with a stack insulator layer have a lower hydration related threshold voltage drift than ZnO NWFETs with a single material (Al_2O_3) insulator layer, two set of ZnO NWFET arrays were fabricated. One set of ZnO NWFET arrays had a 24 nm thick Al_2O_3 passivation layer. On the other ZnO NWFET array a dielectric stack comprised of a 4nm layer of HfO_2 sandwiched between two 8nm layers of Al_2O_3 (AHA) was deposited. The reason for using Al_2O_3 as the single material insulator layer, and adopting the sandwich configuration for the stack insulator layer, was to minimise the amount of HfO_2 used. HfO_2 has a much larger dielectric constant than Al_2O_3 [75] however, it does suffer from hysteresis phenomenon [77]. Al_2O_3 has demonstrated e a stronger resistance to these non-ideal effects [78] than HfO_2.

Phosphate Buffered Solution (PBS) (10 mM phosphate, 150 mM KCl, pH 7.4) was delivered to surface of each device through laser cut PMMA microfluidic channels Figure 6.2(a). This PMMA microfluidic channel design was an early prototype which was abandon for a simpler design Figure 3.5 which made it easier to pipette solutions on the surface of the NWFETs. The ionic strength of the PBS used in this experiment was made up to 150 mM (Debye length of 0.7 nm) because the ionic strength of most physiological samples is $\geq$ 100 mM [112], [129], [130]. I_DV_G sweeps were recorded before and after

both devices were wetted with PBS, in dry conditions. In the subsequent hour, while each device was wetted with PBS, the drain current was recorded. For this current-time wet measurement, both devices were biased in the subthreshold region with a gate voltage of 4 V and a drain voltage of 2 V. The devices were biased in the subthreshold region as it has been shown to be the most sensitive region of bioFET operation for concentration related sensing [99]. That is to say, bioFETs are most sensitive to changes in analyte concentration when operating in this region; and as these are the kinds of future sensing experiments we aim to be conducting, biasing in the subthreshold region was deemed to be expedient. Moreover it enables the NWFETs to be employed as low power devices. All electrical measurements were conducted in a dark environment, at room temperature, using the Keysight Semiconductor Parameter Analyzer (B1500A).

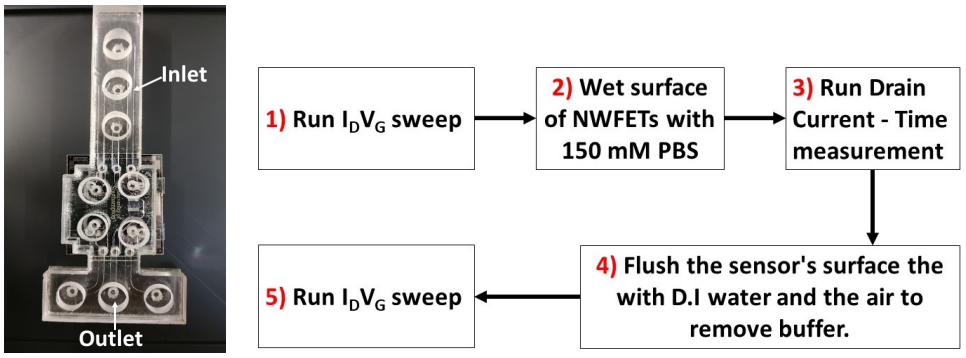

(a) (b)

Figure 6.2: (a) An image of ZnO NWFETs underneath a sheet of PMMA laser cut to form channels through which to flow PBS from a syringe to wet the surface of the NWFETs. The width of the channels is 1.18 mm. (b) The protocol for the experiment investigating the threshold voltage drift mitigating effects of the stack insulator layer. Both the ZnO NWFETs with the stack insulator layer and the ZnO NWFETs with the Al_2O_3 insulator layer undergo this protocol.

6.3 Results and Discussion

Figure 6.3 shows I_DV_G curves for both devices in dry conditions. As mentioned above, the bias voltages chosen for both devices were a gate voltage of 4 V and a drain voltage of 2 V. The data generated from the I_DV_G sweeps in Figure 6.3 showed that these bias voltages produced a 1.40 nA current for the ZnO NWFETs with the stack insulator and 2.79 nA current for ZnO NWFETs with the Al_2O_3 insulator. Figure 6.4 depicts how the drain current of each device varies over an hour when wetted with PBS. In comparing the drain current before and an hour after PBS was initially delivered to the surfaces of both devices, it was seen that the drain current of the ZnO NWFETs with the Al_2O_3 insulator had shifted by 2.72 nA to a value of 73.8 pA (left axis of Figure 6.4) by the end of the experiment. This 97.4% change in current corresponds approximately to a 0.5 V threshold voltage shift.

Although the drain current of this device exhibited some stability over the course of the experiment (i.e. drain current varied by, roughly, 2 pA during the experiment), the magnitude of the drain current of this device was in the range of the leakage current. Hydration causing a bioFET to drift into the range of leakage current is detrimental to its function as biosensor, as negatively charged analyte such as DNA would have the effect on n-channel bioFETs of decreasing the drain current. Consequently, any change in current associated with an analyte-receptor binding event will be virtually indistinguishable from the leakage current, thus rendering such a bioFET effectively useless.

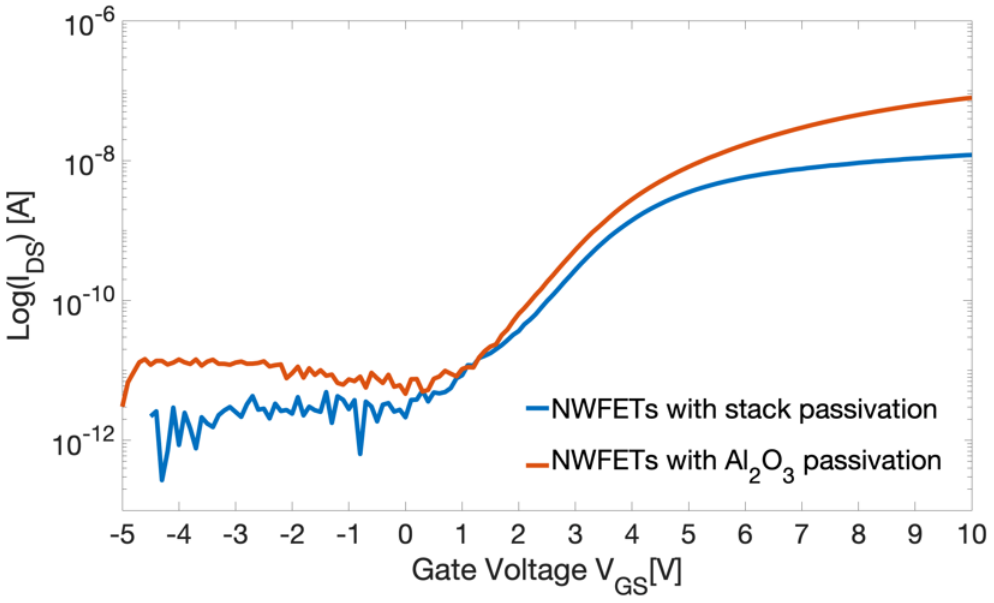

Figure 6.3: (a) I_DV_G curves of the ZnO NWFETs with the stack insulator layer and the ZnO NWFETs with the Al_2O_3 insulator layer before being wetted with PBS. The drain voltage for both devices during this I_DV_G sweep was 2 V.

The ZnO NWFETs with the stack insulator layer, in stark contrast, produced a significantly smaller change in drain current of 0.064 nA. This corresponded to a a 4% change in current, which is equivalent to a 0.2 V threshold voltage shift over the course of the hour long investigation. During this period the drain current of this device showed quite remarkable stability as it only varied by 0.04 nA. Furthermore, the output current was 2 orders of magnitude above the leakage current range, thus eliminating any potential difficulties in differentiating between the leakage current and the output signal generated in response to an analyte-receptor binding event at the surface of NWFETs.

Table 6.1 summarises the results obtained which support the assertions made above. It was posited that while the insulator layers of both devices would be subject to hydration as a result of being wetted with an electrolyte; the reduction in effective capacitance of the stack insulator layer would be less than reduction in the capacitance of the single material Al_2O_3 insulator layer. Consequently, the ZnO NWFETs with the stack layer would experience a smaller drift in threshold voltage and drain current than the ZnO NWFETs with the Al_2O_3 layer. The experimental results demonstrated that the NWFETs with the stack insulator has a smaller shift in threshold voltage than the NWFETs with the Al_2O_3 insulator. Furthermore, the NWFETs with the Al_2O_3 insulator exhibit a relatively larger response to the electrolyte with a 97.4% change in drain current compared to a 4% change

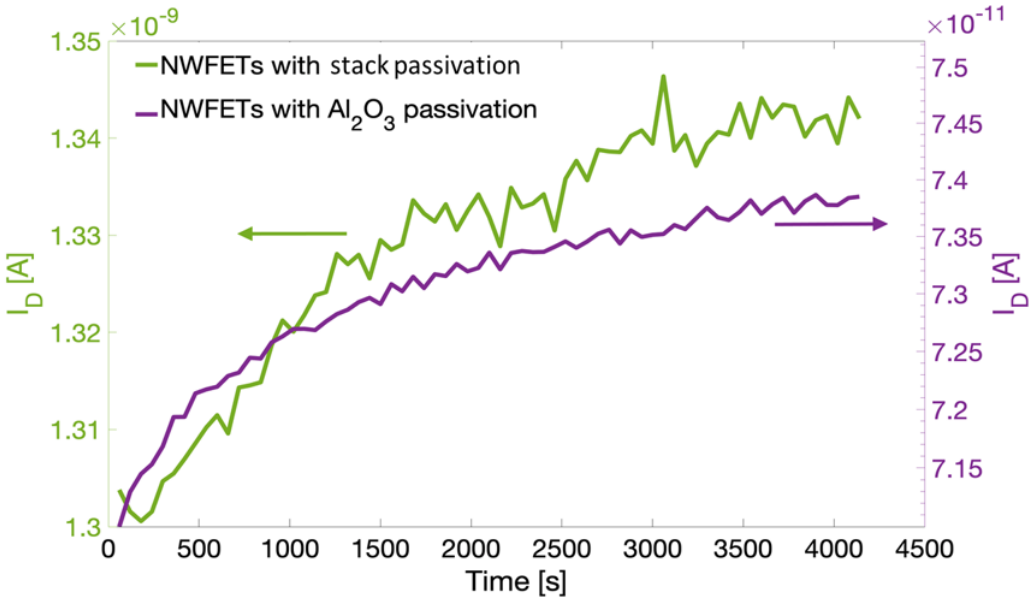

Figure 6.4: (b) Drain Current against Time graph for NWFETs while wetted with PBS. Both devices were biased with in the subthreshold region with a gate voltage of 4 V and a drain voltage of 2 V.

produced by the NWFETs with the stack insulator. A 97.4% change in drain current constitutes significant background noise which would mask the response generated by analyte given that during the experiment the drain current of this device was in the range of the leakage current. The results obtained confirm that the stack layer enhances the resilience of ZnO NWFETs biosensors, operating in electrolytes of physiological relevant ionic concentrations, by minimising the drift in threshold voltage and drain current. Given that the NWFETs with the stack insulator performed better in this environment than the NWFETs with the Al_2O_3 insulator, only the NWFETs with the stack insulator were used in future experiments.

Table 6.1: A summary of the experimental results obtained.

Devices	Magnitude of shift in drain current (nA)	Percentage change in in drain current (%)	Magnitude of shift in threshold voltage (mV)
Stack	0.064	4	200
Al_2O_3	2.72	97.4	500

6.4 Conclusions

BioFETs operating in an electrolyte experience a monotonic, temporal and relatively slow drift in threshold voltage caused by the hydration of the insulator layer between the electrolyte and the bioFET's channel. It is imperative to the function of bioFETs that drift inducing effects of hydration are minimised as it results in a diminishing drain current; making it increasingly difficult to distinguish between the signal generated in response the analyte - receptor binding event and the background noise generated by the electrolyte and the bioFET itself. It has been shown that a tri-layer insulator

stack of high-κ dielectrics compromised of HfO_2 sandwiched between two Al_2O_3 layers experiences drift to lesser degree than a single material insulator layer which is comprised of Al_2O_3. This is because the stack insulator experiences a smaller, hydration related, change in effective capacitance than the single material Al_2O_3 insulator layer.

Having established that the stack passivation layer enables the NWFETs to produce a stable current output, the next chapter focuses squarely on miRNA detection. It begins with a literature review highlighting the importance of the miRNA group of biomolecules. Subsequently the results of miRNA detection experiments are presented and discussed. It should be noted that Chapter 6 was published as a paper in Micro and Nano Engineering (MNE) journal.

Chapter 7

Detection of miRNA

7.1 Introduction

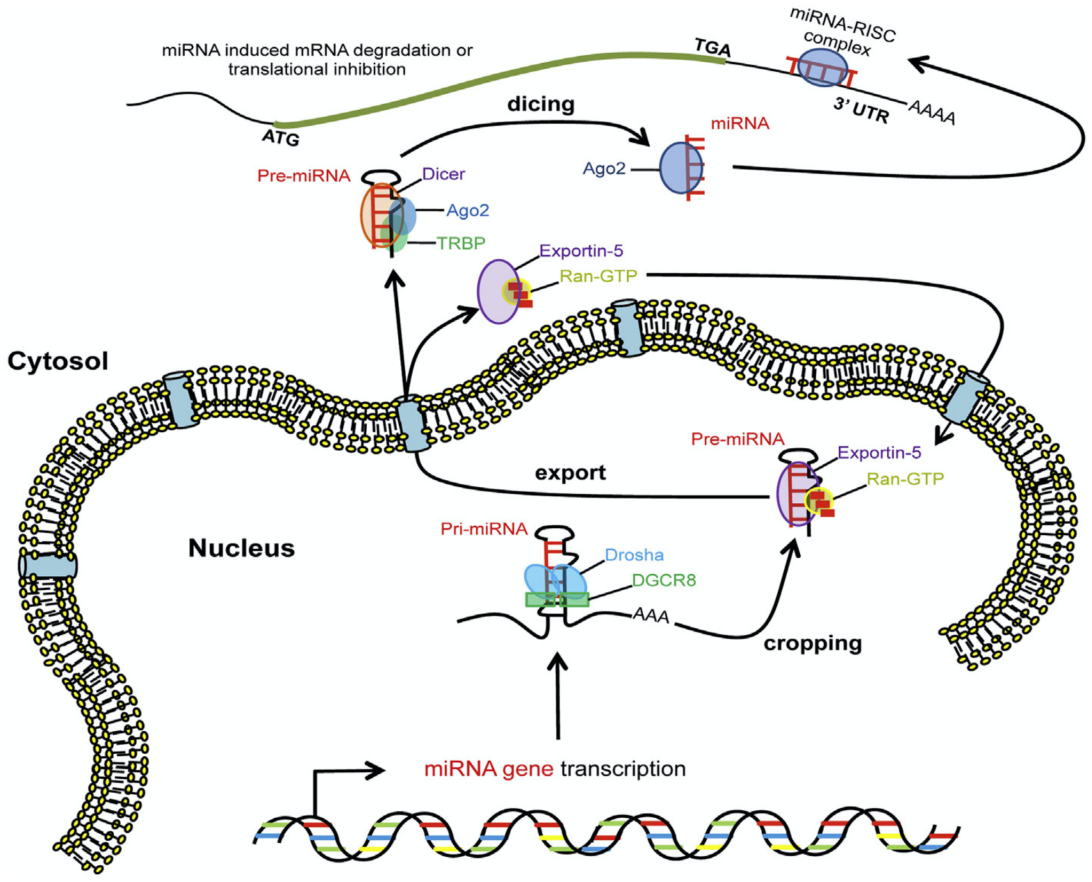

Figure 7.1: A schematic of miRNA biogenesis [131]. miRNA is the analyte used in the experiments detailed in this chapter.

Cancer is a complex disease characterised by genes which encode oncogenic and tumour-suppressor proteins. microRNAs (miRNA), a group of small non-coding RNA that regulate gene expression,

have been shown to participate in a number of essential biological process including cell proliferation control, hematopoietic B-cell lineage fate, B-cell survival, brain patterning, pancreatic cell insulin secretion and adipocyte development [1].

Figure 7.1 shows that miRNA are located in the cell nucleus where they are transcribed by RNA polymerase II. This process starts with the production of a long primary transcript referred to as pri-miRNA [132]. The Drosha enzyme generates miRNA precursors called pre-miRNA by cropping pri-miRNA [133]. When bound to pre-miRNAs, Exportin 5 protein and the Ran-GTP enzyme facilitate the export of pre-miRNAs from the nucleus to the cytoplasm [134]. In the cytoplasm pre-miRNA are cleaved by RNAse III Dicer producing a mature miRNA duplex of about 22 nucleotides [131]. The miRNA duplex binds to the RNA-induced silencing complex (RISC) which retains the mature strand fragment but discards the complementary strand which is eventually degraded [135] [136]. The resulting fully functioning miRNA induces the degradation of their mRNA target when matched with the complementary 3 prime Untranslated Region (3'-UTR) region of their targets.

The abnormal expression of miRNA genes, which refers to the loss, amplification or mutations of miRNA has been identified in a wide variety of cancers including B-Cell Chronic Lymphocytic Leukemia (B-CLL) [2], breast carcinoma [3], primary glioblastoma [4], hepatocellular carcinoma [5], papillary thyroid carcinoma [6], lung cancer [7], colon carcinoma [8], and pancreatic tumours [9]. The abnormal expression of miRNA has been found in malignant cells and also in premalignant cells such as, benign tumours in colons where miR-143 and miR-145 expression was reduced [8]; or in pituitary adenomas where miR-16-1 and miR-15a expression was reduced [137]. miR-221 has also been seen to be over expressed in normal thyroid tissue next to tumours but not in the normal thyroid tissue of individuals without tumors [6]. Therefore, it is likely that in a number of cases cancer-specific miRNA fingerprints could indicate the initiation of the malignant process. Furthermore, it has been noted that miRNA, in certain cases, could be used as an indicator of post-operative survival rates with high miR-155 and low let-7a-2 expression correlating with poor survival rates [138]. It is for these reasons that monitoring the loss, amplification or mutation of miRNA is vital for the classification, diagnosis, and prognosis of human malignancies [139].

7.2 Experiment

7.2.1 Analyte Reagents Used for Sensing

The importance of monitoring miRNA motivated the design and execution of experiments detailed below. The aim of these experiments was to establish whether the output of the ZnO NWFETs would change in response to changes in miRNA concentration. Changes in concentrations mimic the loss and amplification of miRNA. Detecting mutations in miRNA was outside the scope of the investigation. The biosensors used in the experiment described below were comprised solely of 512 ZnO Nanowire Field Effect Transistors (NWFETs) arrays with a stack insulator layer as fabricated in Chapter 3.

Table 7.1: List of Analyte

EXPERIMENT	ANALYTE
E-I	miDNA21-P21 SHORT duplex (D21-Short)
E-II	miDNA21-P21 LONG duplex (D21-Long)
E-III	miRNA21-P21 SHORT probe duplex (R21-Short)

Table 7.2: Analyte sequences. The approximate length of an oligomer (nucleotide) is 0.676 nm [140].

OLIGOMER ID	SEQUENCE	LENGTH
miDNA21	TAG CTT ATC AGA CTG ATG TTG A	22 oligomers (15 nm)
P21 SHORT	TCA ACA TCA GTC TGA TAA GCT A	22 oligomers (15 nm)
P21 LONG	CCC CCC CCC CCC CCC CCC CCC CCC CCC CCC TCA ACA TCA GTC TGA TAA GCT A CCC CCC CCC CCC CCC CCC CCC CCC CCC (P21 SHORT extended by 30 C bases on each side)	82 oligomers (55 nm)
miRNA21	UAG CUU AUC AGA CUG AUG UUG A	22 oligomers (15 nm)

Table 7.3: Experiment protocol

	PROTOCOL
Phase 1	Aqueous Buffer CTM Dehydrated Buffer CTM
Phase 2	Aqueous 10 nM analyte in Buffer CTM Dehydrated 10 nM analyte in Buffer CTM
Phase 3	Aqueous 100 nM analyte in Buffer CTM Dehydrated 100 nM analyte in Buffer CTM
Phase 4	Aqueous 1 μM analyte in Buffer CTM Dehydrated 1 μM analyte in Buffer CTM

In all investigations, Trizma-Ethylenediaminetetraacetic (EDTA) buffer was used. The Trizma-EDTA (TE) Buffer sample was comprised of 2 mM Trizma, 10 mM KCl, 200 μM EDTA. Trizma is a buffer molecule which aids in regulating the pH of the samples and the EDTA molecule inhibits the hydrolysis of DNA molecules by exogenous DNases enzymes [141]. The analyte used in each experiment is listed in Table 7.1. The sequence of each miDNA and miRNA molecule is given in Table 7.2.

miRNA-21 was chosen as the analyte for following reasons. The over-expression of miRNA-21 in ductal adenocarcinoma, has been reported to precede changes in the phenotype of the ducts, suggesting the possibility of using miRNA-21 as an early diagnosis biomarker to improve prognosis [142]. High levels of miRNA-21 expression have also been reported in breast [3], glioblastomas [4], pancreas [143] and colon cancer [144]. Furthermore, several miRNAs have been seen to indicate whether specific cancer treatments have been effective or not. The over-expression of miRNA-21 in particular has been observed as being sufficient to predict poor response to adjuvant chemotherapy in adenocarcinomas [144]. A similar finding has been reported for miRNA-21 in pancreatic cancer patients treated with gemcitabine [145]. Because of its utility as an early diagnosis biomarker and as a sufficient predictor the efficacy of cancer treatment, miRNA-21 was chosen as the analyte for these experiments. miDNA are the stable biological equivalent of miRNA. As it is known that miRNA degrades easily within cells, equivalent miDNA strands are often used to demonstrate the ability of a device to detect miRNA [146].

7.2.2 miDNA and miRNA Measurement Protocols

Each experiment follows the protocol detailed in Table 7.3. The first phase of each experiment involved measuring the drain current response of the NWFET array when its surface was wetted with the buffer sample. This measurement was carried out for ten minutes (600 s) during which the drain current was recorded every second. Subsequently, the buffer sample was dehydrated by placing the wetted NWFET array on a heated stage for 5 minutes at 30 °C. The drain current response of the NWFETs to the dehydrated buffer sample was then recorded for 600 s. Following this measurement the surface of the NWFET was rinsed with Deionized (DI) water.

The second phase began with measuring the drain current response of the NWFET array when its surface was wetted with the 10 nM of analyte in TE Buffer. In E-I the analyte was the miDNA21-P21 SHORT duplex; in E-II it was the miDNA21-P21 LONG duplex; and in E-III it was the miRNA21-P21 SHORT duplex. There are a number of examples of the use of extended probes complementary to miRNA, in nanopore pulse sensing experiments [147][148]. Extended probes have a higher charge and thus more susceptible to an electric field. Consequently the miRNA-probe duplex experiences a larger electrophoretic force drawing it towards the nanopore [148]. In E-II a long probe was used to observed whether, as analyte concentration was varied, the resulting change in drain current response would be larger than with the short probe duplex in E-I.

As in the previous phase, the analyte sample was dehydrated by placing the wetted NWFET array on a heated stage for 5 minutes at 30 °C. The drain current response of the NWFETs to the dehydrated 10 nM analyte sample was then recorded for 600 s. Subsequently the surface of the NWFET was then

rinsed with DI water. The same procedure was carried out in phases 3 and 4 for analyte concentrations of 100 nM and 1 μM samples. In the absence of the time-consuming functionalisation process, the reason for dehydrating the buffer and analyte samples was to ensure that the miDNA-21 and miRNA21 duplexes physisored to the surface of the stack insulator layer. All electrical measurements presented were conducted in a dark environment, at room temperature, using the Keysight Semiconductor Parameter Analyzer (B1500A). Different 512 ZnO NWFET arrays used in experiments E-I, E-II and E-III Figure 7.2.

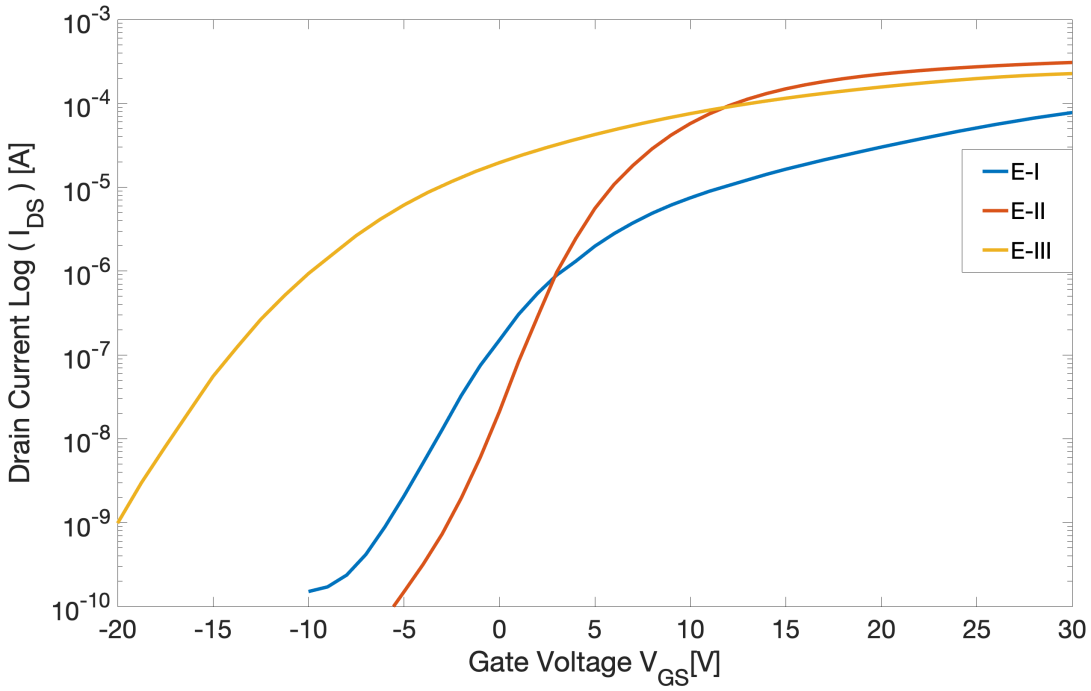

Figure 7.2: I_DV_G curve of the ZnO NWFET arrays used in each experiment. Each I_DV_G sweep was conducted in dry conditions.E-I = miDNA21-P21 Short Duplex; E-II = miDNA21-P21 Long Duplex; E-III = miRNA21-P21 Short Duplex. The bias point for the devices used in each experiment is presented as follows: (Experiment identifier, Gate Voltage, Drain Voltage, Drain Current). (E-I, 1 V, 5 V, 304 nA); (E-II, 2 V, 3 V, 286 nA); (E-III, -5 V, 1 V, 6.1363 uA).

7.3 Results

The results of experiment E-I are displayed in Figure 7.3. Figure 7.3(a) shows the drain current response of the NWFET array to aqueous buffer and aqueous miDNA21-SHORT duplex samples. For an expanded view please see Figure E.1. Figure 7.3(b) shows the drain current response to dehydrated buffer and dehydrated miDNA21-SHORT duplex samples. The results of experiment E-II are displayed in Figure 7.4. Figure 7.4(a) shows the drain current response of the NWFET array to aqueous buffer and aqueous miDNA21-Long duplex samples. Figure 7.4(b) shows the drain current response to dehydrated buffer and dehydrated miDNA21-Long duplex samples. The results of experiment E-III are displayed in Figure 7.5. Figure 7.5(a) shows the drain current response of the

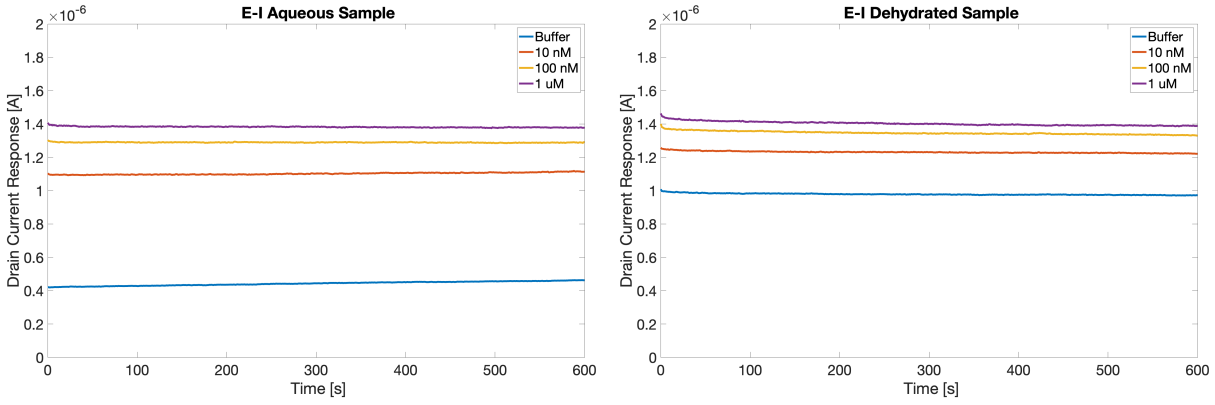

(a) (b)

Figure 7.3: The drain current response of the NWFETs to the buffer and analyte samples. The analyte in this instance was the miDNA21-P21 SHORT duplex (D21-Short) (a) These were results obtained when the NWFET array was wetted with each aqueous sample. (b) These were results obtained when the aqueous component of each sample was evaporated from the surface.

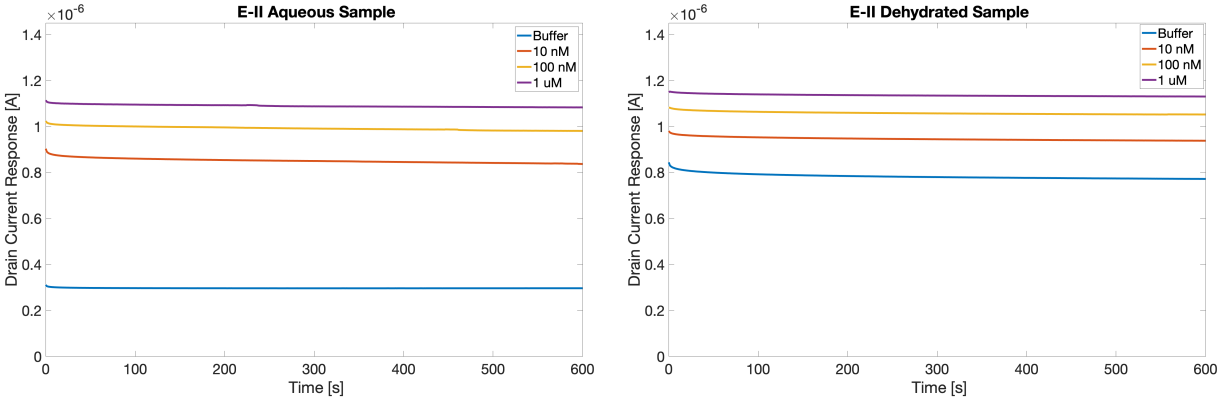

(a) (b)

Figure 7.4: The drain current response of the NWFETs to the buffer and analyte samples. The analyte in this instance was the miDNA21-P21 LONG duplex (D21-Long) (a) These were results obtained when the NWFET array was wetted with each aqueous sample. (b) These were results obtained when the aqueous component of each sample was evaporated from the surface.

NWFET array to aqueous buffer and aqueous miRNA21-SHORT duplex samples. Figure 7.5(b) shows the drain current response to dehydrated buffer and dehydrated miRNA21-SHORT duplex samples.

In all the graphs Figure 7.3, Figure 7.4 and Figure 7.5 it can be seen that as the analyte concentration was increased the Drain Current Response also increased. This trend was observed across all experiments and for both aqueous and dehydrated samples. There is a clear distinction between the signals produced at each analyte concentration. Consequently, changes in concentration in miDNA-21 and miRNA-21 can be detected.

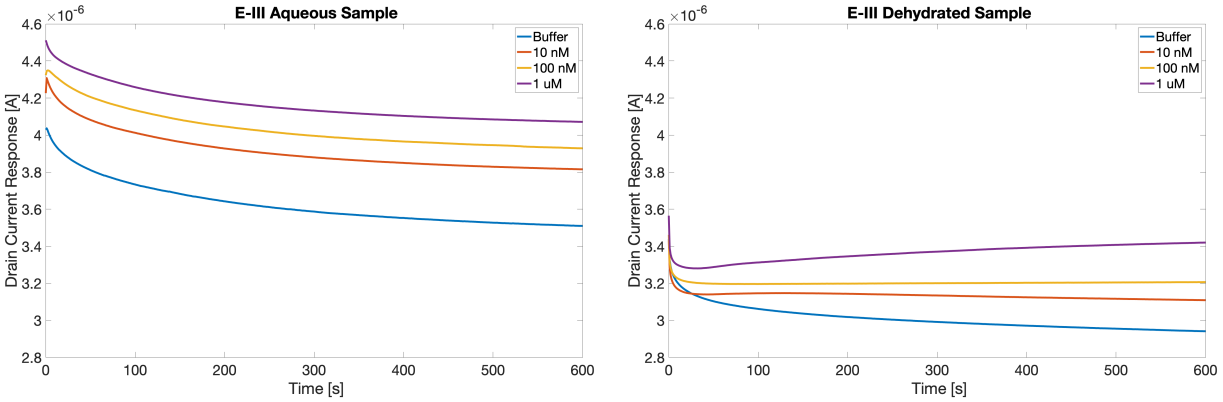

(a) (b)

Figure 7.5: The drain current response of the NWFETs to the buffer and analyte samples. The analyte in this instance was the miRNA21-P21 SHORT duplex (R21-Short) (a) These were results obtained when the NWFET array was wetted with each aqueous sample. (b) These were results obtained when the aqueous component of each sample was evaporated from the surface.

7.3.1 miDNA- Short VS Long Probe

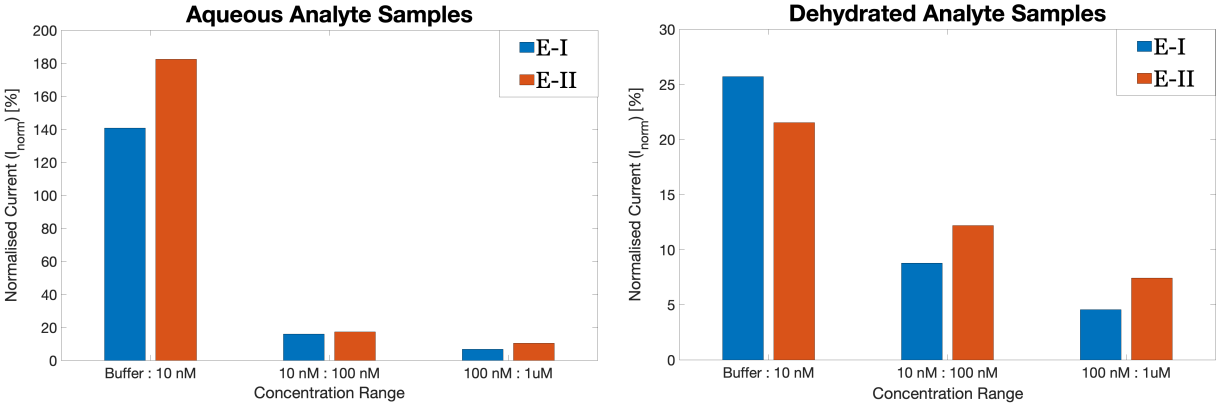

(a) (b)

Figure 7.6: Comparing changes in the normalised current as the analyte concentration is increased in 10-fold increments. (a) aqueous miDNA21-P21 SHORT duplexes (E-I) vs aqueous miDNA21-P21 LONG duplexes (E-II) (b) dehydrated miDNA21-P21 SHORT duplexes (E-I) vs dehydrated miDNA21-P21 LONG duplexes (E-II). The designation x:y on the x-axis refers to a 10-fold concentration of the analyte.

As mentioned above, this investigation was designed, in part, to observe whether the NWFETs would have a stronger response to long probe duplexes than short probe duplexes. On account of the long probe having more charge than the short probe, it was thought that the NWFETs would have a stronger response to the presence of the long probe duplexes than short probe duplexes. The normalised current I_{norm} (A) in Equation 7.1 is a measure of the change in current resulting from a ten-fold change in analyte [68].

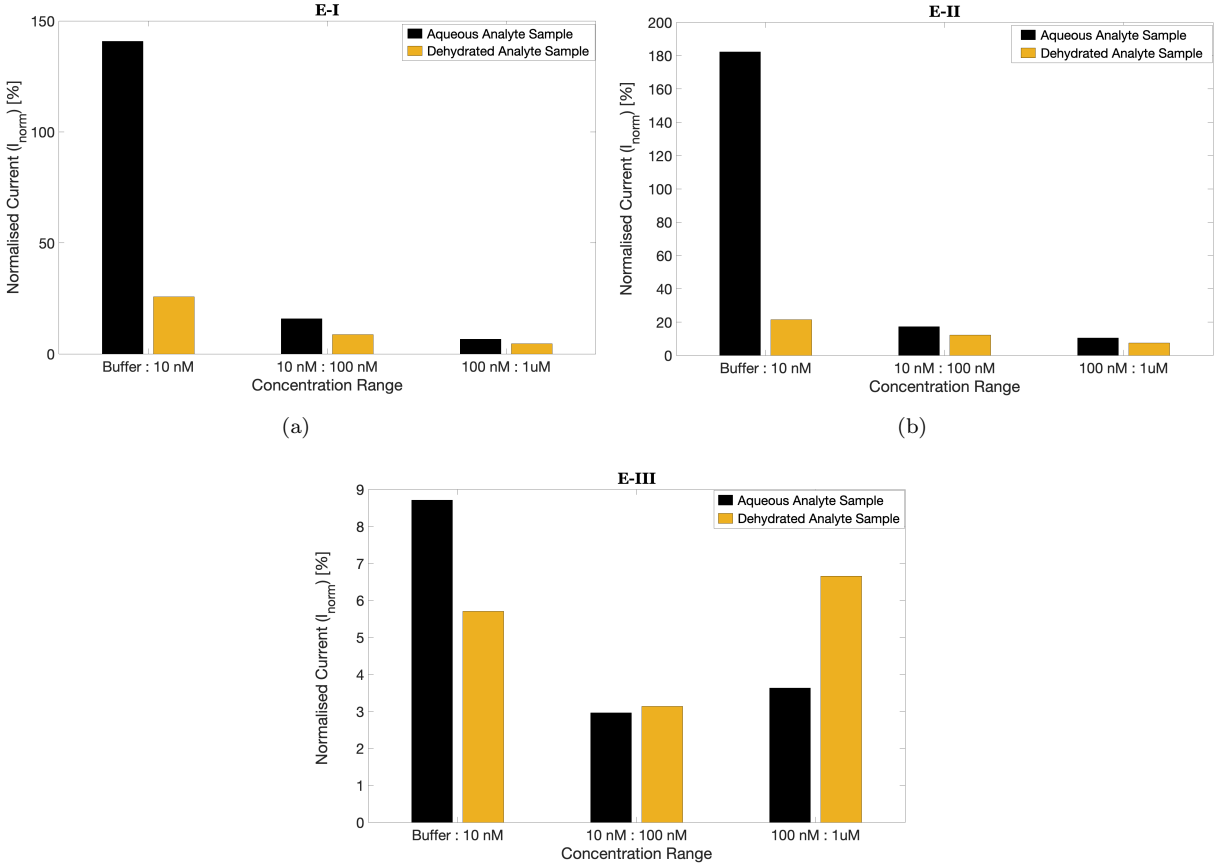

Figure 7.7: Comparing changes in the normalised current as the analyte concentration is increased in 10-fold increments. (a) aqueous miDNA21-P21 SHORT duplexes vs dehydrated miDNA21-P21 SHORT duplexes (b) aqueous miDNA21-P21 LONG duplexes vs dehydrated miDNA21-P21 LONG duplexes (c) aqueous miRNA21-P21 SHORT duplexes vs dehydrated miRNA21-P21 SHORT duplexes.

$$I_{norm} = \frac{I_{High} - I_{low}}{I_{low}} \tag{7.1}$$

Figure 7.6 shows that as the concentration of the analyte increases, I_{norm} diminishes for both Aqueous and Dehydrated Samples. Figure 7.6(a) consistently shows that NWFETs were more sensitive to changes in aqueous miDNA21-P21 LONG duplex (E-II) concentration than changes to the aqueous miDNA21-P21 SHORT duplex (E-I) concentration. This was expected on account of the long probes having more charge than the short probes.

For both LONG and SHORT duplex samples, there was a large drop in I_{norm} as the analyte concentration increased from 10 nM to 100 nM (10 nM:100 nM). The drop in I_{norm} was less pronounced between 100 nM and 1 μM. In Figure 7.6(b) the NWFETs response to changes in dehydrated miDNA21-P21 LONG duplex (E-II) concentration concentration is more sensitive than to changes in dehydrated miDNA21-P21 SHORT duplex (E-I). The only exception to this trend the change in concentration from Buffer to 10 nM. The drop in I_{norm} was more gradual for the Dehydrated analyte samples than

it was for the Aqueous sample. In conclusion, it was seen, as expected, that the change in normalised current as a result of changes in miDNA21-P21 LONG duplex (E-II) concentration was greater than the change in normalised current as a result of changes in miDNA21-P21 SHORT duplex concentration. The general trend observed was that as the concentration of the analyte increases, the I_{norm} of the NWFETs diminished in response to both Aqueous and Dehydrated Samples.

7.3.2 Differences between Aqueous and Dehydrated Samples

This investigation was also designed, in part, to observe whether there would be difference between the NWFETs response to aqueous samples and dehydrated samples. The aim here was to determine the best conditions in which to conduct the sensing experiments. From the results it was seen that the NWFETs were more sensitive to aqueous analyte samples than dehydrated samples Figure 7.7. There were 2 data points however, that deviated from this trend, 10 nM:100 nM and 100 nM:1 μM in Figure 7.7(c). As in the previous subsection, the general trend observed in Figure 7.7 is a decrease in I_{norm} as the concentration was increased. An anomaly was observed in Figure 7.7(c) where I_{norm} was seen to increase when the concentration of the analyte was increased from 100 nM:1 μM.

7.4 Discussion of Device Sensitivity

Table 7.4: Sensitivity of the NWFETs to ten-fold changes in analyte concentration across all three experiments. See Figure F.1 for calculations.

	E-I	E-II	E-III
AQUEOUS SAMPLES	43.88%	54.04%	5.07%
DEHYDRATED SAMPLES	12.65%	13.56%	5.15%

These result obtained from this investigation confirmed that ZnO NWFETs can detect the presence of miRNA21 duplexes. Equally as important was the demonstration of the ability to detect changes in miRNA concentration. This is significant because changes in miRNA concentration in a number of cases can be used as an early diagnosis of cancer and as a sufficient predictor the efficacy of cancer treatment.

It was interesting to note that NWFETs were more sensitive to presence of the miDNA and miRNA duplexes in aqueous conditions than in dehydrated conditions. In calculating the Sensitivity of the NWFETs to ten-fold changes in analyte concentration across all three experiments, Equation 7.2 [68] was used. I_n and I_0 correspond to the current response corresponding to the lowest and highest concentration of analyte, respectively.

$$Sensitivity = \left(\frac{I_n}{I_0}\right)^{\frac{1}{n}} - 1 \tag{7.2}$$

In calculating Sensitivity, the result of which are listed in Table 7.4, it was observed that the NWFETs were more sensitive to changes in concentration of the miDNA and miRNA duplexes in aqueous conditions than in dehydrated conditions. As shown above, Figure 7.7 supports this finding. Furthermore, it was seen that the NWFETs were more sensitivity to the changes in the concentrations of the long probe duplexes(E-II) than to to the changes in the concentrations of the short probe duplexes (E-I) for both aqueous and dehydrated samples. Figure 7.6 depicts this observation. From these results we can conclude that, with regards to Sensitivity, it is advantageous to use the LONG-probe duplex instead of the SHORT-probe duplex. There is, however, no advantage to be gained by dehydrating the samples. The forced physisorption of the analyte to the device's surface does not improve Sensitivity.

The figures presented in Table 7.4 give a broad idea of how the NWFETs response changes as a result of a 10-fold increase in analyte concentration. To get a more detailed picture of how the NWFETs response changes as a result of changes in concentration, it is helpful to refer to Figure 7.6 and Figure 7.7. Figure 7.6 shows that as the concentration of the analyte increases, I_{norm} diminishes for both long probe and short probe duplexes. That is to say, as the analyte concentration is increased in 10-fold increments, the corresponding increments in the NWFETs responses gets smaller and smaller. This seems to indicate that the NWFETs current response is nearing saturation as the analyte concentration is increased in 10-fold increments. Diminishing I_{norm} values are also observed in Figure 7.7 where aqueous and dehydrated samples are compared for each type of analyte. This also seems to sure support the idea that that the NWFETs current response is nearing saturation as the analyte concentration is increased in 10-fold increments.

The NWFETs used in each experiment were biased in the Subthreshold region. Thus, the diminishing I_{norm} values seem to indicate that drain current response of NWFETs is nearing the Saturation region. The On/Off ratios of the devices used in these experiments ranged from 10^3 to 10^5. In future investigations involving these ZnO NWFETs it would be worthwhile to explore whether devices with much larger On/Off ratio say 10^{10} are more likely to produce constant I_{norm} values over a wider range of concentrations. Our current hypothesis, which needs investigating, is that NWFETs with larger On/Off ratios could be biased further away from the Saturation region. This would enable the device to operate in the Subthreshold region over a much larger range of analyte concentrations. As there is a linear relationship between changes in gate voltage and drain current in the Subthreshold region, it is expected that I_{norm} values would be constant when the device is operating in this region.

7.5 Results and Discussion of Repeated miDNA and miRNA Detection Experiments

Just like with the initial experiments, three different 512 ZnO NWFET arrays were used in the repeat E-I, E-II and E-III experiments. The switching characteristics of the devices used are shown

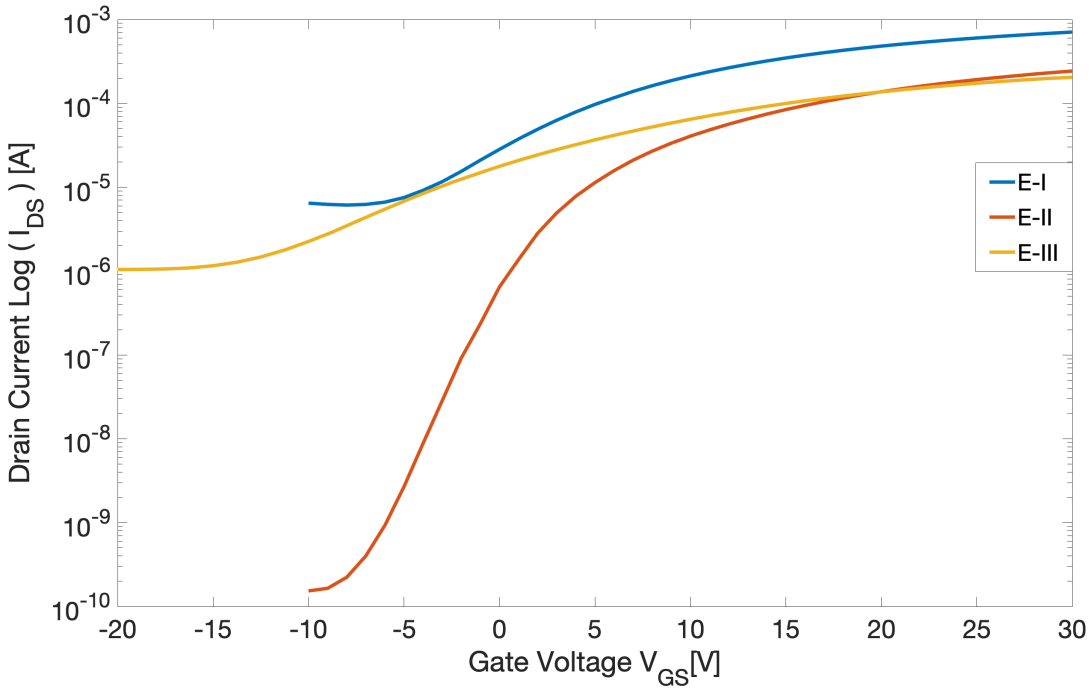

Figure 7.8: I_DV_G curve of the ZnO NWFET arrays used in each repeat experiment. Each I_DV_G sweep was conducted in dry conditions. The bias point for the devices used in each repeat experiment is presented as follows: (Experiment identifier, Gate Voltage, Drain Voltage, Drain Current). (E-I, 1 V, 5 V, 37 uA); (E-II, 1 V, 3 V, 1.37 uA); (E-III, -5 V, 1 V, 6.816 uA).

in Figure 7.8. While the On-Off ratio for the devices used in the repeat E-I and E-III experiments is approximately 10^2, it was sufficient to show distinct current output response to change in analyte concentration.

The results of the repeat of experiment E-I are displayed in Figure 7.9. Figure 7.9(a) shows the drain current response of the NWFET array to aqueous buffer and aqueous miDNA21-SHORT duplex samples. Figure 7.9(b) shows the drain current response to dehydrated buffer and dehydrated miDNA21-SHORT duplex samples. The results of the repeat of experiment E-II are displayed in Figure 7.10. Figure 7.10(a) shows the drain current response of the NWFET array to aqueous buffer and aqueous miDNA21-Long duplex samples. Figure 7.10(b) shows the drain current response to dehydrated buffer and dehydrated miDNA21-Long duplex samples. The results of experiment E-III are displayed in Figure 7.11. Figure 7.11(a) shows the drain current response of the NWFET array to aqueous buffer and aqueous miRNA21-SHORT duplex samples. Figure 7.11(b) shows the drain current response to dehydrated buffer and dehydrated miRNA21-SHORT duplex samples.

In all the graphs Fig Figure 7.9, Figure 7.10 and Figure 7.11 it can be seen that as the analyte concentration was increased the Drain Current Response also increased. This trend was observed in the results obtained from all the repeat experiments and for both aqueous and dehydrated samples. There is a clear distinction between the signals produced at each analyte concentration. The data indicates that as the concentration of the analyte is increased, there is a positive increase in potential at the surface of the NWFETs. This had the effect of increasing the positive bias on the NWFETs

such that the drain current increased. Consequently, changes in concentration in miDNA-21 and miRNA-21 can be detected. This was the same trend observed in the previous chapter, thus giving further credence to the obtained results.

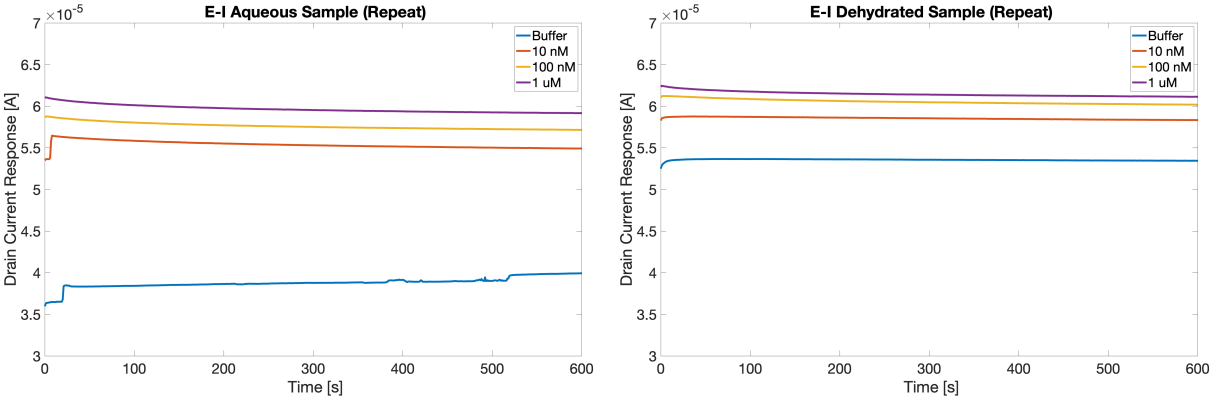

(a) (b)

Figure 7.9: The drain current response of the NWFETs to the buffer and analyte samples. The analyte in this instance was the miDNA21-P21 SHORT duplex (D21-Short) (a) These were results obtained when the NWFET array was wetted with each aqueous sample. (b) These were results obtained when the aqueous component of each sample was evaporated from the surface.

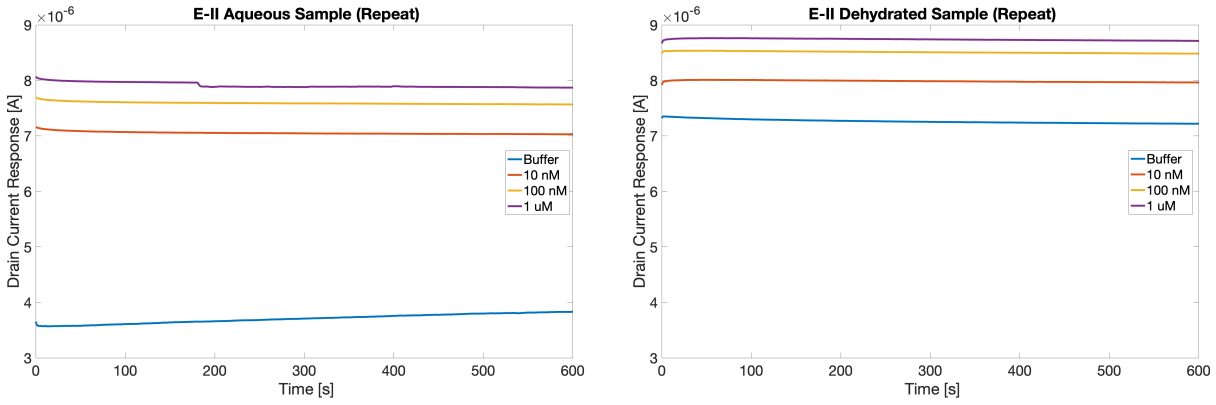

(a) (b)

Figure 7.10: The drain current response of the NWFETs to the buffer and analyte samples. The analyte in this instance was the miDNA21-P21 LONG duplex (D21-Long) (a) These were results obtained when the NWFET array was wetted with each aqueous sample. (b) These were results obtained when the aqueous component of each sample was evaporated from the surface.

Figure 7.12 shows that as the concentration of the analyte increases, Sensitivity diminishes for both Aqueous and Dehydrated Samples. Figure 7.12(a) consistently shows that were larger changes in the normalised current in response to changes in aqueous miDNA21-P21 LONG duplex (E-II) concentration than changes to the aqueous miDNA21-P21 SHORT duplex (E-I) concentration. This was

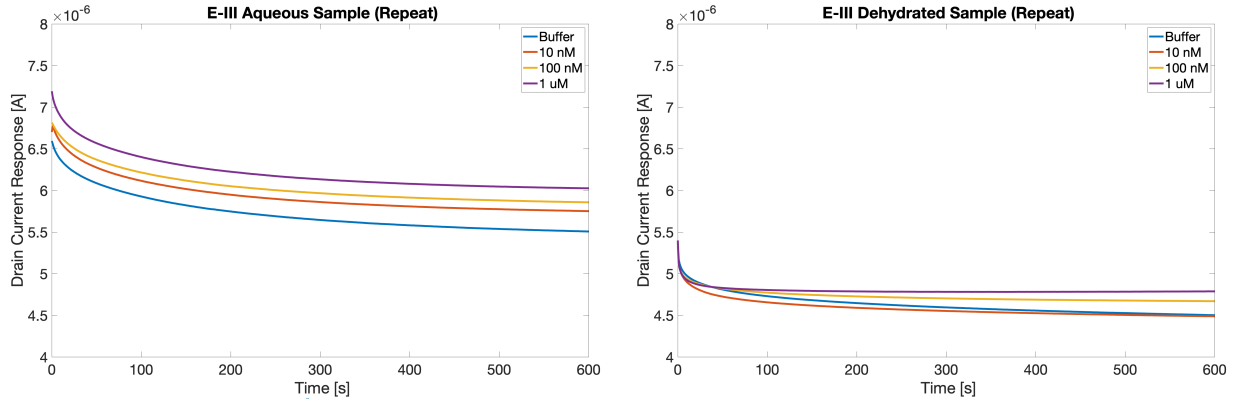

(a) (b)

Figure 7.11: The drain current response of the NWFETs to the buffer and analyte samples. The analyte in this instance was the miRNA21-P21 SHORT duplex (R21-Short) (a) These were results obtained when the NWFET array was wetted with each aqueous sample. (b) These were results obtained when the aqueous component of each sample was evaporated from the surface.

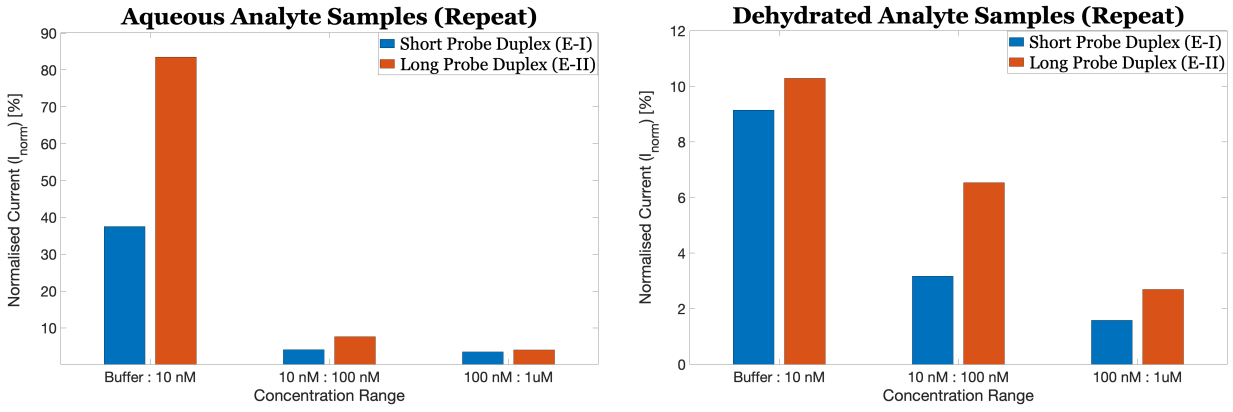

(a) (b)

Figure 7.12: Comparing changes in the normalised current as the analyte concentration is increased in 10-fold increments. (a) aqueous miDNA21-P21 SHORT duplexes (E-I) vs aqueous miDNA21-P21 LONG duplexes (E-II) (b) dehydrated miDNA21-P21 SHORT duplexes (E-I) vs dehydrated miDNA21-P21 LONG duplexes (E-II).

expected on account of the long probes having more charge than the short probes. As seen previously, there was a large drop in the normalised current as the analyte concentration increased from 10 nM:100 nM. This was less pronounced between 100 nM:1 μM.

In Figure 7.12(b) the NWFETs response to changes in dehydrated miDNA21-P21 LONG duplex (E-II) concentration concentration was more pronounced than to changes in dehydrated miDNA21-P21 SHORT duplex (E-I). Again, the decrease in normalised current was more gradual for the Dehydrated analyte samples than it was for the Aqueous sample. In conclusion, the results of the repeated experiments appear to confirm the expected, that the change in normalised current as a result of changes in miDNA21-P21 LONG duplex (E-II) concentration was greater than the change in normalised current

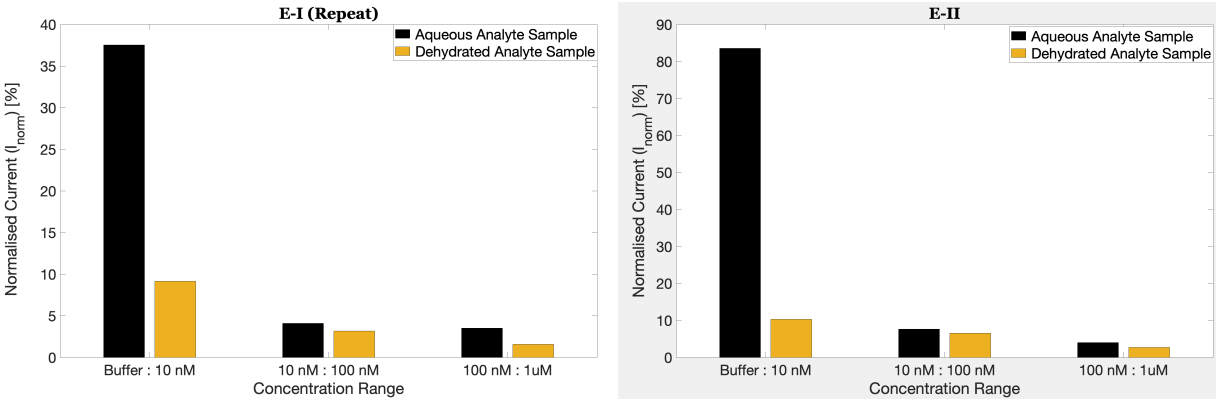

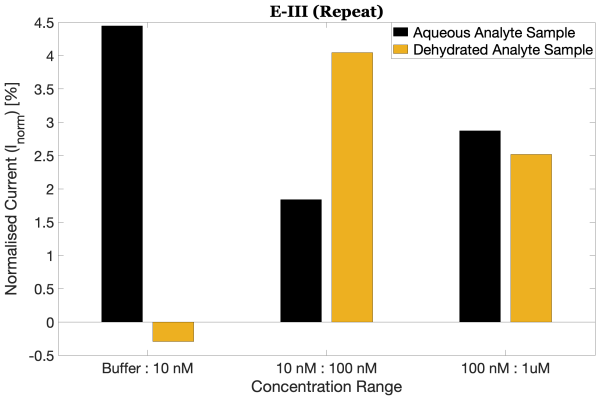

Figure 7.13: Comparing changes in the normalised current as the analyte concentration is increased in 10-fold increments. (a) aqueous miDNA21-P21 SHORT duplexes vs dehydrated miDNA21-P21 SHORT duplexes (b) aqueous miDNA21-P21 LONG duplexes vs dehydrated miDNA21-P21 LONG duplexes (c) aqueous miRNA21-P21 SHORT duplexes vs dehydrated miRNA21-P21 SHORT duplexes.

as a result of changes in miDNA21-P21 SHORT duplex concentration. In comparing the results of each experiment it was also seen that the NWFETs produced a larger response to aqueous analyte samples than dehydrated samples Figure 7.13. This underscores the observation made in the previous chapter that NWFETs were more sensitive to presence of the miDNA and miRNA duplexes in aqueous conditions than in dehydrated conditions.

Table 7.5: Sensitivity of the NWFETs to ten-fold changes in analyte concentration.

	E-I	E-II	E-III
AQUEOUS SAMPLES	14.00%	27.12%	3.05%
DEHYDRATED SAMPLES	4.58%	6.46%	2.07%

The results obtained from the repeat investigations support the results reported in the previous chapter. In the repeat investigations it was seen that the NWFETs were more sensitive to changes in concentration of the miDNA and miRNA duplexes in aqueous conditions than in dehydrated conditions. Furthermore, it was seen that the NWFETs were more sensitivity to the changes in the concentrations of the long probe duplexes(E-II) than to the changes in the concentrations of the short probe duplexes (E-I) for both aqueous and dehydrated samples Table 7.5. This gives more gravitas to the conclusions that it is advantageous to use the LONG-probe duplex instead of the SHORT-probe duplex; and that there is no advantage to be gained by dehydrating the samples. The results of the repeat experiments also support the observation that in the previous chapter where I_{norm} diminished for both long probe and short probe duplexes and both aqueous and dehydrated conditions as the analyte concentration was increased in 10-fold increments. These result also seem to indicate that the NWFETs current response is nearing saturation as the analyte concentration is increased in 10-fold increments.

7.6 Analysis and Discussion

Given that miDNA-21 and miRNA-21 are negatively charged analyte and the ZnO NWFETs used in these experiments operate as n-type devices, it could be expected that as the analyte concentration increased the drain current would decrease, assuming that the analyte is the only charge source. This is on account of the negatively charged analyte negatively biasing the n-type nanowire. The experimental data shows the opposite trend. Figure 7.3, Figure 7.4 and Figure 7.5 indicate that as the concentration of the analyte is increased, the drain current increased.

In the experiments conducted one can rule out the desorption of the analyte from the surface of the NWFETs as the cause of the positive correlation between changes in concentration of negatively charged analyte and the increase in the drain current response, as been observed with other n-type FETs [149] [150]. This is because the samples used in this experiment were dehydrated to force the physisorption of analyte to surface of the NWFETs and yet the drain current increased as the analyte concentration increased.

Before introducing the analyte, NWFETs were biased in the subthreshold region. This resulted in electrons accumulating to form a channel between source and drain at the bottom gate oxide-nanowire interface. When NWFETs were wetted with the analyte samples an increase in drain current was observed. In the absence of another external source of electrons, this phenomena indicates that the increase in the current is as a result of the depletion of the top oxide-nanowire interface of electrons which accumulate at the bottom gate oxide-nanowire interface. As the concentration of negatively charged analyte increases, the surface potential becomes increasingly negative. Consequently, the depletion region at the top oxide-nanowire interface grows Figure 7.14. This results in the observed increase in current as more electrons accumulate at the bottom oxide-nanowire interface. Figure 7.15 shows a band energy schematic depicting of the accumulation and depletion regions.

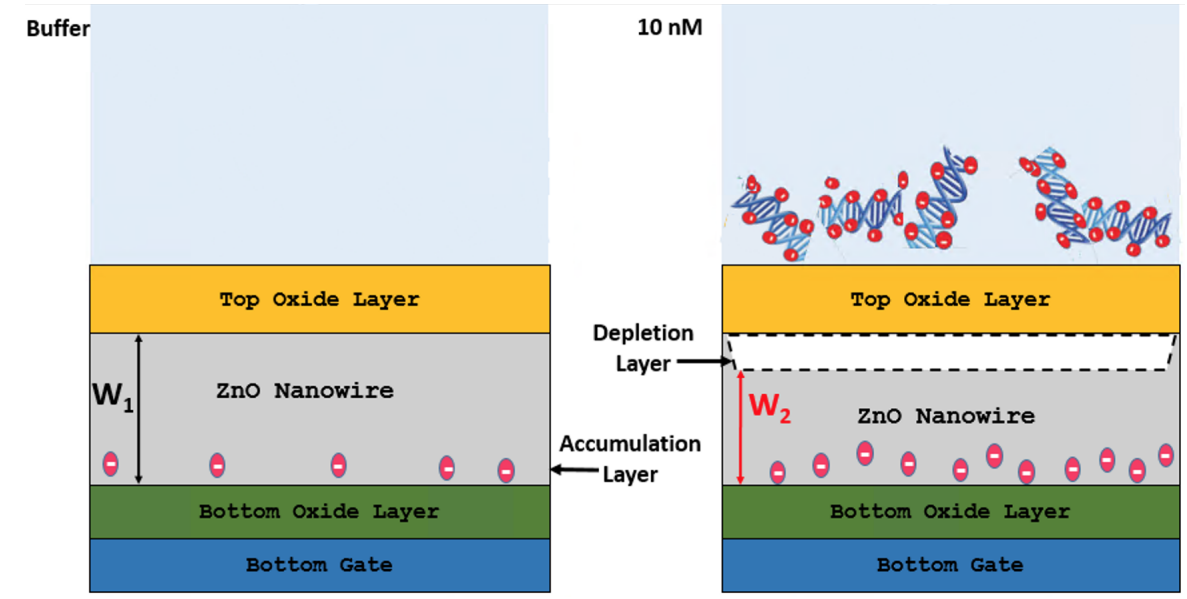

(a)

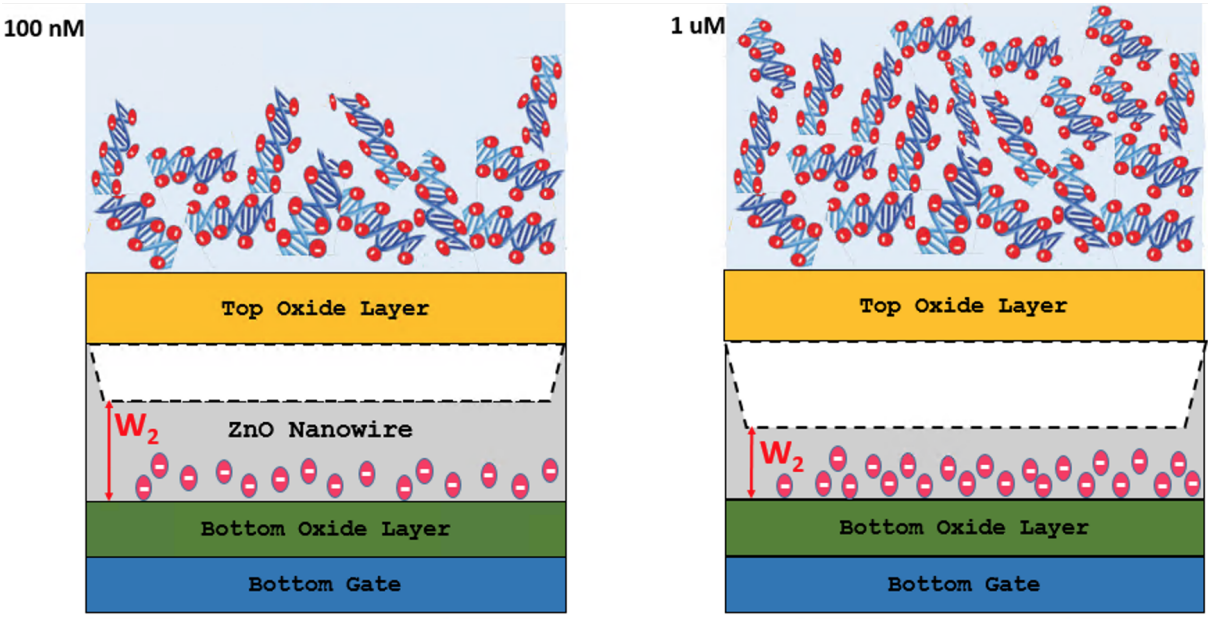

(b)

Figure 7.14: A schematic that depicts a growing depletion and accumulation layers in response to 10-fold increases in analyte concentration. As ZnO has very low hole carrier because of its dominant n-type carrier, depletion region is represented as a shaded region. This is in place of using a "+" sign to represent a small concentration of minority hole carriers that is sufficient for inversion like layer.

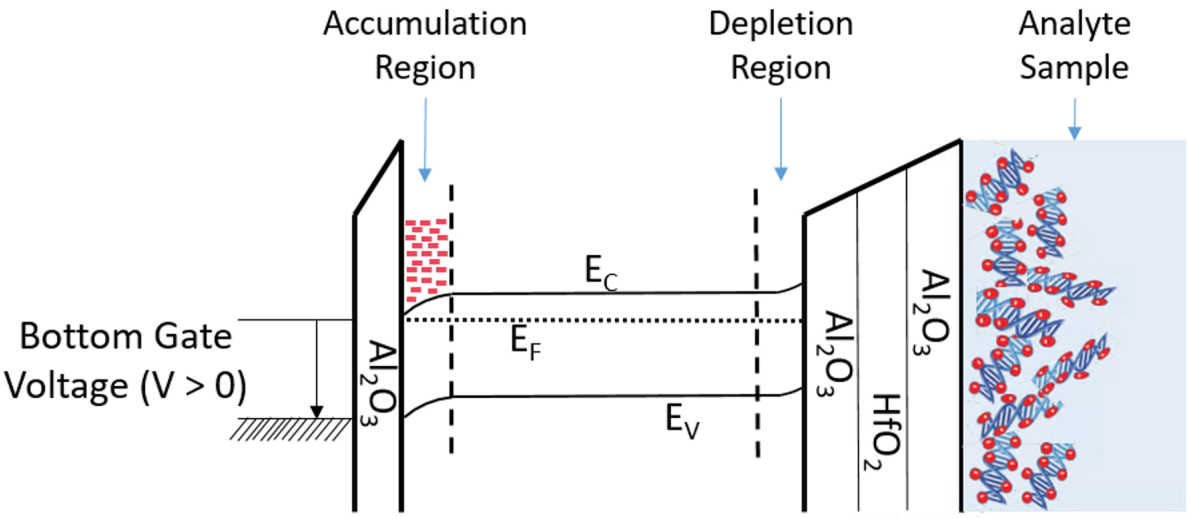

Figure 7.15: A band energy schematic depicting of the accumulation and depletion regions

In considering how the threshold voltage of a depletion mode device changes in response to the presence of the analyte, its helpful to refer to Equation 7.3 [151] where V_{FB}, $2\Psi_B$ and V_{Dep} are the Flat band voltage, bulk potential and depletion voltage respectively. The depletion voltage can be represented as the product of the charge of electron q $(1.60218 \times 10^{-19} C)$, electron donor concentration N_D (cm^{-3}), and the depletion width W_1 (m) divided by the capacitance of the gate oxide per unit area C_{ox} (F) Equation 7.4. W_1 is the initial depletion width of the device with respect to the gate voltage applied at the bottom gate.

$$V_T = V_{FB} + 2\Psi_B - V_{Dep} \tag{7.3}$$

$$V_T = V_{FB} + 2\Psi_B - \frac{qN_D W_1}{C_{ox}} \tag{7.4}$$

As described above the presence of the analyte results in an increase in drain current as electrons, depleted at the top oxide-nanowire interface, accumulate at the bottom gate oxide-nanowire interface. As this occurs W_2 decreases. Equation 7.5 describes how the threshold voltage changes in the presence of the analyte assuming $W_2 < W_1$. As seen from Equation 7.5, the threshold voltage diminishes as the V_{Dep} term grows. That is, as W_2 decreases due to the analyte induced growth of the depletion region, the threshold voltage becomes increasingly smaller.

$$V_{T_{WithAnalyte}} = V_{FB} + 2\Psi_B - \left(\frac{qN_D}{C_{ox}}(W_1 - W_2)\right) \tag{7.5}$$

The following Equation 7.6, describes the relationship of the drain current I_{DS} and threshold voltage V_T in the subthreshold region where Z (m) is the channel width, L (m) is the channel length and μ_n is the mobility of the minority carriers $(cm^2/V.s)$ [66]. From Equation 7.6 it can be seen that as

the V_T term decreases, the drain current increases. In summary, as 10-fold increments in the analyte induces the decrease of W_2, the threshold voltage decreases. Given that all other parameters remain constant, per Equation 7.6, this results in an increase in the drain current as electrons depleted at the top oxide-nanowire interface accumulate at the bottom gate oxide-nanowire interface.

$$I_{DS} = \frac{Z}{L}\mu_n C_{ox}(V_G - V_T - \frac{V_D}{2})V_D \tag{7.6}$$

Figure 7.6 and Figure 7.7 show that as the analyte concentration is increased in 10-fold increments, the corresponding increments in the NWFETs responses gets smaller and smaller. It appears that the NWFETs current response is nearing saturation as the analyte concentration is increased in 10-fold increments. This seems to indicate that the depletion region, and by the extension the rate at which electrons accumulate at the bottom oxide, is growing at a diminishing rate.

7.6.1 Comparing Contrasting Results

Table 7.6: Sensitivity of the NWFETs to ten-fold changes in Single strand miDNA-21 and Double strand miDNA-21.

	Single strand miDNA-21	Double strand miDNA-21
AQUEOUS SAMPLES	-3.39%	67.06%
DEHYDRATED SAMPLES	-8.82%	16.93%

In a previous paper [18] ZnO NWFETs were used to detect the presence of 100 nM single strand miDNA-21 (ssDNA) in TE Buffer sample (10 μM Trizma, 50 μM KCl, 1 μM EDTA). In that experiment a decrease in current was observed when the NWFETs were wetted with the analyte Figure 7.16. Those results are in contrast with the results presented in this chapter. The main differences to highlight between both experiments are the type of analyte used and the ionic strength of the buffers. In the previous experiment the analyte was 100 nM single strand miDNA-21. The ionic strength of that buffer was 50 μM KCl and the Debye length was approximately 43 nm. In this experiment 100 nM double strand miDNA-21 (dsDNA) was used. The ionic strength of this buffer was 10 mM KCl and the Debye length was approximately 3.04 nm. The reason for using a buffer with a higher ionic strength, and thus reducing Debye length, was to bring Debye length into more realistic range. That is, closer to the 0.7 nm the Debye length of physiological samples which typically have an ionic strength of 150 mM.

An article by Tarasov et al [103] demonstrated that increasing the ionic concentration of the buffer effectively increases the negative surface potential at the oxide-electrolyte concentration. This fact in combination with the fact that double strand miDNA-21 has twice the electric charge of single strand

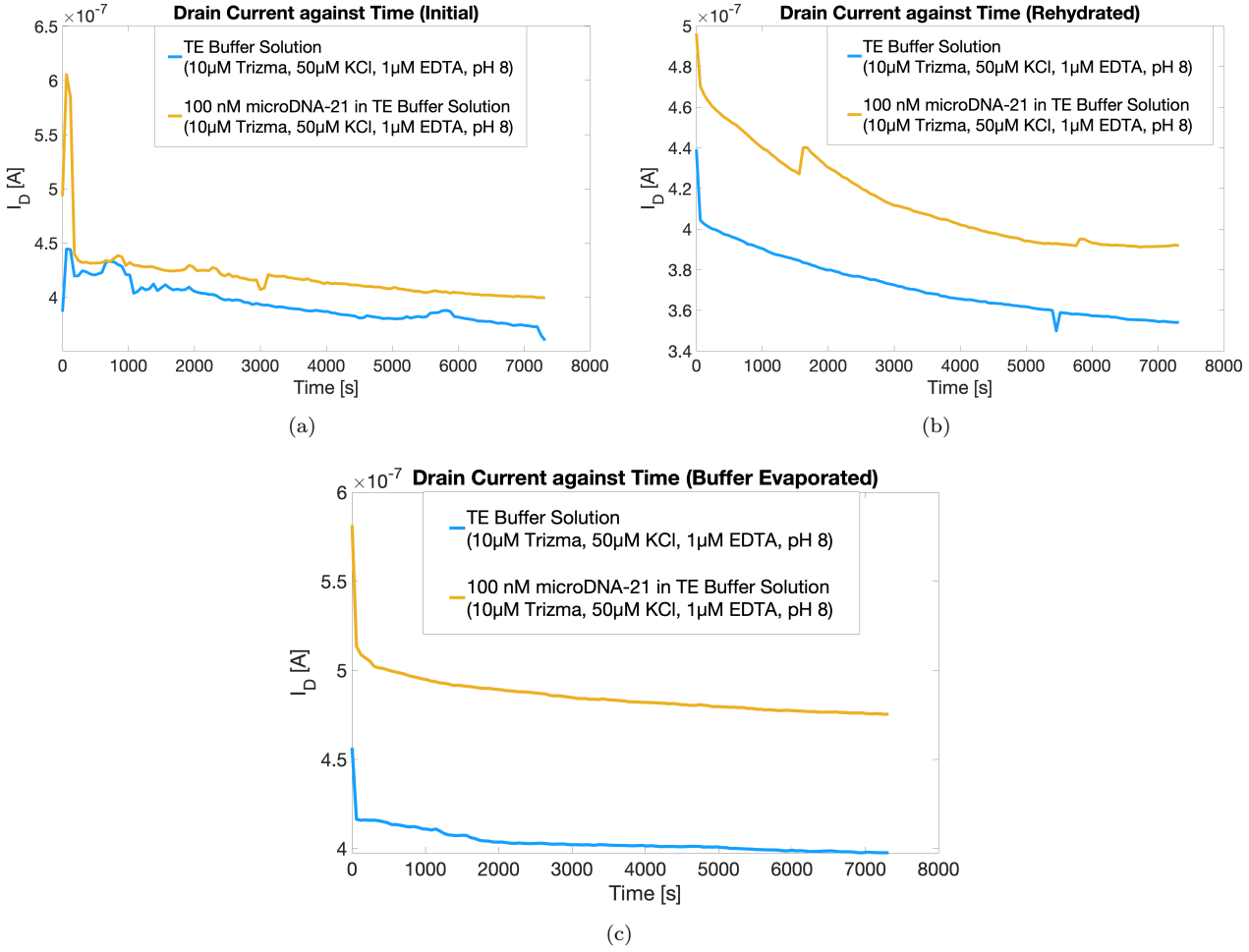

Figure 7.16: (a) Drain Current against Time graph for ZnO NWFETs with a stack insulator in TE Buffer and then in a solution of TE Buffer with 100 nM miDNA-21. (b) Drain Current against Time graph of the NWFETs in rehydrated TE Buffer and then in a rehydrated solution of TE Buffer with 100 nM miDNA-21. (c) Drain Current against Time graph for NWFETs obtained after TE Buffer was allowed to evaporate.[18]

miDNA-21 aids in explaining the difference in the results produced by both experiments. Double strand miDNA-21 in the stronger ionic buffer causes a more pronounced depletion of the nanowire near the top oxide-channel interface than the single strand miDNA-21 in the weaker ionic buffer. This results in the increased accumulation of electrons at the bottom oxide which is seen as an increase in the drain current.

Table 7.6 shows the Sensitivity of the NWFETs to analyte used in both experiments. The magnitude of the Sensitivity values demonstrate that NWFETs generate a much stronger response to 10-fold increases in the concentration of double strand miDNA-21 in the stronger ionic buffer than to 10-fold increases in the concentration of single strand miDNA-21 in the weaker ionic buffer. Those values support the rationale that the increase in the ionic concentration of the buffer and the double strand miDNA-21 would result in larger positive increase in the drain current than the single strand miDNA-21 in the weaker ionic buffer. This is due to the more pronounced depletion of the nanowire near the

top oxide-channel interface, resulting in the accumulation of electrons at the bottom oxide which is seen as an increase in the drain current.

As mentioned above, the experiments presented by Majd et al [149] and Lee et al [150] produced a positive correlation between changes in concentration of negatively charged analyte and the increase in the drain current response. This positive correlation was attributed to the desorption of the analyte from the surface of the NWFETs however, both papers did not show fluorescent images [152] that could corroborate the desorption theory. The ionic salt concentrations of the buffers used in these were 10mM [149] and $0.1 \times PBS$ [150]. The calculated Debye lengths of these buffers range between $2 - 3\ nm$ and the Debye length of the buffer used in the experiment presented in this chapter fits within this range. Furthermore, the results reported by Majd et al and Lee et al follow the same trend as presented in this thesis. That is, increasing drain currents in response to increasing concentration of negatively charged analyte. Although their experimental setup differs from the one detailed here, it follows that theory put forward in this thesis can be used to explain the findings reported in those papers. That is to say, the observed increase in the drain current resulting from increasing the concentration of negatively charged analyte can be explained with the premise that stronger ionic buffers cause the increased accumulation of electrons.

7.7 Conclusion

In this chapter it was demonstrated that the NWFETs can distinguish between the different concentrations of miRNA. The result of the investigation was compelling. The ZnO NWFETs were found to have a 43.88% Sensitivity to one order of magnitude changes in miDNA concentration (10 nM, 100 nM and 1 μM). In the subsequent investigation with miRNA as the analyte, the ZnO NWFETs were found to have a 5.07% Sensitivity to one order of magnitude changes in miRNA concentration of (10 nM, 100 nM and 1 μM). Repeats of the aforementioned experiments yielded 14.00% Sensitivity to one order of magnitude changes in miDNA concentration and a 3.05% Sensitivity to one order of magnitude changes in miRNA concentration.

Increases in the drain current due to changes in analyte concentration were attributed to the depletion of the nanowire near the top oxide-channel interface, resulting in the accumulation of electrons at the bottom oxide. As the concentration of negatively charged analyte was increased, the surface potential became increasingly negative. Consequently, the depletion region at the top oxide-nanowire interface grew. This resulted in the observed increase in current as more electrons accumulated at the bottom oxide-nanowire interface. Furthermore, as the analyte concentration was increased in 10-fold increments current response of the NWFETs appeared to be nearing saturation. This seemed to indicate that the depletion region, and by the extension the rate at which electrons accumulate at the bottom oxide, was growing at a diminishing rate. Following this, the differences between the results generated by single strand miDNA and double strand miDNA were explained using the accumulation-depletion model. The magnitude of the Sensitivity values demonstrated that NWFETs generate a much stronger response to 10-fold increases in the concentration of double strand miDNA-21

in the stronger ionic buffer than to 10-fold increases in the concentration of single strand miDNA-21 in the weaker ionic buffer. Those values support the rationale that the increase in the ionic concentration of the buffer and the double strand miDNA-21 would result in larger positive increase in the drain current than the single strand miDNA-21 in the weaker ionic buffer. This is due to the more pronounced depletion of the nanowire near the top oxide-channel interface, resulting in the accumulation of electrons at the bottom oxide which is seen as an increase in the drain current.

In the next chapter concludes this thesis by summarising the main findings detailed in the previous chapters. It ends with a look ahead to the future and a brief discussion on the next steps on the path of developing a Point-of-Care device.

Chapter 8

Concluding Remarks

8.1 Conclusion

Point of Care (PoC) devices are diagnostic devices which rapidly provide actionable information for patient care at the time and location of an encounter with the health care system. Field Effect Transistor (FET) biosensors, a promising class of PoC devices, have been shown to able to distinguish between different concentrations of molecular analyte [14]. This function would be vital in cancer diagnosis revolving around detection of the abnormal expression of miRNA. This is because cancerous cells typically manifest a deviation in miRNA concentration from the normal range.

In pursuit of the goal of developing a FET biosensor for cancer diagnostic applications, the preliminary step was to fabricate FETs capable of detecting changes in miRNA concentration. The FETs fabricated for this purpose were Zinc Oxide Nanowire Field Effect Transistors (NWFETs) arrays. ZnO is an ideal material with which to fabricate these NWFETs because it is naturally a n-type semiconductor [15], thus eliminating the need for a high temperature doping process steps. ZnO has a large and direct band-gap (3.37 eV [16]) which enables it to sustain large electric fields; withstand higher breakdown voltages; generate lower levels of noise; and operate at high temperatures and levels of power [17]. The ZnO NWFETs were passivated with stack high-κ dielectrics. The stack layer consists of a layer of Hafnium dioxide sandwiched between two Aluminium oxide layers which has been shown to diminish threshold voltage drift effectively [18]. Once fabricated, the ZnO NWFETs were first tested to observe how well they functioned as transducers of ionic charge. The ZnO NWFETs were seen to be excellent transducers of ionic charge with a shift in gate voltage per pH of 117 mV/pH. This shift in gate voltage per pH is comparable to largest known value of 220 mV/pH recorded by Knopfmacher's single Silicon NWFET with a Dual Gate [19]. It is also twice as large as the Nernst limit (59 mV/pH).

Following the pH-sensing experiment, a microDNA(miDNA) detection investigation was conducted. miDNA are the stable biological equivalent of miRNA and thus can serve as proxy of miRNA detection. The result of the investigation was compelling. The ZnO NWFETs were found to have a 43.88%

Sensitivity to one order of magnitude increments of miDNA concentration (10 nM, 100 nM and 1 μM). Subsequently, the same investigation was carried out with miRNA as the analyte. In this instance the ZnO NWFETs were found to have a 5.07% Sensitivity to one order of magnitude increments of miRNA concentration (10 nM, 100 nM and 1 μM). These results irrevocably demonstrate that ZnO NWFETs are capable of detecting changes in miRNA concentration. Thus, making ZnO NWFETs a suitable candidate for the development of a PoC device with which to conduct cancer diagnostics.

8.2 Future Work

Presently, medical diagnostic tests, by and large, are performed in laboratories equipped with bench-top analyzers and operated by trained lab technicians. Although these systems have a high throughput, in most cases patients wait a number of days to receive their test results [10]. Being able to perform diagnostic tests at or near the site where patients encounter the health care system, and receiving the results within the time frame of a consultation with a healthcare professional (approximately 15 minutes [11]), would be extremely beneficial. It would provide actionable information that can lead to several changes in patient management. This would include but is not limited to, facilitating the containment of infectious disease outbreaks; reducing the need for multiple patient visits; enabling the prompt treatment of an illness in a more targeted fashion; and reducing the reliance on presumptive treatment thereby safeguarding antibiotics and stemming antimicrobial resistance [153].

Point of Care (PoC) devices, diagnostic devices which rapidly provide actionable information for patient care at the time and location of an encounter with the health care system, are becoming more prevalent. The most commonly found type of PoC device is the Lateral Flow Immunoassays (LFIA) [12] [13]. However, LFIA conventionally provide qualitative results (i.e., yes or no) which are of little use when trying to gauge changes in concentration as would be needed in detecting the loss or amplification miRNA strands. Furthermore, LFIA suffers from difficulties due to varying consistency of the flow rate and to non-uniform dispersion of the sample to label [10].

Field Effect Transistor (FET) biosensors, a promising class of PoC devices, have been shown to able to distinguish between different concentrations of molecular analyte [14]. These FETs are typically made with established semiconductor techniques and technologies meaning that they can be readily integrated with other electronic systems. This would enable on chip signal processing and the instantaneous electronic transmission of results from remote areas to a centralised hub. This would particularly useful in instances where the progress of an infectious through a population needs to be tracked and traced.

The goal is to leverage the advantages in semiconductor technologies to develop a PoC device for cancer diagnostics. In doing so we hope to enable cancers to be caught and treated earlier thus reducing the need for invasive or debilitating treatments like surgery or chemotherapy. These result obtained from the investigation detailed above confirmed that, ZnO NWFETs can detect the presence of miRNA21, a known cancer biomarker. Equally as important was the demonstration of the ability to detect changes in miRNA concentration within 10 minutes. This is significant because changes

in miRNA concentration in a number of cases has be used in the early diagnosis of cancer and as a sufficient predictor the efficacy of cancer treatment. These results form the basis upon which to build a PoC device for cancer diagnostics. The next major milestone along this journey is to use these ZnO NWFETs to distinguish between elevated or depressed miRNA concentration in unadulterated cell samples from cancerous cells; and miRNA concentration in unadulterated cell samples from normal cells.

Appendix A

Appendix A: Table of materials used to fabricate ZnO NWFETs

Table A.1: Table of materials used to fabricate ZnO NWFETs

Product	Supplier	Country
Silicon Wafer 150mm Prime Si < 100 > p-type Boron doping 1-10 Ohm-cm	Siegert Wafer	Germany
TMA CAS 75-24-1	Dockweiler chemical GmbH	Germany
DEZ CAS 557-20-0	Dockweiler chemical GmbH	Germany
TeMaHf CAS 352535-01-4	Dockweiler chemical GmbH	Germany
Al 99.999%	AJA International	USA
AL/Zn target (2:98) 99.99% I-901-D21	Testbourne Ltd	UK

Appendix B

Appendix B: Table of Photoresist used in fabricating ZnO NWFETs

Table B.1: Table of Photoresist used in fabricating ZnO NWFETs

Product	Supplier	Country
AZ2070	Microchemicals GmbH	Germany
AZ2070 verd 1:1.33	Microchemicals GmbH	Germany
LOR1A	Kayaku Advanced Materials	USA
SU-8	Kayaku Advanced Material	USA
LOR5A	Kayaku Advanced Materials	USA

Appendix C

Appendix C: Table of Tools used in fabricating ZnO NWFETs

Table C.1: Table of Tools used in fabricating ZnO NWFETs

Tool Name	Manufacturer
Brewer Resist Spinner	Brewer Science
Sawatech Hotplate	SAWATEC AG
Lithography Aligner EVG620T	EV Group
Fisher 15061 Ultrasonic Tank	Fisher Scientific
Oxford Instruments Plasma Tools FlexAL	Oxford Instruments
AJA Orion Sputtering Machine	AJA International
Tempress 150mm Oxidation Furnace	Tempress
Oxford Instruments Plasma Tools Ionfab 300	Oxford Instruments
Felcon Wet Bench	Felcon
Optical Microscope Nikon Stereomicroscope	Nikon
Woollam M-2000DI spectroscopic ellipsometer	J.A. Woollam
FIBSEM Zeiss Nvision 40 SEM	Zeiss

Appendix D

Appendix D: Table of Acids and Buffers used in experiments

Table D.1: Table of Acids and Buffers used in experiments

Product	Supplier	Country
Invitrogen UltraPure 0.5M EDTA, pH 8.0	Fischer Scientific	UK
Tris Hydrochloride, 1M Solution (pH 7.5/Mol. Biol.)	Fischer Scientific	UK
Fisher BioReagents Potassium Chloride (White Crystals)	Fischer Scientific	UK
microDNA21 (1.0 µmol synthesis scale)	ATDBio	UK
p21-SHORT (1.0 µmol synthesis scale)	ATDBio	UK
p21-LONG (1.0 µmol synthesis scale) with the C-terminus and N-terminus extended with C30	ATDBio	UK
microRNA 21 (0.2 µmol synthesis scale)	ATDBio	UK

Appendix E

Appendix E: Additional miDNA and miRNA Detection Experimental Data

E.1 Results

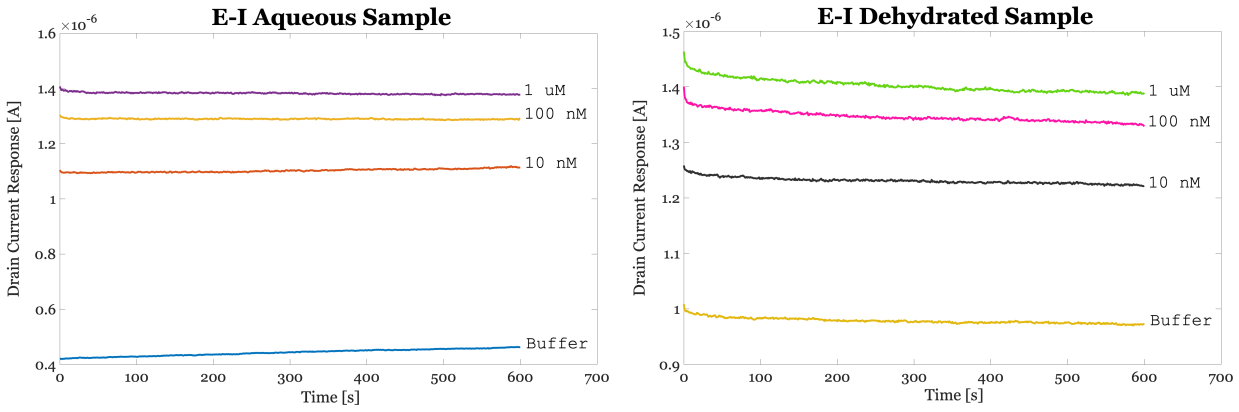

(a) (b)

Figure E.1: The drain current response of the NWFETs to the buffer and analyte samples. The analyte in this instance was the miDNA21-P21 SHORT duplex (D21-Short) (a) These were results obtained when the NWFET array was wetted with each aqueous sample. (b) These were results obtained when the aqueous component of each sample was evaporated from the surface.

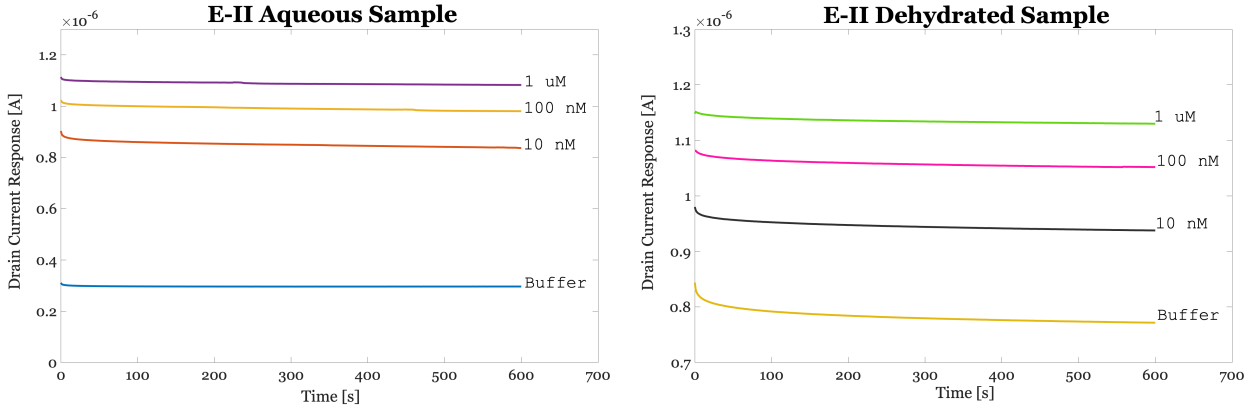

(a) (b)

Figure E.2: The drain current response of the NWFETs to the buffer and analyte samples. The analyte in this instance was the miDNA21-P21 LONG duplex (D21-Long) (a) These were results obtained when the NWFET array was wetted with each aqueous sample. (b) These were results obtained when the aqueous component of each sample was evaporated from the surface.

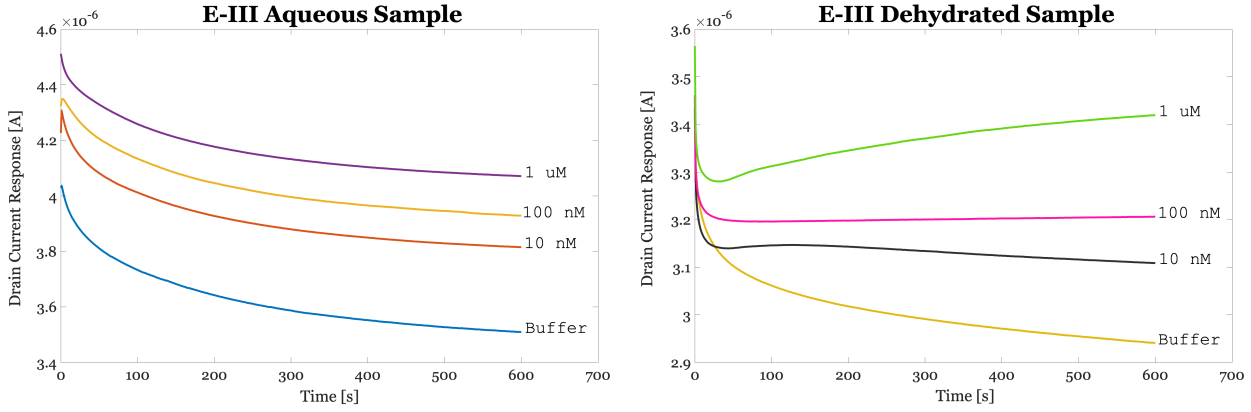

(a) (b)

Figure E.3: The drain current response of the NWFETs to the buffer and analyte samples. The analyte in this instance was the miRNA21-P21 SHORT duplex (R21-Short) (a) These were results obtained when the NWFET array was wetted with each aqueous sample. (b) These were results obtained when the aqueous component of each sample was evaporated from the surface.

Appendix F

Appendix F: Matlab Code to Calculate Sensitivity

```
% Final current reading at  600 seconds. Signal had settled by this point
% Order of currents in each array [Buffer, 10 nM, 100 nM, 1 uM]


Ei_Dehydrated=[9.71762000000000e-07,1.22151000000000e-06,1.32869000000000e-06,1.38928000000000e-06];
Eii_Dehydrated=[7.71576000000000e-07,9.37604000000000e-07,1.05186300000000e-06,1.12999000000000e-06];
Eiii_Dehydrated=[2.94089000000000e-06,3.10867000000000e-06,3.20623000000000e-06,3.41954000000000e-06];
Eiii_Aqueous=[3.50963000000000e-06,3.81544000000000e-06,3.92842000000000e-06,4.07122000000000e-06];
Eii_Aqueous=[2.96221000000000e-07,8.36434000000000e-07,9.80373000000000e-07,1.08271000000000e-06];
Ei_Aqueous=[4.62604000000000e-07,1.11390000000000e-06,1.29113000000000e-06,1.37775000000000e-06];

% Final current reading at  600 seconds for Repeat Experiments
REP_Ei_Dehydrated = [5.343900000000000e-05, 5.832570000000000e-05, 6.017160000000000e-05, 6.112370000000001e-05];
REP_Eii_Dehydrated = [7.219590000000000e-06, 7.962200000000000e-06, 8.482480000000000e-06, 8.710950000000000e-06];
REP_Eiii_Dehydrated = [4.500790000000000e-06, 4.487599999999999e-06, 4.669160000000000e-06, 4.786699999999999e-06];
REP_Eiii_Aqueous = [5.506150000000000e-06, 5.750969999999999e-06, 5.856800000000000e-06, 6.025120000000000e-06];
REP_Eii_Aqueous = [3.830440000000000e-06, 7.029729999999999e-06, 7.566440000000000e-06, 7.869250000000000e-06];
REP_Ei_Aqueous = [3.992510000000000e-05, 5.491080000000001e-05, 5.715020000000001e-05, 5.915350000000001e-05];


% Using the current repsonse to the Buffer and 1uM analyte to calculate Sensitivity values
SensiEi_Dehydrated=(power(( Ei_Dehydrated(4)/ Ei_Dehydrated(1) ), (1/3))-1)*100;
SensiEii_Dehydrated=(power(( Eii_Dehydrated(4)/ Eii_Dehydrated(1) ), (1/3))-1)*100;
SensiEiii_Dehydrated=(power(( Eiii_Dehydrated(4)/ Eiii_Dehydrated(1) ), (1/3))-1)*100;
SensiEi_Aqueous=(power(( EiWet(4)/ EiWet(1) ), (1/3))-1)*100;
SensiEii_Aqueous=(power(( EiiWet(4)/ EiiWet(1) ), (1/3))-1)*100;
SensiEiii_Aqueous=(power(( Eiii_Aqueous(4)/ Eiii_Aqueous(1) ), (1/3))-1)*100;

% Using the current repsonse to the Buffer and 1uM analyte to calculate Sensitivity values for ghd  repeat experiments
REP_SensiEi_Dehydrated=(power(( REP_Ei_Dehydrated(4)/ REP_Ei_Dehydrated(1) ), (1/3))-1)*100;
REP_SensiEii_Dehydrated=(power(( REP_Eii_Dehydrated(4)/ REP_Eii_Dehydrated(1) ), (1/3))-1)*100;
REP_SensiEiii_Dehydrated=(power(( REP_Eiii_Dehydrated(4)/ REP_Eiii_Dehydrated(1) ), (1/3))-1)*100;
REP_SensiEi_Aqueous=(power(( REP_Ei_Aqueous(4)/ REP_Ei_Aqueous(1) ), (1/3))-1)*100;
REP_SensiEii_Aqueous=(power(( REP_Eii_Aqueous(4)/ REP_Eii_Aqueous(1) ), (1/3))-1)*100;
REP_SensiEiii_Aqueous=(power(( REP_Eiii_Aqueous(4)/ REP_Eiii_Aqueous(1) ), (1/3))-1)*100;
```

Figure F.1: This is code used to calculate Sensitivity.

Bibliography

[1] Brian D Harfe. "MicroRNAs in vertebrate development". In: *Current Opinion in Genetics & Development* 15.4 (2005). Pattern formation and developmental mechanisms, pp. 410–415. ISSN: 0959-437X. DOI: https://doi.org/10.1016/j.gde.2005.06.012. URL: http://www.sciencedirect.com/science/article/pii/S0959437X05000985.

[2] George Adrian Calin et al. "MicroRNA profiling reveals distinct signatures in B cell chronic lymphocytic leukemias". In: *Proceedings of the National Academy of Sciences* 101.32 (2004), pp. 11755–11760. ISSN: 0027-8424. DOI: 10.1073/pnas.0404432101. URL: https://www.pnas.org/content/101/32/11755.

[3] Marilena V. Iorio et al. "MicroRNA Gene Expression Deregulation in Human Breast Cancer". In: *Cancer Research* 65.16 (2005), pp. 7065–7070. ISSN: 0008-5472. DOI: 10.1158/0008-5472.CAN-05-1783. URL: https://cancerres.aacrjournals.org/content/65/16/7065.

[4] S.A. Ciafrè et al. "Extensive modulation of a set of microRNAs in primary glioblastoma". In: *Biochemical and Biophysical Research Communications* 334.4 (2005), pp. 1351–1358. ISSN: 0006-291X. DOI: https://doi.org/10.1016/j.bbrc.2005.07.030. URL: http://www.sciencedirect.com/science/article/pii/S0006291X05014816.

[5] Y. Murakami et al. "Comprehensive analysis of microRNA expression patterns in hepatocellular carcinoma and non-tumorous tissues". In: *Oncogene* 25.17 (Apr. 2006), pp. 2537–2545. ISSN: 1476-5594. DOI: 10.1038/sj.onc.1209283. URL: https://doi.org/10.1038/sj.onc.1209283.

[6] Huiling He et al. "The role of microRNA genes in papillary thyroid carcinoma". In: *Proceedings of the National Academy of Sciences* 102.52 (2005), pp. 19075–19080. ISSN: 0027-8424. DOI: 10.1073/pnas.0509603102. URL: https://www.pnas.org/content/102/52/19075.

[7] Junichi Takamizawa et al. "Reduced Expression of the let-7 MicroRNAs in Human Lung Cancers in Association with Shortened Postoperative Survival". In: *Cancer Research* 64.11 (2004), pp. 3753–3756. ISSN: 0008-5472. DOI: 10.1158/0008-5472.CAN-04-0637. URL: https://cancerres.aacrjournals.org/content/64/11/3753.

[8] Michael Z. Michael et al. "Reduced Accumulation of Specific MicroRNAs in Colorectal Neoplasia11Note: Susan M. O' Connor and Nicholas G. van Holst Pellekaan contributed equally to this work." In: *Molecular Cancer Research* 1.12 (2003), pp. 882–891. ISSN: 1541-7786. URL: https://mcr.aacrjournals.org/content/1/12/882.

[9] Stefano Volinia et al. “A microRNA expression signature of human solid tumors defines cancer gene targets”. In: *Proceedings of the National Academy of Sciences* 103.7 (2006), pp. 2257–2261. ISSN: 0027-8424. DOI: 10.1073/pnas.0510565103. URL: https://www.pnas.org/content/103/7/2257.

[10] Wooseok Jung et al. “Point-of-care testing (POCT) diagnostic systems using microfluidic lab-on-a-chip technologies”. In: *Microelectronic Engineering* 132 (2015). Micro and Nanofabrication Breakthroughs for Electronics, MEMS and Life Sciences, pp. 46–57. ISSN: 0167-9317. DOI: https://doi.org/10.1016/j.mee.2014.09.024.

[11] Myriam Deveugele et al. “Consultation length in general practice: cross sectional study in six European countries”. In: *BMJ* 325.7362 (2002), p. 472. DOI: 10.1136/bmj.325.7362.472.

[12] Darlisha A. Williams et al. “Evaluation of Fingerstick Cryptococcal Antigen Lateral Flow Assay in HIV-Infected Persons: A Diagnostic Accuracy Study”. In: *Clinical Infectious Diseases* 61.3 (Apr. 2015), pp. 464–467. ISSN: 1058-4838. DOI: 10.1093/cid/civ263. URL: https://doi.org/10.1093/cid/civ263.

[13] Liqiang Liu et al. “Development and evaluation of a rapid lateral flow immunochromatographic strip assay for screening 19-nortestosterone”. In: *Biomedical Chromatography* 21.8 (2007), pp. 861–866. DOI: 10.1002/bmc.832. URL: https://onlinelibrary.wiley.com/doi/abs/10.1002/bmc.832.

[14] Vadim Krivitsky, Marina Zverzhinetsky, and Fernando Patolsky. “Antigen-Dissociation from Antibody-Modified Nanotransistor Sensor Arrays as a Direct Biomarker Detection Method in Unprocessed Biosamples”. In: *Nano Letters* 16.10 (2016), pp. 6272–6281. DOI: 10.1021/acs.nanolett.6b02584. URL: https://doi.org/10.1021/acs.nanolett.6b02584.

[15] A. F. Lotus, D. H. Reneker, and G. G. Chase. “Electrical, structural, and chemical properties of semiconducting metal oxide nanofiber yarns”. In: *Journal of Applied Physics* 103.2 (2008), p. 024910. DOI: 10.1063/1.2831362.

[16] A. Ohtomo, H. Koinuma, and M. Kawasaki. “Single crystalline ZnO films grown on lattice-matched ScAlMgO4(0001) substrates”. In: *Applied Physics Letters* 75.17 (1999), pp. 2635–2637. DOI: 10.1063/1.125102.

[17] Ü. Özgür, S.-J. Cho, and H. Morkoç. “A comprehensive review of ZnO materials and devices”. In: *Journal of Applied Physics* 98.4 (2005), p. 041301. DOI: 10.1063/1.1992666.

[18] J.D. Akrofi et al. “Multi-stack insulator to minimise threshold voltage drift in ZnO FET sensors operating in ionic solutions”. In: *Micro and Nano Engineering* (2020), p. 100066. ISSN: 2590-0072. DOI: https://doi.org/10.1016/j.mne.2020.100066. URL: http://www.sciencedirect.com/science/article/pii/S2590007220300216.

[19] O. Knopfmacher et al. “Nernst Limit in Dual-Gated Si-Nanowire FET Sensors”. In: *Nano Letters* 10.6 (2010). PMID: 20499926, pp. 2268–2274. DOI: 10.1021/nl100892y.

[20] T. Vo-Dinh and B. Cullum. “Biosensors and biochips: advances in biological and medical diagnostics”. In: *Fresenius’ Journal of Analytical Chemistry* 366.6 (2000), pp. 540–551. ISSN: 1432-1130. DOI: 10.1007/s002160051549. URL: https://doi.org/10.1007/s002160051549.

[21] Matti Kaisti. "Detection principles of biological and chemical FET sensors". In: *Biosensors and Bioelectronics* 98 (2017), pp. 437–448. ISSN: 0956-5663. DOI: https://doi.org/10.1016/j.bios.2017.07.010.

[22] Christine Campagnolo et al. "Real-Time, label-free monitoring of tumor antigen and serum antibody interactions". In: *Journal of biochemical and biophysical methods* 61.3 (Nov. 2004), pp. 283–298. ISSN: 0165-022X. DOI: 10.1016/j.jbbm.2004.05.006. URL: https://doi.org/10.1016/j.jbbm.2004.05.006.

[23] A Milford Ward, J W F Catto, and F C Hamdy. "Prostate specific antigen: biology, biochemistry and available commercial assays". In: *Annals of Clinical Biochemistry* 38.6 (2001), pp. 633–651. DOI: 10.1258/0004563011901055.

[24] Guanghua Wu et al. "Bioassay of prostate-specific antigen (PSA) using microcantilevers". In: *Nature Biotechnology* 19.9 (2001), pp. 856–860. ISSN: 1546-1696. DOI: 10.1038/nbt0901-856.

[25] J. L. Arlett, E. B. Myers, and M. L. Roukes. "Comparative advantages of mechanical biosensors". In: *Nature Nanotechnology* 6 (Mar. 2011), p. 203.

[26] Fernando Patolsky, Gengfeng Zheng, and Charles M. Lieber. "Nanowire-Based Biosensors". In: *Analytical Chemistry* 78.13 (2006), pp. 4260–4269. DOI: 10.1021/ac069419j.

[27] Oscar Gutierrez-Sanz et al. "Direct, Label-Free, and Rapid Transistor-Based Immunodetection in Whole Serum". In: *ACS Sensors* 2.9 (2017), pp. 1278–1286. DOI: 10.1021/acssensors.7b00187.

[28] D. Cahen, R. Naaman, and Z. Vager. "The Cooperative Molecular Field Effect". In: *Advanced Functional Materials* 15.10 (2005), pp. 1571–1578. DOI: 10.1002/adfm.200500187.

[29] P. Bergveld, J. Wiersma, and H. Meertens. "Extracellular Potential Recordings by Means of a Field Effect Transistor Without Gate Metal, Called OSFET". In: *IEEE Transactions on Biomedical Engineering* BME-23.2 (Mar. 1976), pp. 136–144. ISSN: 0018-9294. DOI: 10.1109/TBME.1976.324574.

[30] Fernando Patolsky et al. "Electrical detection of single viruses". In: *Proceedings of the National Academy of Sciences* 101.39 (2004), pp. 14017–14022. ISSN: 0027-8424. DOI: 10.1073/pnas.0406159101. URL: https://www.pnas.org/content/101/39/14017.

[31] Jordi Riu, Alicia Maroto, and F. Xavier Rius. "Nanosensors in environmental analysis". In: *Talanta* 69.2 (2006). 1st Swift-WFD workshop on validation of Robustness of sensors and bioassays for Screening Pollutants, pp. 288–301. ISSN: 0039-9140. DOI: https://doi.org/10.1016/j.talanta.2005.09.045. URL: http://www.sciencedirect.com/science/article/pii/S0039914005006570.

[32] Pooja Arora et al. "Biosensors as innovative tools for the detection of food borne pathogens". In: *Biosensors and Bioelectronics* 28.1 (2011), pp. 1–12. ISSN: 0956-5663. DOI: https://doi.org/10.1016/j.bios.2011.06.002. URL: http://www.sciencedirect.com/science/article/pii/S0956566311003502.

[33] Wayne U. Wang et al. “Label free detection of small molecule protein interactions by using nanowire nanosensors”. In: *Proceedings of the National Academy of Sciences* 102.9 (2005), pp. 3208–3212. ISSN: 0027-8424. DOI: 10.1073/pnas.0406368102.

[34] Martin Ebert. “A novel low temperature fabrication approach of multichannel zinc oxide nanowire field effect transistors for biosensing applications”. PhD thesis. University of Southampton, Aug. 2019. URL: https://eprints.soton.ac.uk/438102/.

[35] Michael Taeyoung Hwang et al. “Ultrasensitive detection of nucleic acids using deformed graphene channel field effect biosensors”. In: *Nature Communications* 11.1 (Mar. 2020), p. 1543. ISSN: 2041-1723. DOI: 10.1038/s41467-020-15330-9. URL: https://doi.org/10.1038/s41467-020-15330-9.

[36] Wen-Pin Hu et al. “Synergetic improvements of sensitivity and specificity of nanowire field effect transistor gene chip by designing neutralized DNA as probe”. In: *Scientific Reports* 8.1 (Aug. 2018), p. 12598. ISSN: 2045-2322. DOI: 10.1038/s41598-018-30996-4. URL: https://doi.org/10.1038/s41598-018-30996-4.

[37] Na Lu et al. “Ultra-sensitive nucleic acids detection with electrical nanosensors based on CMOS-compatible silicon nanowire field-effect transistors”. In: *Methods* 63.3 (2013). Biosensor Technologies, pp. 212–218. ISSN: 1046-2023. DOI: https://doi.org/10.1016/j.ymeth.2013.07.012.

[38] Samaneh Mirsian et al. “A new method for selective functionalization of silicon nanowire sensors and Bayesian inversion for its parameters”. In: *Biosensors and Bioelectronics* 142 (2019), p. 111527. ISSN: 0956-5663. DOI: https://doi.org/10.1016/j.bios.2019.111527. URL: https://www.sciencedirect.com/science/article/pii/S0956566319306062.

[39] Dong-Sheng Su et al. “Disease antigens detection by silicon nanowires with the efficiency optimization of their antibodies on a chip”. In: *Biosensors and Bioelectronics* 141 (2019), p. 111209. ISSN: 0956-5663. DOI: https://doi.org/10.1016/j.bios.2019.03.042. URL: https://www.sciencedirect.com/science/article/pii/S0956566319302477.

[40] Shenhui Ma et al. “Direct label-free protein detection in high ionic strength solution and human plasma using dual-gate nanoribbon-based ion-sensitive field-effect transistor biosensor”. In: *Biosensors and Bioelectronics* 117 (2018), pp. 276–282. ISSN: 0956-5663. DOI: https://doi.org/10.1016/j.bios.2018.05.061.

[41] Mihee Uhm et al. “Ultrasensitive Electrical Detection of Hemagglutinin for Point-of-Care Detection of Influenza Virus Based on a CMP-NANA Probe and Top-Down Processed Silicon Nanowire Field-Effect Transistors”. In: *Sensors (Basel, Switzerland)* 19.20 (Sept. 2019). s19204502[PII], p. 4502. ISSN: 1424-8220. DOI: 10.3390/s19204502. URL: https://doi.org/10.3390/s19204502.

[42] Jong-in Hahm and Charles M. Lieber. “Direct Ultrasensitive Electrical Detection of DNA and DNA Sequence Variations Using Nanowire Nanosensors”. In: *Nano Letters* 4.1 (2004), pp. 51–54. DOI: 10.1021/nl034853b.

[43] Gengfeng Zheng et al. "Multiplexed electrical detection of cancer markers with nanowire sensor arrays". In: *Nature Biotechnology* 23.10 (2005), pp. 1294–1301. ISSN: 1546-1696. DOI: 10.1038/nbt1138.

[44] NW Kim et al. "Specific association of human telomerase activity with immortal cells and cancer". In: *Science* 266.5193 (1994), pp. 2011–2015. ISSN: 0036-8075. DOI: 10.1126/science.7605428.

[45] Joseph Becker. "Signal transduction inhibitors–a work in progress". In: *Nature Biotechnology* 22.1 (2004), pp. 15–18. ISSN: 1546-1696. DOI: 10.1038/nbt0104-15.

[46] Yu Zhang et al. "Electrochemical Stability Investigations and Drug Toxicity Tests of Electrolyte-Gated Organic Field-Effect Transistors". In: *ACS Applied Materials & Interfaces* 12.50 (2020). PMID: 33327057, pp. 56216–56221. DOI: 10.1021/acsami.0c15024. URL: https://doi.org/10.1021/acsami.0c15024.

[47] A. Susloparova et al. "Impedance spectroscopy with field-effect transistor arrays for the analysis of anti-cancer drug action on individual cells". In: *Biosensors and Bioelectronics* 40.1 (2013). Selected Papers from the World Congress on Biosensors, pp. 50–56. ISSN: 0956-5663. DOI: https://doi.org/10.1016/j.bios.2012.06.006. URL: https://www.sciencedirect.com/science/article/pii/S095656631200365X.

[48] Shu-Yi Tsai et al. "Rapid Drug-Screening Platform Using Field-Effect Transistor-Based Biosensors: A Study of Extracellular Drug Effects on Transmembrane Potentials". In: *Analytical Chemistry* 94.6 (2022). PMID: 34919373, pp. 2679–2685. DOI: 10.1021/acs.analchem.1c03402. URL: https://doi.org/10.1021/acs.analchem.1c03402.

[49] Duy Phu Tran et al. "CMOS Compatible Silicon Nanowire Field Effect Transistor Biosensor". In: *Materials* 11.5 (2018). ISSN: 1996-1944. DOI: 10.3390/ma11050785.

[50] Duy P. Tran, Andreas Offenhäusser, and Benjamin Thierry. "Toward Intraoperative Detection of Disseminated Tumor Cells in Lymph Nodes with Silicon Nanowire Field Effect Transistors". In: *ACS Nano* 10.2 (2016), pp. 2357–2364. DOI: 10.1021/acsnano.5b07136.

[51] Richard M. Graybill and Ryan C. Bailey. "Emerging Biosensing Approaches for microRNA Analysis". In: *Analytical Chemistry* 88.1 (2016), pp. 431–450. DOI: 10.1021/acs.analchem.5b04679.

[52] Jun Lu, H. Robert Horvitz, and Todd R. Golub. "MicroRNA expression profiles classify human cancers". In: *Nature* 435.7043 (2005), pp. 834–838. ISSN: 1476-4687. DOI: 10.1038/nature03702.

[53] M. Im et al. "Development of a Point-of-Care Testing Platform With a Nanogap-Embedded Separated Double-Gate Field Effect Transistor Array and Its Readout System for Detection of Avian Influenza". In: *IEEE Sensors Journal* 11.2 (Feb. 2011), pp. 351–360. ISSN: 1530-437X. DOI: 10.1109/JSEN.2010.2062502.

[54] W. H. Lee et al. "Characterization and Capacitive Modeling of Target Concentration-Dependent Subthreshold Swing in Silicon Nanoribbon Biosensors". In: *IEEE Electron Device Letters* 35.5 (May 2014), pp. 587–589. ISSN: 0741-3106. DOI: 10.1109/LED.2014.2312196.

[55] Hyungsoon Im et al. "A dielectric-modulated field-effect transistor for biosensing". In: *Nature Nanotechnology* 2 (June 2007), p. 430.

[56] Xuexin Duan et al. "Quantification of the affinities and kinetics of protein interactions using silicon nanowire biosensors". In: *Nature Nanotechnology* 7 (May 2012). Article, p. 401.

[57] Gengfeng Zheng, Xuan P. A. Gao, and Charles M. Lieber. "Frequency Domain Detection of Biomolecules Using Silicon Nanowire Biosensors". In: *Nano Letters* 10.8 (2010), pp. 3179–3183. DOI: 10.1021/nl1020975.

[58] Hao Heng Liu, Tzung Han Lin, and Jeng-Tzong Sheu. "Enhancement of detection by selective modification of silicon nanobelt field-effect transistors via localized Joule heating". In: *Sensors and Actuators B: Chemical* 192 (2014), pp. 111–116. ISSN: 0925-4005. DOI: https://doi.org/10.1016/j.snb.2013.10.102.

[59] Taiuk Rim et al. "Investigation of the electrical stability of Si-nanowire biologically sensitive field-effect transistors with embedded Ag/AgCl pseudo reference electrode". In: *RSC Adv.* 3 (21 2013), pp. 7963–7969. DOI: 10.1039/C3RA40768C.

[60] Junchi Mei et al. "Molybdenum disulfide field-effect transistor biosensor for ultrasensitive detection of DNA by employing morpholino as probe". In: *Biosensors and Bioelectronics* 110 (2018), pp. 71–77. ISSN: 0956-5663. DOI: https://doi.org/10.1016/j.bios.2018.03.043.

[61] Mohsen Shariati. "The field effect transistor DNA biosensor based on ITO nanowires in label-free hepatitis B virus detecting compatible with CMOS technology". In: *Biosensors and Bioelectronics* 105 (2018), pp. 58–64. ISSN: 0956-5663. DOI: https://doi.org/10.1016/j.bios.2018.01.022. URL: http://www.sciencedirect.com/science/article/pii/S0956566318300289.

[62] N Aroonyadet et al. "Top-down and sensitive indium oxide nanoribbon field effect transistor biosensor chips integrated with on-chip gate electrodes toward point of care applications". In: *Nanotechnology* 29.40 (July 2018), p. 405505. DOI: 10.1088/1361-6528/aad435.

[63] Zhaoli Gao et al. "Detection of Sub-fM DNA with Target Recycling and Self-Assembly Amplification on Graphene Field-Effect Biosensors". In: *Nano Letters* 18.6 (2018), pp. 3509–3515. DOI: 10.1021/acs.nanolett.8b00572.

[64] Pavel Ivanoff Reyes et al. "ZnO thin film transistor immunosensor with high sensitivity and selectivity". In: *Applied Physics Letters* 98.17 (2011), p. 173702. DOI: 10.1063/1.3582555.

[65] Cornelis P. Balde et al. "The Global E-waste Monitor 2017: Quantities, Flows and Resources". In: (2017). URL: http://collections.unu.edu/eserv/UNU:6341/Global-E-waste_Monitor_2017__electronic_single_pages_.pdf.

[66] Simon M. Sze and Ming-Kwei Lee. *Semiconductor Devices: Physics and Technology*. 3rd ed. John Wiley & Sons Inc., 2012. ISBN: 978-0-470-91407-6.

[67] Yuan Taur and Tak H. Ning. *Fundamentals of Modern VLSI Devices*. 2nd. New York, NY, USA: Cambridge University Press, 2009. ISBN: 0521832942.

[68] Benjamin M. Lowe, Chris-Kriton Skylaris, and Nicolas G. Green. "Field-effect sensors: From pH sensing to biosensing: sensitivity enhancement using streptavidin-biotin as a model system". In: *Analyst* 142 (22 2017), pp. 4173–4200. DOI: 10.1039/C7AN00455A. URL: http://dx.doi.org/10.1039/C7AN00455A.

[69] Sami Franssila. "Silicon". In: *Introduction to Microfabrication*. John Wiley & Sons, Ltd, 2010. Chap. 4, pp. 35–46. ISBN: 9781119990413. DOI: https://doi.org/10.1002/9781119990413.ch4. URL: https://onlinelibrary.wiley.com/doi/abs/10.1002/9781119990413.ch4.

[70] D. C. Look, J. W. Hemsky, and J. R. Sizelove. "Residual Native Shallow Donor in ZnO". In: *Phys. Rev. Lett.* 82 (12 Mar. 1999), pp. 2552–2555. DOI: 10.1103/PhysRevLett.82.2552.

[71] Chris G. Van de Walle. "Hydrogen as a Cause of Doping in Zinc Oxide". In: *Phys. Rev. Lett.* 85 (5 July 2000), pp. 1012–1015. DOI: 10.1103/PhysRevLett.85.1012.

[72] Sami Franssila. "Diffusion". In: *Introduction to Microfabrication*. John Wiley & Sons, Ltd, 2010, pp. 165–172. ISBN: 9781119990413. DOI: https://doi.org/10.1002/9781119990413.ch14. URL: https://onlinelibrary.wiley.com/doi/abs/10.1002/9781119990413.ch14.

[73] M Ebert, M R R de Planque, and H M H Chong. "Multichannel ZnO nanowire field effect transistors by lift-off process". In: *Nanotechnology* 29.41 (2018), p. 415302. DOI: 10.1088/1361-6528/aad4c5. URL: https://doi.org/10.1088%2F1361-6528%2Faad4c5.

[74] H. Liu et al. "Aluminum-Doped Zinc Oxide Transparent Electrode Prepared by Atomic Layer Deposition for Organic Light Emitting Devices". In: *IEEE Transactions on Nanotechnology* 16.4 (July 2017), pp. 634–638. ISSN: 1536-125X. DOI: 10.1109/TNANO.2017.2700408.

[75] Robertson, J. "High dielectric constant oxides". In: *Eur. Phys. J. Appl. Phys.* 28.3 (2004), pp. 265–291. DOI: 10.1051/epjap:2004206. URL: https://doi.org/10.1051/epjap:2004206.

[76] Bobby Reddy, Muhammad A. Alam, and Rashid Bashir. "High-k dielectric Al2O3 nanowire and nanoplate field effect sensors for improved pH sensing". In: *Biomedical Microdevices* 13.2 (Apr. 2011), pp. 335–344. ISSN: 1572-8781. DOI: 10.1007/s10544-010-9497-z.

[77] Tseng-Fu Lu, Chi-Fong Ai, and Chao-Sung Lai. "Non-ideal effects improvement of SF6 plasma treated hafnium oxide film based on electrolyte-insulator-semiconductor structure for pH-sensor application". In: *Microelectronics Reliability* 50.5 (2010). 2009 International Electron Devices and Materials Symposium (IEDMS), pp. 742–746. ISSN: 0026-2714. DOI: https://doi.org/10.1016/j.microrel.2010.01.029.

[78] M.J. Schöning, Yu.G. Vlasov, and H. Lüth. "Can pulsed laser deposition serve as an advanced technique in fabricating chemical sensors?" In: *Sensors and Actuators B: Chemical* 78.1 (2001). Selected Papers from Eurosensors XIV, pp. 273–278. ISSN: 0925-4005. DOI: https://doi.org/10.1016/S0925-4005(01)00825-5.

[79] Shih-Hsiang Shen et al. "An enhancement of high-k/oxide stacked dielectric structure for silicon-based multi-nanowire biosensor in cardiac troponin I detection". In: *Sensors and Actuators B: Chemical* 218 (2015), pp. 303–309. ISSN: 0925-4005. DOI: https://doi.org/10.1016/j.snb.2015.05.002.

[80] Eric Stern et al. “Label-free immunodetection with CMOS-compatible semiconducting nanowires”. In: *Nature* 445 (Feb. 2007), p. 519. URL: https://doi.org/10.1038/nature05498.

[81] Niklas Elfström, Amelie Eriksson Karlström, and Jan Linnros. “Surface Charge Sensitivity of Silicon Nanowires: Size Dependence”. In: *Nano Letters* 7.9 (2007), pp. 2608–2612. DOI: 10.1021/nl0709017.

[82] Niklas Elfström, Amelie Eriksson Karlström, and Jan Linnros. “Silicon Nanoribbons for Electrical Detection of Biomolecules”. In: *Nano Letters* 8.3 (2008), pp. 945–949. DOI: 10.1021/nl080094r.

[83] P. R. Nair and M. A. Alam. “Performance limits of nanobiosensors”. In: *Applied Physics Letters* 88.23 (2006), p. 233120. DOI: 10.1063/1.2211310.

[84] Larry Senesac and Thomas G. Thundat. “Nanosensors for trace explosive detection”. In: *Materials Today* 11.3 (2008), pp. 28–36. ISSN: 1369-7021. DOI: https://doi.org/10.1016/S1369-7021(08)70017-8. URL: http://www.sciencedirect.com/science/article/pii/S1369702108700178.

[85] P. Bergveld. “Development of an Ion-Sensitive Solid-State Device for Neurophysiological Measurements”. In: *IEEE Transactions on Biomedical Engineering* BME-17.1 (1970), pp. 70–71.

[86] P. Bergveld. “Development, Operation, and Application of the Ion-Sensitive Field-Effect Transistor as a Tool for Electrophysiology”. In: *IEEE Transactions on Biomedical Engineering* BME-19.5 (1972), pp. 342–351.

[87] Geert A. L. Besselink and Piet Bergveld. “ISFET affinity sensor”. In: *Affinity Biosensors: Techniques and Protocols*. Ed. by Kim R. Rogers and Ashok Mulchandani. Totowa, NJ: Humana Press, 1998, pp. 173–185. ISBN: 978-1-59259-485-6. DOI: 10.1385/0-89603-539-5:173.

[88] Jonghyun Go, Pradeep R. Nair, and Muhammad A. Alam. “Theory of signal and noise in double-gated nanoscale electronic pH sensors”. In: *Journal of Applied Physics* 112.3 (2012), p. 034516. DOI: 10.1063/1.4737604. URL: https://doi.org/10.1063/1.4737604.

[89] P. Bergveld. “Thirty years of ISFETOLOGY: What happened in the past 30 years and what may happen in the next 30 years”. In: *Sensors and Actuators B: Chemical* 88.1 (2003), pp. 1–20. ISSN: 0925-4005. DOI: https://doi.org/10.1016/S0925-4005(02)00301-5. URL: http://www.sciencedirect.com/science/article/pii/S0925400502003015.

[90] B. M. Lowe et al. “Dynamic behaviour of the silica-water-bio electrical double layer in the presence of a divalent electrolyte”. In: *Phys. Chem. Chem. Phys.* 19 (4 2017), pp. 2687–2701. DOI: 10.1039/C6CP04101A. URL: http://dx.doi.org/10.1039/C6CP04101A.

[91] David E. Yates, Samuel Levine, and Thomas W. Healy. “Site-binding model of the electrical double layer at the oxide/water interface”. In: *J. Chem. Soc., Faraday Trans. 1* 70 (0 1974), pp. 1807–1818. DOI: 10.1039/F19747001807. URL: http://dx.doi.org/10.1039/F19747001807.

[92] Michael J. Schöning and Arshak Poghossian. “Recent advances in biologically sensitive field-effect transistors (BioFETs)”. In: *Analyst* 127 (9 2002), pp. 1137–1151. DOI: 10.1039/B204444G. URL: http://dx.doi.org/10.1039/B204444G.

[93] R.E.G. [van Hal], J.C.T. Eijkel, and P. Bergveld. "A general model to describe the electrostatic potential at electrolyte oxide interfaces". In: *Advances in Colloid and Interface Science* 69.1 (1996), pp. 31–62. ISSN: 0001-8686. DOI: https://doi.org/10.1016/S0001-8686(96)00307-7. URL: http://www.sciencedirect.com/science/article/pii/S0001868696003077.

[94] B. M. Lowe et al. "Molecular dynamics simulation of potentiometric sensor response: the effect of biomolecules, surface morphology and surface charge". In: *Nanoscale* 10 (18 2018), pp. 8650–8666. DOI: 10.1039/C8NR00776D. URL: http://dx.doi.org/10.1039/C8NR00776D.

[95] Deblina Sarkar et al. "MoS2 Field-Effect Transistor for Next-Generation Label-Free Biosensors". In: *ACS Nano* 8.4 (2014). PMID: 24588742, pp. 3992–4003. DOI: 10.1021/nn5009148. URL: https://doi.org/10.1021/nn5009148.

[96] K Sun et al. "Effect of subthreshold slope on the sensitivity of nanoribbon sensors". In: *Nanotechnology* 27.28 (June 2016), p. 285501. DOI: 10.1088/0957-4484/27/28/285501. URL: https://doi.org/10.1088%2F0957-4484%2F27%2F28%2F285501.

[97] I Zeimpekis et al. "Dual-gate polysilicon nanoribbon biosensors enable high sensitivity detection of proteins". In: *Nanotechnology* 27.16 (2016), p. 165502. DOI: 10.1088/0957-4484/27/16/165502.

[98] Sungho Kim et al. "Silicon nanowire ion sensitive field effect transistor with integrated Ag/AgCl electrode: pH sensing and noise characteristics". In: *Analyst* 136 (23 2011), pp. 5012–5016. DOI: 10.1039/C1AN15568G. URL: http://dx.doi.org/10.1039/C1AN15568G.

[99] Xuan P. A. Gao, Gengfeng Zheng, and Charles M. Lieber. "Subthreshold Regime has the Optimal Sensitivity for Nanowire FET Biosensors". In: *Nano Letters* 10.2 (2010). PMID: 19908823, pp. 547–552. DOI: 10.1021/nl9034219.

[100] Sufi Zafar et al. "Optimization of pH sensing using silicon nanowire field effect transistors with HfO2as the sensing surface". In: *Nanotechnology* 22.40 (Sept. 2011), p. 405501. DOI: 10.1088/0957-4484/22/40/405501. URL: https://doi.org/10.1088%2F0957-4484%2F22%2F40%2F405501.

[101] S. Rigante et al. "Finfet With Fully Ph-Responsive Hfo2 As Highly Stable Biochemical Sensor". In: *2014 Ieee 27Th International Conference On Micro Electro Mechanical Systems (Mems)* (2014), pp. 4. 1063–1066. URL: http://infoscience.epfl.ch/record/208698.

[102] Songyue Chen et al. "Al2O3/Silicon NanoISFET with Near Ideal Nernstian Response". In: *Nano Letters* 11.6 (2011). PMID: 21526845, pp. 2334–2341. DOI: 10.1021/nl200623n. URL: https://doi.org/10.1021/nl200623n.

[103] A. Tarasov et al. "True Reference Nanosensor Realized with Silicon Nanowires". In: *Langmuir* 28.25 (2012). PMID: 22631046, pp. 9899–9905. DOI: 10.1021/la301555r. URL: https://doi.org/10.1021/la301555r.

[104] Fateme S. Emami et al. "Force Field and a Surface Model Database for Silica to Simulate Interfacial Properties in Atomic Resolution". In: *Chemistry of Materials* 26.8 (2014), pp. 2647–2658. DOI: 10.1021/cm500365c. URL: https://doi.org/10.1021/cm500365c.

[105] Fateme S. Emami et al. “Correction to Force Field and a Surface Model Database for Silica to Simulate Interfacial Properties in Atomic Resolution”. In: *Chemistry of Materials* 28.1 (2016), pp. 406–407. DOI: 10.1021/acs.chemmater.5b04760. URL: https://doi.org/10.1021/acs.chemmater.5b04760.

[106] Toshiya Sakata et al. “Ion Sensitive Transparent-Gate Transistor for Visible Cell Sensing”. In: *Analytical Chemistry* 89.7 (2017). PMID: 28298088, pp. 3901–3908. DOI: 10.1021/acs.analchem.6b02246. URL: https://doi.org/10.1021/acs.analchem.6b02246.

[107] Yi Cui et al. “Nanowire Nanosensors for Highly Sensitive and Selective Detection of Biological and Chemical Species”. In: *Science* 293.5533 (2001), pp. 1289–1292. ISSN: 0036-8075. DOI: 10.1126/science.1062711.

[108] Jonghyun Go, Pradeep R. Nair, and Muhammad A. Alam. “Theory of signal and noise in double-gated nanoscale electronic pH sensors”. In: *Journal of Applied Physics* 112.3 (2012), p. 034516. DOI: 10.1063/1.4737604.

[109] Daniel R. Thévenot et al. “Electrochemical biosensors: recommended definitions and classification1International Union of Pure and Applied Chemistry: Physical Chemistry Division, Commission I.7 (Biophysical Chemistry); Analytical Chemistry Division, Commission V.5 (Electroanalytical Chemistry).1”. In: *Biosensors and Bioelectronics* 16.1 (2001), pp. 121–131. ISSN: 0956-5663. DOI: https://doi.org/10.1016/S0956-5663(01)00115-4. URL: https://www.sciencedirect.com/science/article/pii/S0956566301001154.

[110] Vivek Pachauri and Sven Ingebrandt. “Biologically sensitive field-effect transistors: from ISFETs to NanoFETs”. In: 60.1 (2016), pp. 81–90. ISSN: 0071-1365. DOI: 10.1042/EBC20150009.

[111] A. Poghossian et al. “Possibilities and limitations of label-free detection of DNA hybridization with field-effect-based devices”. In: *Sensors and Actuators B: Chemical* 111-112 (2005), pp. 470–480. ISSN: 0925-4005. DOI: https://doi.org/10.1016/j.snb.2005.03.083.

[112] Roey Elnathan, Raisa Kantaev, and Fernando Patolsky. “Biorecognition Layer Engineering: Overcoming Screening Limitations of Nanowire-Based FET Devices”. In: *Nano Letters* 12.10 (2012), pp. 5245–5254. DOI: 10.1021/nl302434w.

[113] Mo-Yuan Shen, Bor-Ran Li, and Yaw-Kuen Li. “Silicon nanowire field-effect-transistor based biosensors: From sensitive to ultra-sensitive”. In: *Biosensors and Bioelectronics* 60 (2014), pp. 101–111. ISSN: 0956-5663. DOI: https://doi.org/10.1016/j.bios.2014.03.057.

[114] Guo-Jun Zhang et al. “Label-free direct detection of MiRNAs with silicon nanowire biosensors”. In: *Biosensors and Bioelectronics* 24.8 (2009), pp. 2504–2508. ISSN: 0956-5663. DOI: https://doi.org/10.1016/j.bios.2008.12.035.

[115] Benjamin Mark Lowe. “Interfacial physics of field-effect biosensors”. PhD thesis. University of Southampton, 2016.

[116] Noémie Lloret et al. “Effects of buffer composition and dilution on nanowire field-effect biosensors”. In: *Nanotechnology* 24.3 (Dec. 2012), p. 035501. DOI: 10.1088/0957-4484/24/3/035501. URL: https://doi.org/10.1088%2F0957-4484%2F24%2F3%2F035501.

[117] Alexey Tarasov, Michel Calame, and Christian Schönenberger. "Understanding the Electrolyte Background for Biochemical Sensing with Ion-Sensitive Field-Effect Transistors". In: *ACS Nano* 6.10 (2012). PMID: 23016890, pp. 9291–9298. DOI: 10.1021/nn303795r.

[118] Yuki Maekawa, Yasushi Shibuta, and Toshiya Sakata. "Distinctive Potential Behavior at the Oxidized Surface of a Semiconductor Device in a Concentrated Aqueous Salt Solution". In: *ChemElectroChem* 1.9 (2014), pp. 1516–1524. DOI: 10.1002/celc.201402069.

[119] Eric Stern et al. "Importance of the Debye Screening Length on Nanowire Field Effect Transistor Sensors". In: *Nano Letters* 7.11 (2007), pp. 3405–3409. DOI: 10.1021/nl071792z.

[120] Chan Woo Park et al. "Analysis of configuration of surface-immobilized proteins by Si nanochannel field effect transistor biosensor". In: *Sensors and Actuators B: Chemical* 154.2 (2011). EUROSENSORS XXIII, pp. 164–168. ISSN: 0925-4005. DOI: https://doi.org/10.1016/j.snb.2009.11.056.

[121] Vadim Krivitsky, Marina Zverzhinetsky, and Fernando Patolsky. "Antigen-Dissociation from Antibody-Modified Nanotransistor Sensor Arrays as a Direct Biomarker Detection Method in Unprocessed Biosamples". In: *Nano Letters* 16.10 (2016), pp. 6272–6281. DOI: 10.1021/acs.nanolett.6b02584.

[122] Todd M. Squires, Robert J. Messinger, and Scott R. Manalis. "Making it stick: convection, reaction and diffusion in surface-based biosensors". In: *Nature Biotechnology* 26 (Apr. 2008), p. 417. URL: https://doi.org/10.1038/nbt1388.

[123] Luc Bousse and Piet Bergveld. "The role of buried OH sites in the response mechanism of inorganic-gate pH-sensitive ISFETs". In: *Sensors and Actuators* 6.1 (1984), pp. 65–78. ISSN: 0250-6874. DOI: doi.org/10.1016/0250-6874(84)80028-1.

[124] A. Hartstein and D. R. Young. "Identification of electron traps in thermal silicon dioxide films". In: *Applied Physics Letters* 38.8 (1981), pp. 631–633. DOI: 10.1063/1.92459. URL: https://doi.org/10.1063/1.92459.

[125] Shahriar Jamasb, Scott Collins, and Rosemary L. Smith. "A physical model for drift in pH ISFETs". In: *Sensors and Actuators B: Chemical* 49.1 (1998), pp. 146–155. ISSN: 0925-4005. DOI: doi.org/10.1016/S0925-4005(98)00040-9.

[126] Tung-Ming Pan, Chao-Wen Lin, and Min-Hsien Wu. "Development of high-K HoTiO3 sensing membrane for pH detection and glucose biosensing". In: *Sensors and Actuators B: Chemical* 144.1 (2010), pp. 139–145. ISSN: 0925-4005. DOI: doi.org/10.1016/j.snb.2009.10.049.

[127] Tung-Ming Pan, Min-Hsien Wu, and Chao-Sung Lai. "Study of high-k Er2O3 thin layers as ISFET sensitive insulator surface for pH detection". In: *Sensors and Actuators B: Chemical* 138.2 (2009), pp. 619–624. ISSN: 0925-4005. DOI: doi.org/10.1016/j.snb.2009.01.051.

[128] Julien Beynet, Yong-Min Yoo, and Mireille Maenhoudt. "Low temperature plasma-enhanced ALD enables cost-effective spacer defined double patterning (SDDP)". In: *Lithography Asia 2009*. Ed. by Alek C. Chen et al. Vol. 7520. International Society for Optics and Photonics. SPIE, 2009, pp. 489–495. DOI: 10.1117/12.836979. URL: https://doi.org/10.1117/12.836979.

[129] Yuri L. Bunimovich et al. "Quantitative Real-Time Measurements of DNA Hybridization with Alkylated Nonoxidized Silicon Nanowires in Electrolyte Solution". In: *Journal of the American Chemical Society* 128.50 (2006), pp. 16323–16331. DOI: 10.1021/ja065923u.

[130] Ayako Oyane et al. "Preparation and assessment of revised simulated body fluids". In: *Journal of Biomedical Materials Research Part A* 65A.2 (2003), pp. 188–195. DOI: 10.1002/jbm.a.10482. URL: https://onlinelibrary.wiley.com/doi/abs/10.1002/jbm.a.10482.

[131] Mario Acunzo et al. "MicroRNA and cancer – A brief overview". In: *Advances in Biological Regulation* 57 (2015). 55th Symposium Issue, pp. 1–9. ISSN: 2212-4926. DOI: https://doi.org/10.1016/j.jbior.2014.09.013. URL: https://www.sciencedirect.com/science/article/pii/S2212492614000529.

[132] Yoontae Lee et al. "MicroRNA genes are transcribed by RNA polymerase II". In: *The EMBO Journal* 23.20 (2004), pp. 4051–4060. DOI: https://doi.org/10.1038/sj.emboj.7600385. URL: https://www.embopress.org/doi/abs/10.1038/sj.emboj.7600385.

[133] Jinju Han et al. "The Drosha-DGCR8 complex in primary microRNA processing". In: *Genes and Development* 18 (2004), pp. 3016–3027. ISSN: 0962-8924. DOI: doi:10.1101/gad.1262504.

[134] V.Narry Kim. "MicroRNA precursors in motion: exportin-5 mediates their nuclear export". In: *Trends in Cell Biology* 14.4 (2004), pp. 156–159. ISSN: 0962-8924. DOI: https://doi.org/10.1016/j.tcb.2004.02.006. URL: https://www.sciencedirect.com/science/article/pii/S0962892404000534.

[135] David P Bartel. "MicroRNAs: Genomics, Biogenesis, Mechanism, and Function". In: *Cell* 116.2 (2004), pp. 281–297. ISSN: 0092-8674. DOI: https://doi.org/10.1016/S0092-8674(04)00045-5. URL: https://www.sciencedirect.com/science/article/pii/S0092867404000455.

[136] Sven Diederichs and Daniel A. Haber. "Dual Role for Argonautes in MicroRNA Processing and Posttranscriptional Regulation of MicroRNA Expression". In: *Cell* 131.6 (2007), pp. 1097–1108. ISSN: 0092-8674. DOI: https://doi.org/10.1016/j.cell.2007.10.032. URL: https://www.sciencedirect.com/science/article/pii/S0092867407013517.

[137] Arianna Bottoni et al. "miR-15a and miR-16-1 down-regulation in pituitary adenomas". In: *Journal of Cellular Physiology* 204.1 (2005), pp. 280–285. DOI: 10.1002/jcp.20282. URL: https://onlinelibrary.wiley.com/doi/abs/10.1002/jcp.20282.

[138] Nozomu Yanaihara et al. "Unique microRNA molecular profiles in lung cancer diagnosis and prognosis". In: *Cancer Cell* 9.3 (2006), pp. 189–198. ISSN: 1535-6108. DOI: https://doi.org/10.1016/j.ccr.2006.01.025. URL: http://www.sciencedirect.com/science/article/pii/S153561080600033X.

[139] George Adrian Calin and Carlo Maria Croce. "MicroRNA-Cancer Connection: The Beginning of a New Tale". In: *Cancer Research* 66.15 (2006), pp. 7390–7394. ISSN: 0008-5472. DOI: 10.1158/0008-5472.CAN-06-0800. URL: https://cancerres.aacrjournals.org/content/66/15/7390.

[140] Efrat Roth et al. "Measuring the Conformation and Persistence Length of Single-Stranded DNA Using a DNA Origami Structure". In: *Nano Letters* 18.11 (2018). PMID: 30352164, pp. 6703–6709. DOI: 10.1021/acs.nanolett.8b02093. URL: https://doi.org/10.1021/acs.nanolett.8b02093.

[141] Gustavo Barcelos Barra et al. "EDTA-mediated inhibition of DNases protects circulating cell-free DNA from ex vivo degradation in blood samples". In: *Clinical Biochemistry* 48.15 (2015). Circulating Nucleic Acids, pp. 976–981. ISSN: 0009-9120. DOI: https://doi.org/10.1016/j.clinbiochem.2015.02.014. URL: http://www.sciencedirect.com/science/article/pii/S0009912015000685.

[142] MC du Rieu et al. "MicroRNA-21 is induced early in pancreatic ductal adenocarcinoma precursor lesions". In: *Clinical Chemistry* 56(4) (2010), pp. 603–12. DOI: doi:10.1373/clinchem.2009.137364..

[143] Mark Bloomston et al. "MicroRNA Expression Patterns to Differentiate Pancreatic Adenocarcinoma From Normal Pancreas and Chronic Pancreatitis". In: *JAMA* 297.17 (May 2007), pp. 1901–1908. ISSN: 0098-7484. DOI: 10.1001/jama.297.17.1901. URL: https://doi.org/10.1001/jama.297.17.1901.

[144] Aaron J. Schetter et al. "MicroRNA Expression Profiles Associated With Prognosis and Therapeutic Outcome in Colon Adenocarcinoma". In: *JAMA* 299.4 (Jan. 2008), pp. 425–436. ISSN: 0098-7484. DOI: 10.1001/jama.299.4.425. URL: https://doi.org/10.1001/jama.299.4.425.

[145] Elisa Giovannetti et al. "MicroRNA-21 in Pancreatic Cancer: Correlation with Clinical Outcome and Pharmacologic Aspects Underlying Its Role in the Modulation of Gemcitabine Activity". In: *Cancer Research* 70.11 (2010), pp. 4528–4538. ISSN: 0008-5472. DOI: 10.1158/0008-5472.CAN-09-4467. URL: https://cancerres.aacrjournals.org/content/70/11/4528.

[146] Josip Ivica, Philip T. F. Williamson, and Maurits R. R. de Planque. "Salt Gradient Modulation of MicroRNA Translocation through a Biological Nanopore". In: *Analytical Chemistry* 89.17 (2017), pp. 8822–8829. DOI: 10.1021/acs.analchem.7b01246.

[147] Yong Wang et al. "Nanopore-based detection of circulating microRNAs in lung cancer patients". In: *Nature Nanotechnology* 6.10 (Oct. 2011), pp. 668–674. ISSN: 1748-3395. DOI: 10.1038/nnano.2011.147. URL: https://doi.org/10.1038/nnano.2011.147.

[148] Yong Wang et al. "Probing molecular pathways for DNA orientational trapping, unzipping and translocation in nanopores by using a tunable overhang sensor". In: *Nanoscale* 6 (19 2014), pp. 11372–11379. DOI: 10.1039/C4NR03195D. URL: http://dx.doi.org/10.1039/C4NR03195D.

[149] Samira Mansouri Majd, Abdollah Salimi, and Foad Ghasemi. "An ultrasensitive detection of miRNA-155 in breast cancer via direct hybridization assay using two-dimensional molybdenum disulfide field-effect transistor biosensor". In: *Biosensors and Bioelectronics* 105 (2018), pp. 6–13. ISSN: 0956-5663. DOI: https://doi.org/10.1016/j.bios.2018.01.009. URL: https://www.sciencedirect.com/science/article/pii/S0956566318300162.

[150] Doo-Won Lee et al. “Field-effect transistor with a chemically synthesized MoS2 sensing channel for label-free and highly sensitive electrical detection of DNA hybridization”. In: *Nano Research* 8.7 (July 2015), pp. 2340–2350. ISSN: 1998-0000. DOI: 10.1007/s12274-015-0744-8. URL: https://doi.org/10.1007/s12274-015-0744-8.

[151] Yun Seop Yu et al. “A compact analytical current conduction model for a depletion-mode n-type nanowire field-effect transistor with a bottom-gate structure”. In: *Semiconductor Science and Technology* 23.3 (Feb. 2008), p. 035025. DOI: 10.1088/0268-1242/23/3/035025. URL: https://doi.org/10.1088/0268-1242/23/3/035025.

[152] Matti Kaisti et al. “Real-time wash-free detection of unlabeled PNA-DNA hybridization using discrete FET sensor”. In: *Scientific Reports* 7.1 (Nov. 2017), p. 15734. ISSN: 2045-2322. DOI: 10.1038/s41598-017-16028-7. URL: https://doi.org/10.1038/s41598-017-16028-7.

[153] Thomas R. Kozel and Amanda R. Burnham-Marusich. “Point-of-Care Testing for Infectious Diseases: Past, Present, and Future”. In: *Journal of Clinical Microbiology* 55.8 (2017). Ed. by Colleen Suzanne Kraft, pp. 2313–2320. ISSN: 0095-1137. DOI: 10.1128/JCM.00476-17.